UNIVERSITÀ DEGLI STUDI DELL'INSUBRIA
Dipartimento di Scienza ed Alta Tecnologia
Dottorato di Ricerca in Fisica
XXVII Ciclo

Astrophysical sources for the observed electron and positron excess at high energy with AMS-02 experiment

Davide ROZZA

A Thesis submitted for the degree of
Doctor in Philosophy

Supervisor: Dr. Pier Giorgio RANCOITA .....

Tutor: Prof. Aldo TREVES .....

June 2015

"To my Family"

"Guardate avanti e puntate sempre in alto: le stelle non sono poi così lontane!"

Paolo Nespoli, Italian astronaut

List of Abbreviations

AU	Astronomical Unit
BB	Black Body
cLIS	classical LIS
CMB	Cosmic Microwave Background
CR	Cosmic Ray
IC	Inverse Compton
IMF	Interplanetary Magnetic Field
IR	Infra Red
ISM	Interstellar Medium
ISS	International Space Station
LIS	Local Interstellar Spectrum
MHD	Magnetohydrodynamics
NS	Neutron Star
PSR	Pulsar
PWN	Pulsar Wind Nebula
SAA	South Atlantic Anomaly
SED	Spectral Energy Distribution
SN	Supernova
SNR	Supernova Remnants
UV	Ultraviolet

Contents

List of Figures

List of Tables

Preface

This Ph.D. thesis contains the result of a research undertaken at the University of Insubria (Como) and the INFN sezione di Milano-Bicocca (Milano). This research was realized within the framework of AMS-02 collaboration of which I am a member and that required my participation at the AMS-02 control center at CERN for the full year 2013, for shifts in the control room and the analysis meetings during these years.

The main topic of the thesis, related to the pulsar wind nebulae as sources of electrons and positrons (see chapter 3 and 4), led to write an article submitted to the Journal of High Energy Astrophysics with title: **Pulsar Wind Nebulae as a source of the observed electron and positron excess at high energy: the case of Vela-X**, Della Torre, S., Gervasi, M., Rancoita, P., Rozza, D. and Treves, A.; and two papers that appear as conference proceedings:

- **On the Contribution of Pulsars to the Positron Fraction in Cosmic Rays**, Della Torre, S., Gervasi, M., Rancoita, P., Rozza, D., & Treves, A. 2013a, in Proceedings of the 33^{rd} International Cosmic Ray Conference (ICRC2013), July 2-9 2013 (Rio de Janeiro, Brazil), arXiv: 1307.5197

- **Possible Contribution to Electron and Positron Fluxes from Pulsars and their Nebulae**, Della Torre, S., Gervasi, M., Rancoita, P., Rozza, D., & Treves, A. 2013b, Proceedings of the 14^{th} ICATPP Conference (Villa Olmo, Como), 23-27 September 2013, ArXiv e-prints: 1312.3483

The material presented in chapter 2, related to the study of the geomagnetic effects on the cosmic ray trajectories, has appeared in part in the following papers:

- **First Result from the Alpha Magnetic Spectrometer on the International Space Station: Precision Measurement of the Positron Fraction in Primary Cosmic Rays of 0.5-350 GeV**, Aguilar, M., ..., Rozza, D., et al. 2013, Phys. Rev. Lett., 110, 141102

- **High Statistics Measurement of the Positron Fraction in Primary Cosmic Rays of 0.5-500 GeV with the Alpha Magnetic Spectrometer on the International Space Station**, Accardo, L., ..., Rozza, D., et al. 2014, Phys. Rev. Lett., 113, 121101
- **Electron and Positron Fluxes in Primary Cosmic Rays Measured with the Alpha Magnetic Spectrometer on the International Space Station**, Aguilar, M., ..., Rozza, D., et al. 2014a, Phys. Rev. Lett., 113, 121102
- **Precision Measurement of the** $(e^+ + e^-)$ **Flux in Primary Cosmic Rays from 0.5 GeV to 1 TeV with the Alpha Magnetic Spectrometer on the International Space Station**, Aguilar, M., ..., Rozza, D., et al. 2014b, Phys. Rev. Lett., 113, 221102
- **Precision Measurement of the Proton Flux in Primary Cosmic Rays from Rigidity 1 GV to 1.8 TV with the Alpha Magnetic Spectrometer on the International Space Station**, Aguilar, M., ..., Rozza, D., et al. 2015, Phys. Rev. Lett., 114, 171103

Furthermore, I contributed to the following papers which were worked out by the Milano-Bicocca group:

- **Geomagnetic Backtracing: A comparison of Tsyganenko 1996 and 2005 External Field models with AMS-02 data**, Boschini, M., ..., Rozza, D., et al. 2013, in Proceedings of the 33^{rd} International Cosmic Ray Conference (ICRC2013), July 2-9 2013 (Rio de Janeiro, Brazil), arXiv: 1307.5192
- **Cosmic Rays in the Earth Magnetosphere: the importance of the External Field models in trajectory reconstruction with AMS-02 data**, Bobik, P., ..., Rozza, D., et al. 2013b, Proceedings of the 14^{th} ICATPP Conference, Villa Olmo 23-27 September 2013
- **Magnetosphere Effects and AMS-02 Solar Protons**, Grandi, D. & Rozza, D. November 2013, Presentation for the AMS-02 Analysis Meeting
- **Rigidity Cutoff Update From AMS-02 Solar protons - 1**, Grandi, D. & Rozza, D. March 2014, Presentation for the AMS-02 Analysis Meeting
- **Rigidity Cutoff Update From AMS-02 Solar protons - 2**, Grandi, D. & Rozza, D. April 2014, Presentation for the AMS-02 Analysis Meeting
- **AMS Rigidity Cutoff with Tsyganenko 2005 - Update**, Grandi, D. & Rozza, D. September 2014, Presentation for the AMS-02 Analysis Meeting

- **Tsyganenko 2005 Cutoff, effect on Particle Rates - 1**, Grandi, D., Rozza, D., & Della Torre, S. October 2014, Presentation for the AMS-02 Analysis Meeting

- **Tsyganenko 2005 Cutoff, effect on Particle Rates - 2**, Grandi, D. & Rozza, D. March 2015, Presentation for the AMS-02 Analysis Meeting

- **Geomagnetic Effects with AMS-02**, Della Torre, S., Grandi, D., La Vacca, G., Rozza, D., & Tacconi, M. 2013c, Internal report for the AMS-02 Collaboration

- **Effects of solar modulation on the cosmic ray positron fraction**, Bobik, P., ..., Rozza, D., et al. 2012, Advances in Space Research, 49, 1587 , advances in theory and observation of solar system dynamics - I

- **Latitudinal Dependence of Cosmic Rays Modulation at 1 AU and Interplanetary Magnetic Field Polar Correction**, Bobik, P., ..., Rozza, D., et al. 2013, Advances in Astronomy, 2013

- **A Monte Carlo study for 2-D Heliospheric modulation effects**, Bobik, P., ..., Rozza, D., et al. 37 July, 2012, in Talk at 23^{rd} European Cosmic Ray Symposium (ECRS-2012), Moscow, Russia

- **Cosmic Ray Modulation studied with HelMod Monte Carlo tool and comparison with Ulysses Fast Scan Data during consecutive Solar Minima**, Bobik, P., ..., Rozza, D., et al. 2013a, in Proceedings of the 33^{rd} International Cosmic Ray Conference (ICRC2013), July 2-9 2013 (Rio de Janeiro, Brazil), arXiv: 1307.5199

- **GeoMag and HelMod webmodels version for magnetosphere and heliosphere transport of cosmic rays**, Bobik, P., ..., Rozza, D., et al. 2013d, in Proceedings of the 33^{rd} International Cosmic Ray Conference (ICRC2013), July 2-9 2013 (Rio de Janeiro, Brazil), arXiv: 1307.5196

- **Suprathermal particle addition to solar wind pressure: possible influence on magnetospheric transmissivity of low energy cosmic rays?**, Bobik, P., ..., Rozza, D., et al. 2013b, in Proceedings of the 33^{rd} International Cosmic Ray Conference (ICRC2013), July 2-9 2013 (Rio de Janeiro, Brazil), arXiv: 1307.5195

- **Solar Modulation along last solar minimum**, Bobik, P., ..., Rozza, D., et al. 2013a, Proceedings of the 14^{th} ICATPP Conference, Villa Olmo 23-27 September 2013

- **Transport of cosmic rays in magnetosphere and heliosphere: GeoMag and HelMod webmodels**, Bobik, P., ..., Rozza, D., et al. 2013c, Proceedings of the 14^{th} ICATPP Conference, Villa Olmo 23-27 September 2013

- **Evaluation of energetic proton pressure during solar events and possible effects on the Magnetosphere**, Bobik, P., ..., Rozza, D., et al. 2013c, Proceedings of the 14^{th} ICATPP Conference, Villa Olmo 23-27 September 2013

Introduction

Cosmic ray electrons and positrons represent only $\sim 1\%$ of the total particles which reach the Earth. The standard scenario predicts that the main component of the electron spectrum is the one produced by supernova remnants, while positrons are supposed to be mainly originated from the decay of muons produced by cosmic ray interactions with the interstellar medium. In the last years, space born experiments, like PAMELA before and AMS-02 later, have detected an anomalous electron and positron abundance with respect to the theoretical model predictions, for energy above ~ 10 GeV. In this work, we will use the AMS-02 data characterised by an high statistics and a wide energy range.

Before reaching the Earth, cosmic rays propagate in the Galaxy (as treated in chapter 3). Electrons and positrons are characterised by an high energy loss rate during their travel in the interstellar medium; we evaluated that an electron (or positron) with an initial energy of 100 GeV can travel at most for ~ 2 kpc. The cosmic ray propagation is described by models, as GALPROP. We worked out the electron and positron spectra using propagation parameters according with e.g., the ratios between fluxes of particles produced in the interstellar medium and the ones produced in known sources. We have subtracted the spectra of electrons and positrons, evaluated with GALPROP, from the AMS-02 ones. Since we have found an equal excess of electrons (above ~ 90 GeV) and positrons (above ~ 10 GeV), additional sources of electron-positron pairs, with distance less than 2 kpc from the Solar System, are required.

The present work is finalized to investigate possible astrophysical sources (i.e., pulsars and their nebulae) of positrons and electrons, which may account for the flux excess. We will see in chapter 4 that the analysis on the pulsar wind nebulae available leads to consider Vela-X as the main candidate for the interpretation of electron and positron excess above 100 GeV. At 1 TeV, the flux expected with our models is around 1.2×10^{-7} $(\mathrm{GeV\ m^2\ s\ sr})^{-1}$, in agreement within the AMS-02

uncertainties. The particle spectra are also responsible of the wide photon spectra from radio to gamma energy observed at the source. Furthermore, a relatively close source, as Vela-X ($\sim$ 300 pc faraway), could give an anisotropic signal in the arrival cosmic ray directions. To study a dipole signal in the AMS-02 data, located inside the magnetosphere, we have performed the reconstruction of the particle trajectory up to the magnetopause using the so called back-tracing technique. The back-tracing can distinguish among cosmic rays produced outside the magnetosphere from the ones generated or trapped inside. A spherical harmonics analysis is presented focusing the attention on the dipole component divided into its three terms in galactic coordinates. Our predictions are inside 2σ from the AMS-02 data, higher statistics and wider energy range are needed.

At the end, an outlook and the prospects for future analysis are presented. The AMS-02 data are fundamental; in fact, this spectrometer is able to detect electrons, protons, ions and antimatter in a wide energy range, from few hundreds MeV up to few TeV. The future higher statistics will allow us to better understand the cosmic ray propagation and discriminate the source responsible for the measured excess.

Chapter 1

Cosmic Rays

Cosmic Rays (CRs) are charged particles moving in space, which may reach the Earth. They span over a very wide energy range from several MeV up to $\sim 10^{20}$ eV and they are mainly composed by protons, whose energy spectra distribution is well described by power laws. The first measurements of these particles were carried out at the beginning of the 20^{th} century (see section 1.1); in a century, many particles, previously unknown, were discovered in CRs (e.g., positrons). Electrons and positrons represent only $\sim$ 1% of the total particles which reach the Earth (see section 1.2). In section 1.3 we present the propagation of these particles in the different environments (galaxy, heliosphere and magnetosphere), where interactions with magnetic and radiation fields occur. The aim of this work regards the study of electron and positron CR fluxes and their interpretation in the energy range between $\sim$ 10 GeV and $\sim$ 1 TeV. For this reason, we use the recent experimental data from space born cosmic ray detector AMS-02 (described in section 1.4).

1.1 History, spectrum and composition

The history of CRs starts at the beginning of the 20^{th} century when a French physicist, H. Becquerel, discovered that certain elements are unstable and transmute into other elements. In these processes the elements emit what appears to be particles (called "radiation") and the process itself is referred to as "radioactive decay". An electroscope would spontaneously discharge in presence of radioactive materials and the rate of discharge of the instrument is used as a measure of the level of radiation. However, physicists noticed that electroscopes were found to discharge slowly even in the absence of radioactive matter. This residual discharge could not be attributed to leakage and it appears to be a background radiation.

It is common knowledge that CRs were discovered for the first time by Hess

(1912) and he was awarded of the 1936 Nobel Prize in physics. He made measurements of radiation levels at different altitudes with electroscopes aboard a balloon. Thanks to an accurate study made by De Angelis (2012), some discoveries and experiments made before 1912 have been rehabilitated. One of the physicists who made similar Hess's analysis was Pacini (1912): he measured penetrating radiation underwater. A decrement observed in the counting rate, starting on the sea (and lake) surface down to underwater, was attributed, by Pacini, to an extraterrestrial radiation, or better, to a non negligible part of this penetrating radiation independent of the emission from the Earth's crust. A similar analysis was made by Hess on balloon to distance the electroscopes from radiation sources on the Earth's surface. Hess went as high as about 5300 meters in his balloon and he found that the radiation levels increased with altitude. He interpreted this result as a radiation entering the atmosphere from the outer space. He gave this phenomenon the name Cosmic Radiation, which later evolved into Cosmic Rays. In the following years, many discoveries were made concerning CRs; by developing the cloud chamber in 1912, Wilson made it possible to detect and follow the tracks left by ionizing particles. Up to the thirties, only electrons, protons and photons were known as elementary particles; the positron was discovered in a cloud chamber by Anderson (1932) and Blackett & Occhialini (1932). This was the antiparticle of the electron, which had been theoretically predicted by Dirac in 1928. For years to come, before the accelerator era, cosmic rays remained the only source of high-energy particles. Today, thanks to many experiments on the ground, on balloons and in space, we learned many aspects concerning these particles coming from the space.

CRs are mainly composed by protons (numerical abundance $\sim 86\,\%$) and alpha particles ($\sim 12\,\%$); the remaining part: other nuclei, electrons and antiparticles (e.g., positrons and antiprotons) are only few percent of the total. Figure 1.1, left panel, reports the measured chemical abundances of cosmic rays with respect to the ones in the Solar System. It is possible to note that some light (Li, Be and B) and heavier nuclei (including F, Sc, Ti and V) have much higher abundances in the CR and they are essentially absent in stellar nucleosynthesis. On the other hand, the fact that the less common elements, which are not produced in suns, are much more abundant in the arriving CRs than in the Solar System, can be understood quantitatively as the result of nuclear interactions of abundant cosmic ray elements with interstellar gas. As an example, interactions of C, N, O result in fragments of lighter elements, Li, Be and B. They arrive at the Earth after the propagation in the space where they interact with the magnetic fields and the other particles. In figure 1.1, right panel, we report the CR spectrum as a function of the energy. The CRs spectra are

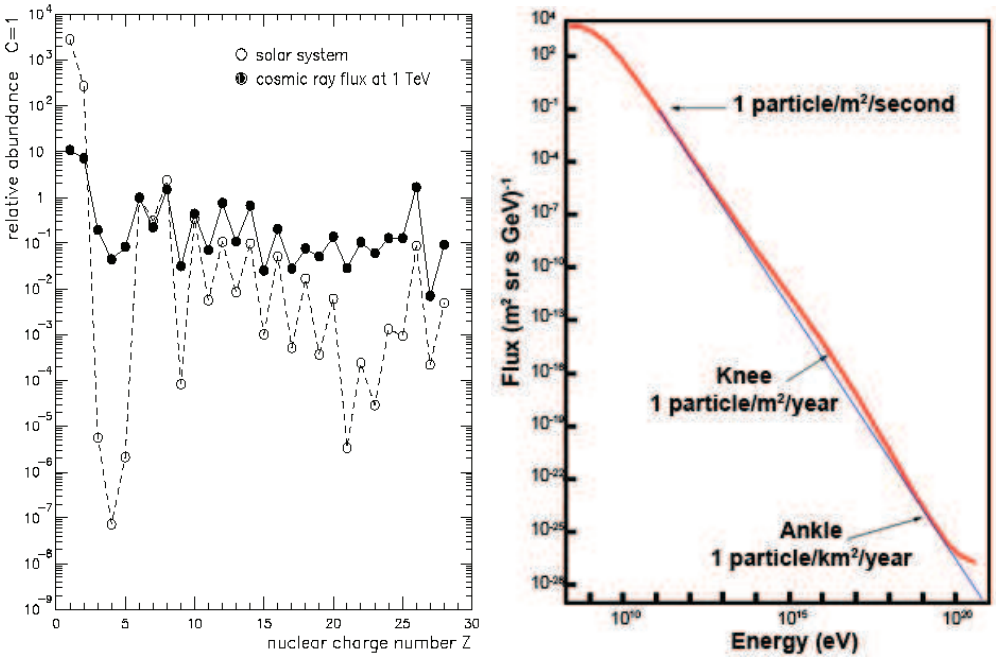

Figure 1.1: Composition of cosmic rays, taken from the ACE/CRIS instrument, in comparison to Solar System abundances (normalised to C) (left), source `http://www.nupecc.org/report97/report97_astrobib/node9.html` (2014); cosmic ray spectrum (right), source `http://astronomy.swin.edu.au/cosmos/C/Cosmic+Ray+Energies` (2014).

commonly described by a power law of the energy:

$$\frac{dN(E)}{dE} \propto E^{-\gamma}, \tag{1.1}$$

where γ is the spectral index, which is about 2.7 below the so called *knee* at $\sim 10^{15}$ eV. Here the spectrum smoothly increases the slope ($\gamma \sim 3$) up to $\sim 10^{18}$ eV, corresponding to the *ankle*. After that, γ returns to be ~ 2.5. The different slopes reflect the different origins of particles; in particular, below the *knee*, their curvature radius is smaller than the galactic disc thickness, hence their sources must belong to our Galaxy. Below ~ 20 GeV the CRs spectra deviate from the power law, reported in equation (1.1) with $\gamma \sim 2.7$, due to the Sun influence (see section 1.3.1).

The origin of the CRs is still under debate. In fact, the particle propagation in the interstellar medium (ISM) depends on the magnetic and radiation fields. In this case, if the energy is not high enough, we lose every information about the sources. The main hypothesis leads to consider the production and acceleration of the particles near stars, specially at the end of their life, e.g., during a supernova (SN) explosion or after in their remnants (SNR). Particles generated and accelerated

at known sources are considered as primaries; CRs are also produced directly inside the ISM: these are commonly referred to as secondaries.

1.2 Electrons and Positrons in Cosmic Rays

At 10 GeV, the electron flux is $\sim 1\%$ of the proton one, while the positrons are $\sim 8\%$ of the electrons (see e.g., section 3.1). The propagation of this kind of particles is characterized by a high energy loss rate due to interactions with the magnetic and radiation fields. As for other species of cosmic rays, we divide electrons and positrons in primary particles (generated and accelerated at known sources) and secondary particles (produced by interactions in the ISM). It is common knowledge that primary CR electrons are produced and accelerated in the same place of nuclei (e.g., SNR). We will discuss other primary sources of electrons and positrons in chapter 4.

Secondary electrons and positrons are produced in interactions between primary CRs (e.g., cosmic ray protons p) and nuclei (X) of the interstellar medium (Moskalenko & Strong 1998; Delahaye et al. 2009; Delahaye, T. et al. 2010). Analysing the main process that involves protons, the main channels for pp interactions at low energy ($E < 3$ GeV) are for single pion production (see e.g., Norbury & Townsend 2007):

$$pp \rightarrow pp\pi^0 \quad [\times 2] \tag{1.2}$$
$$\rightarrow pn\pi^+ \quad [\times 2] \tag{1.3}$$

and for double pion production:

$$pp \rightarrow pp\pi^0\pi^0 \tag{1.4}$$
$$\rightarrow pp\pi^+\pi^- \quad [\times 2] \tag{1.5}$$
$$\rightarrow pn\pi^0\pi^+ \quad [\times 2] \tag{1.6}$$
$$\rightarrow nn\pi^+\pi^+. \tag{1.7}$$

The number in square brackets after some reactions indicates that the reaction can proceed in a number of different ways and therefore the number of particles produced needs to be multiplied by the number in square brackets (e.g., $pp \rightarrow pn\pi^+$ can also proceed as $pp \rightarrow np\pi^+$, with the pion being produced from the other nucleon). At

low energy, i.e., around the two pion threshold, the ratio of the number of pions is:

$$\pi^+ : \pi^- : \pi^0 = 8 : 2 : 6 = 4 : 1 : 3 \tag{1.8}$$

At higher energies direct production of charged pions proceeds without the formation of the Δ resonance (Delahaye et al. 2009). Kaons $K^{\pm}$ may also be produced; the decay of kaons produces muons (63.55%) and pions (20.66%) (see Beringer et al. 2012), while pions and muons decay in the following ways:

$$\pi^+ \to \mu^+ + \nu_\mu \qquad \pi^- \to \mu^- + \bar{\nu_\mu} \tag{1.9}$$

$$\mu^+ \to e^+ + \nu_e + \bar{\nu_\mu} \qquad \mu^- \to e^- + \nu_\mu + \bar{\nu_e}. \tag{1.10}$$

Cosmic rays can interact with the matter in different ways; one of these regards the spallation process that happens when a cosmic ray particle (e.g., a proton) impacts with matter. The result of the collision is the expulsion of large numbers of nucleons (protons and neutrons) from the object hit. As pointed out by Delahaye, T. et al. (2010), since spallation involves positively charged particles, charge conservation implies that it generates more positrons than electrons. This statement is not entirely accurate for neutron decay, but electrons arising from neutron decay have a very low energy (mostly $E < 10$ MeV) and they are outside of the energy range considered in this work (see Zhang L. 2001; Kamae et al. 2006).

1.3 Cosmic ray propagation in Galaxy

Our Galaxy, the Milky Way, is a disk of radii ~ 15 kpc[1] and the Sun is located at ~ 8.5 kpc from the Galactic centre. The Galaxy contains matter in two different states: condensate objects (stars) and diffuse matter (ISM). This region emits synchrotron radiation due to a magnetic field of few μG that forces CRs in circular orbits. Charged particles propagate through the galactic magnetic field and are deflected by its irregularities. The main stream of the magnetic field lines is supposed to follow the spiral arms (Schlickeiser 2002, Chap. 2). The Larmor radius of relativistic particles in a perpendicular magnetic field is:

$$r_L = \gamma \frac{mv}{qB} = \frac{mc}{qB} \sqrt{\left(\frac{E}{mc^2}\right)^2 - 1} \tag{1.11}$$

[1]Parsec, 1 pc= 3.086×10^{16} m

where m, v e q are mass, speed and charge of the particle, B is the strength of the perpendicular magnetic field and γ is the particle Lorentz factor. Using an average magnetic field of $B \sim 3\ \mu\text{G} = 3 \times 10^{-10}$ T, even 10^6 GeV protons have gyroradii smaller than 1 pc. Propagation of cosmic rays is normally approximated as a diffusive process (Strong et al. 2007). Because of their small gyroradii, the arrival directions of low-energy particles are essentially isotropic.

The ISM is a cold plasma in which the magnetic field lines are bound. CRs lose their energy and interact with the ISM changing their spectrum and composition. The lifetime of a cosmic ray depends on its energy loss rate, down to the mean energy of the particles in the interstellar medium, while the upper limit is due to the time that a particle needs to escape from the Galaxy ($\sim 10^7$ years). The interstellar gas density is not constant and many regions, of $1 - 10$ pc big, are denser than ISM and with an higher magnetic field. Interactions between CRs and these clouds may be responsible for the acceleration mechanisms of the cosmic particles. Fermi (1949) proposed two kinds of acceleration: first-order Fermi acceleration (in shocks) and second-order Fermi acceleration (in the environment of moving magnetized gas clouds). In the first case, the gain in energy is $\Delta E/E \propto \beta = v/c$, while in the second one, $\Delta E/E \propto \beta^2$.

CR propagation may be described by a transport equation in which the time evolution of their density $\psi(\vec{r}, p, t)$, per unit of total momentum p at position $\vec{r}$, is described by (see e.g., Strong et al. 2007):

$$\begin{aligned}\frac{\partial \psi(\vec{r},p,t)}{\partial t} &= q(\vec{r},p,t) + \vec{\nabla}(D_{xx}\vec{\nabla}\psi - \vec{V}\psi) + \frac{\partial}{\partial p}p^2 D_{pp}\frac{\partial}{\partial p}\frac{1}{p^2}\psi \\ &\quad -\frac{\partial}{\partial p}\left[\dot{p}\psi - \frac{p}{3}(\vec{\nabla}\vec{V})\psi\right] - \frac{1}{\tau_f}\psi - \frac{1}{\tau_r}\psi. \end{aligned} \tag{1.12}$$

The equation (1.12) includes: the spatial and time distribution of the sources $q(\vec{r}, p)$, the spatial diffusion process keep into account the diffusion coefficient:

$$D_{xx} = \beta D_0 (\rho/\rho_0)^{\delta}, \tag{1.13}$$

the momentum gain or loss rate during the propagation $\dot{p}$, the fragmentation and radioactive decay time respectively τ_f and τ_r. The boundary conditions depend on the model; usually $\psi = 0$ at the border of the Galaxy, where particles escape into intergalactic space, but this is obviously just an approximation (since the intergalactic flux is not zero) which can be relaxed for models with a physical treatment of the boundary. CR propagation is commonly treated in diffusion models in which the interactions with the magnetic field are purely diffusive and the diffusion coeffi-

cient is scalar. Many galaxys have a galactic wind with a velocity ($\vec{V}$) that increases from the center to the border of the disk; this phenomenon is called "convection". Diffusive reacceleration is described as diffusion in momentum space (identified by D_{pp}); Alfén studied the reacceleration of CRs in interactions with the MHD waves (described in the magnetohydrodynamics theory) and he introduced the velocity ($\vec{V_a}$, Alfén velocity) that described the propagation of small perturbations in the magnetic field.

The equation (1.12) is the most general description of the CR propagation. All its terms have been fixed from observations of the particle fluxes. The analysis of the nuclei spectra gives us information on the diffusion, convection, reacceleration parameters. In the same way, it is possible to evaluate also the size of the Galaxy and the escape time of the CRs.

1.3.1 Propagation in Heliosphere

The Earth is located inside the solar cavity, i.e., that particular region influenced by the Sun. At energies less than $\sim$ 10 GeV, the Local Interstellar Spectrum (LIS, the CR spectrum in the ISM) is modified by the "solar modulation". This effect is related to the propagation of CRs inside the heliosphere, the region influenced by the activity of the Sun. Inside this region, the interactions between particles and the small scale irregularities of the magnetic field are described by a diffusion process. The region affected by the solar activity extends for about 100 AU[2]. Parker predicted the existence of the *heliospheric termination shock*, which is the region where the solar wind, that is flowing supersonically away from the Sun, must make a transition to subsonic; he also predicted the *heliopause*, which is the boundary surface separating the interstellar and solar wind plasmas and it is located outside the termination shock. A rough estimate of the heliopause location may be obtained from balancing the solar wind pressure (P_W) and the interstellar medium pressure (P_{ISM}). Since the thermal and magnetic pressure components of the solar wind can be neglected, P_W is practically given by the solar wind dynamic pressure.

The magnetic field is carried out through the Solar System by the solar wind into a large rotating spiral (known as Parker spiral). This shape is due to the rotation of the Sun. The interplanetary conditions vary as a function of the solar cycle that is approximately 22 years; consequently also the spectrum of cosmic rays for energies below few tens of GeV undergoes variations. For energy above $\sim$ 20 GeV, it is commonly acknowledged that, inside the heliosphere, particle propagation is

[2]The astronomical unit is the average Earth-Sun distance, 1 AU $\sim 1.49598 \times 10^{11}$ m

no longer affected by this phenomenon; thus, the omnidirectional distribution is the one determined by the LIS. The Tilt angle is one of the parameters that change with the solar activity; it is the angle between the neutral sheet, the plane that divides the heliosphere into two hemispheres with opposite magnetic polarity, and the equatorial plane. In figure 1.2 is reported the time variation of the Tilt angle for the last decades[3].

The diffusion process can be described by the Parker equation (Parker 1957,

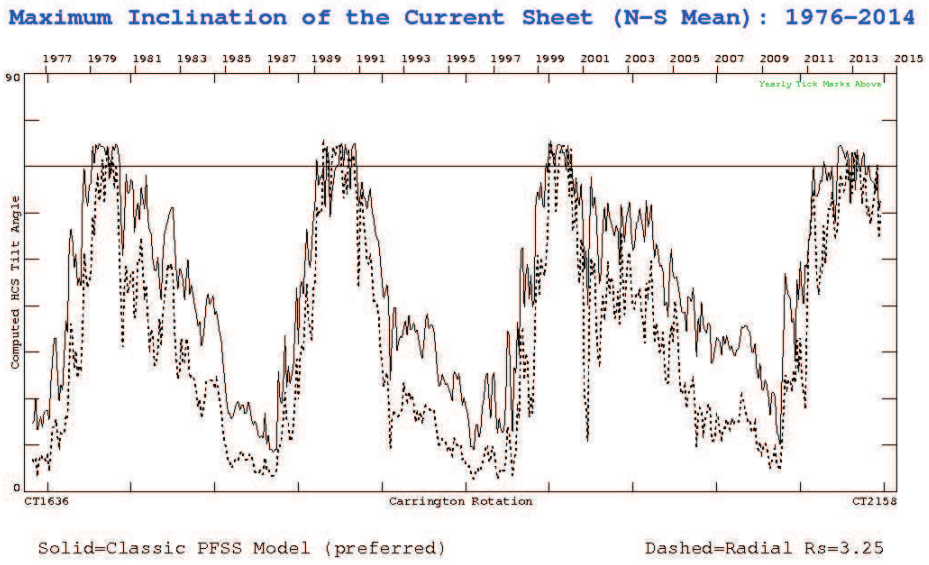

Figure 1.2: Time variation of the Tilt angle[3].

1965), where the time evolution of the particle density U is:

$$\frac{\partial U}{\partial t} = \nabla(\mathbf{K^S}\nabla U - \mathbf{V_{sw}}U - \mathbf{v_d}U) + \frac{1}{3}(\nabla \mathbf{V_{sw}})\frac{\partial}{\partial T}(\alpha_{\mathrm{rel}} T U). \tag{1.14}$$

The first term in equation (1.14) represents the diffusion due to the small scale magnetic field irregularities; the second one describes the convection due to the solar wind moving out from the Sun ($\mathbf{V_{sw}}$ is the solar wind velocity). The term with $\mathbf{v_d}$ (drift velocity) takes into account the drift of the particles due to the large scale structure of the magnetic field, while the last term contains the adiabatic energy loss of the particles (see P. Bobik 2012 for an exhaustive description).

[3] `http://wso.stanford.edu/gifs/Tilts.gif` (2014)

1.3.2 Influence of the Magnetosphere

Cosmic rays approaching the Earth interact with the Earth magnetic field that changes their directions. The geomagnetic field is produced by currents flowing inside the Earth (probably due to the Earth nucleus) and currents due to charge motion outside the planet. This field can be represented, as first approximation, by a dipole with an axis tilted of $\sim 11°$ respect to the Earth rotational axis and shifted with respect to it; its orientation is also opposite to the rotational axis. The region affected by this field is called magnetosphere, which extends from about 6 to 12 Earth radii ($R_E \sim 6378$ km) in the Sun direction. This limit varies with respect to the magnetic field carried out from the Sun by the solar wind. On the opposite side of the Sun, the magnetosphere extends like the tail of a comet up to about a thousand Earth radii. Inside this region, there are the so-called "radiation belts", or Van Allen belts, that consist of charged particles spiralling around the field lines of the geomagnetic field. Figure 1.3 shows an illustration of these belts.

Cosmic rays move following the trajectorys of charged particles inside a magnetic

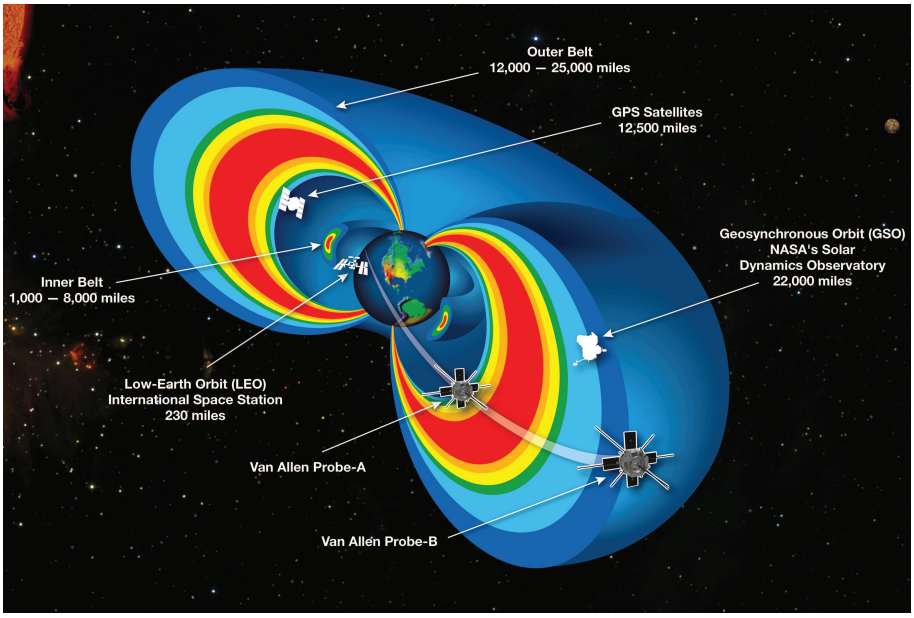

Figure 1.3: A cutaway model of the radiation belts. The radiation belts are two donut-shaped regions encircling Earth, where high-energy particles, mostly electrons and ions, are trapped by Earth's magnetic field. This graphic also shows satellites near the region of trapped radiation. Credit: NASA.

field. For low energy particles the motion is divided into three components: a spiral motion around the field lines, a North-South motion along these lines and a drift

motion East-West. The particle rigidity is defined by:

$$R = \frac{pc}{Ze} \tag{1.15}$$

where p and Ze are the momentum and the charge of the particle respectively, and c is the speed of light. The minimum rigidity value of the particle to enter or escape from the magnetic field is called "geomagnetic rigidity cut-off" R_{cut}. We will discuss more in details this parameter in chapter 2.

1.4 Space born cosmic ray detectors

Cosmic ray detectors are divided into these categories: ground, atmospheric and space detectors. The first kind is characterized by large sizes used to collect all the particles of a shower generated by CRs that interact with the atoms of the atmosphere. Moreover, the high extension of the apparatus leads to higher energy respect to the other detectors. Atmospheric and space experiments, for the moment, can not reach energy above few TeV, but they study with more accuracy the galactic cosmic rays and their different species.

Two space experiments, in particular, are still in orbit: PAMELA[4] and AMS-02[5]. With them it is possible to search structures in cosmic ray spectra from e.g., dark matter or new astrophysical sources, to study cosmic ray propagation mechanisms, the solar activity effects and the particles in the Earth's magnetosphere.

1.4.1 PAMELA

The PAMELA experiment (a Payload for Antimatter Matter Exploration and Light-nuclei Astrophysics) is installed on the up-ward side of the Russian Resurs-DK1 satellite and has been launched the 15^{th} of June 2006 from Kazakhstan. The satellite is travelling around the Earth along an elliptical orbit with an upward orientation, at an altitude ranging between $350 - 610$ km with an inclination of $\sim 70°$. In September 2010 the orbit was changed to a nearby circular one, at an altitude of ~ 570 km, and it has not changed since then. These characteristics allow PAMELA to detect particles between ~ 100 MeV up to the TeV region.

The apparatus (450 kg weight), reported in figure 1.4, is constituted by a magnetic spectrometer with a microstrip silicon tracker and a permanent magnet of intensity 0.43 T for the evaluation of the rigidity and the sign of the particles. The

[4] `http://pamela.roma2.infn.it/index.php` (2014)
[5] `http://www.ams02.org/` (2014)

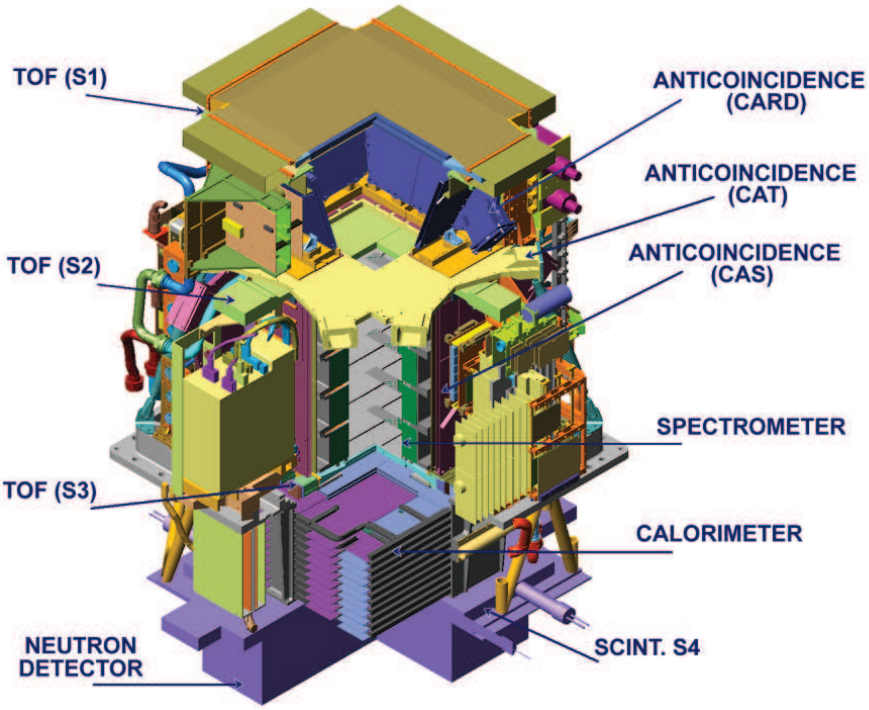

Figure 1.4: PAMELA apparatus and its sub-detectors[4].

time-of-flight (ToF) system distinguishes particles that come from the top and from the bottom of the experiment estimating the particle velocity. The energy released by the interacting particle is measured in a sampling imaging calorimeter and the interaction topology of the particle inside the calorimeter is reconstructed. The imaging calorimeter is the primary detector to distinguish electrons and positrons from antiprotons and protons with the same charge sign and momentum. In the bottom part, a neutron detector helps the calorimeters to distinguish hadronic from electromagnetic showers. The geometric acceptance is 0.00215 m^2sr. A summary of the particle fluxes detected and published by PAMELA collaboration are reported in figure 1.5.

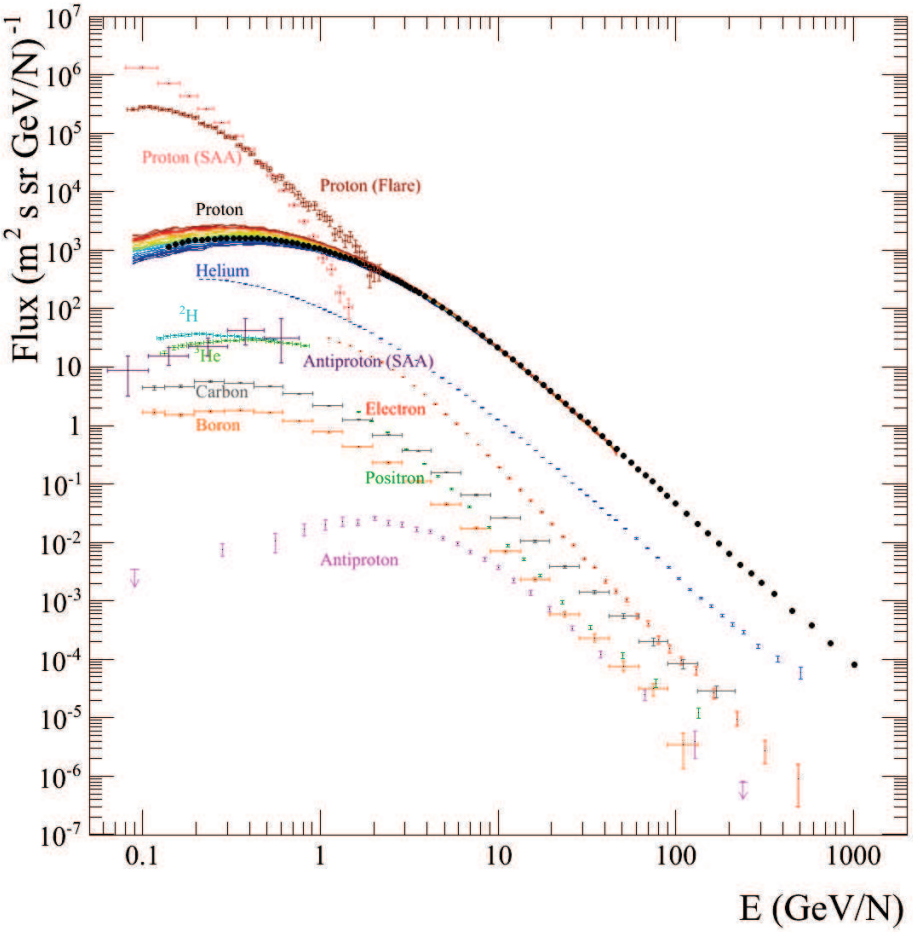

Figure 1.5: Fluxes of different particle species measured by PAMELA, see `http://pamela.roma2.infn.it/index.php` (2014).

1.4.2 AMS-02

AMS-02 (Alpha Magnetic Spectrometer) was installed on the International Space Station (ISS) on 19^{th} of May 2011, during the NASA mission STS-134 with the Space Shuttle Endeavour. One of the main topic of this experiment is to measure the cosmic ray spectrum for the nuclei up to iron ($Z = 26$), electrons and antimatter in a wide energy range from ~ 0.1 GeV up to ~ 2 TeV. In 1998, a prototype of AMS, AMS-01, flew on board of the Space Shuttle Discovery (NASA mission STS-91) for few days.

The main aim of the experiment is to detect antimatter particles in cosmic

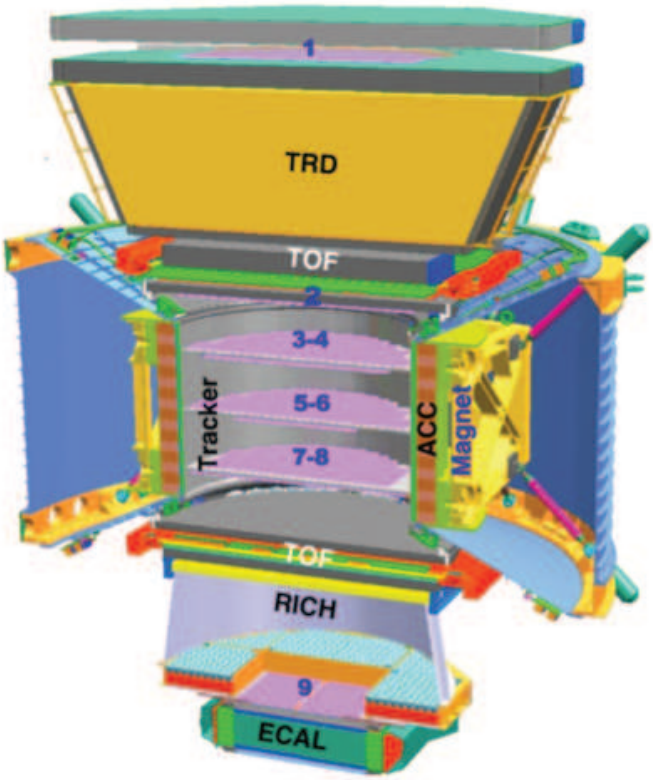

Figure 1.6: AMS-02 apparatus and its sub-detectors[5].

rays. The measure of these spectra could give us information related to possible astrophysical (e.g., pulsars) or exotic (e.g., dark matter) sources of antimatter. AMS-02 is characterized by a huge acceptance (0.45 m^2sr) and it will collect data for, at least, 10 years. Its apparatus is composed by different sub-detectors, reported in figure 1.6. To be able to operate in space, the entire apparatus of the AMS-02 needs to respect the constraints imposed by space missions. First of all, the transport aboard the Space Shuttle Endeavour (NASA mission STS-134), figure 1.7, and the position on the ISS have placed a limit of 8.5 tons to the experiment, a maximum power consumption limit of 2 kW and a transmission rate of 2 Mbits/s. In addition,

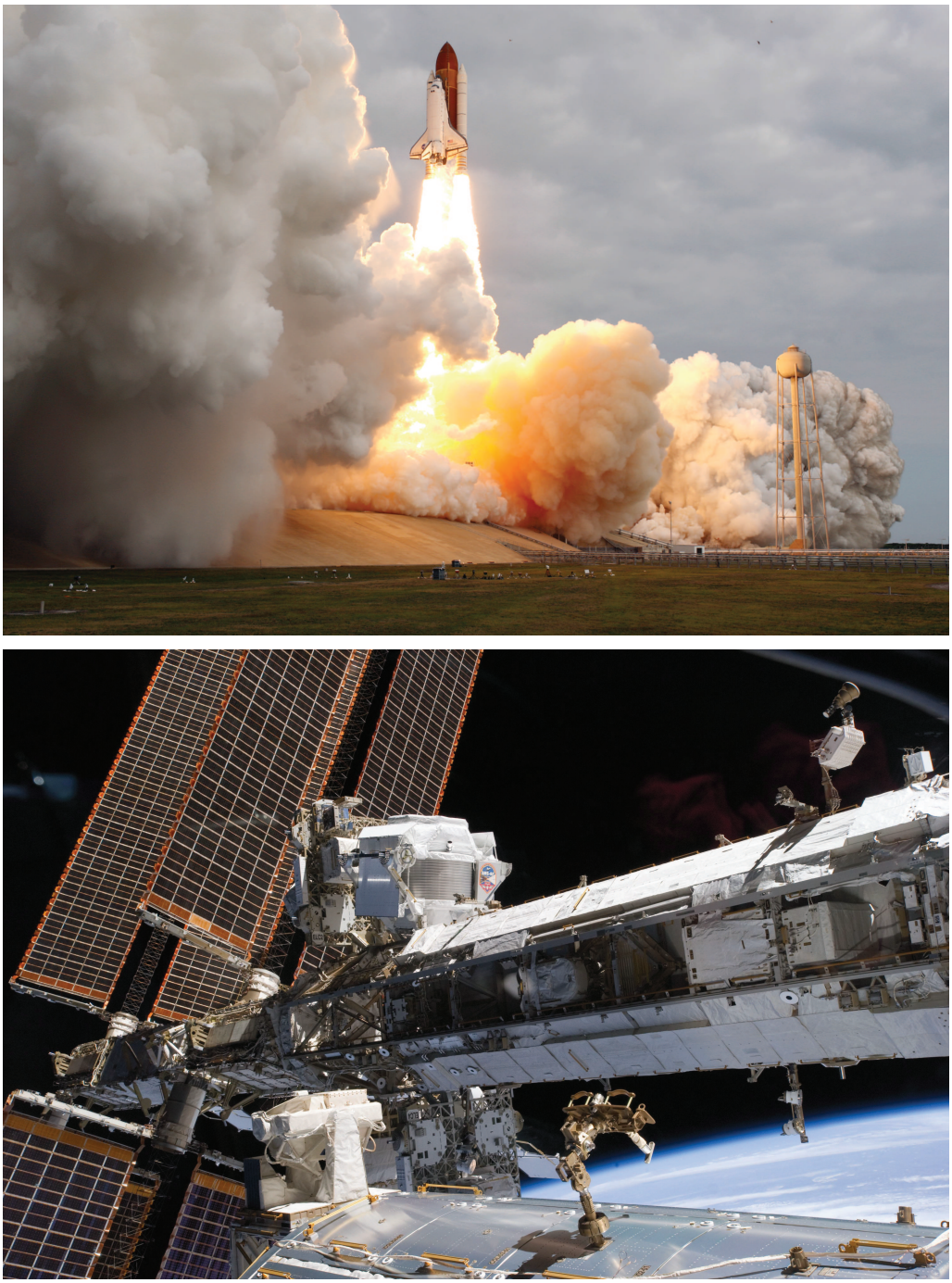

Figure 1.7: AMS-02 launch on bord of the Space Shuttle Endeavour (top picture) and on the ISS (bottom picture). Credit: NASA.

the experiment must be able to work in absence of external operations during its entire life, withstand acceleration (9g) and vibration (150 dB) during the space shuttle launch that was in May 16^{th} 2011.

On May 19^{th} AMS-02 was placed on one of the ISS arms with a temperature variation between $-80°$ C and $+50°$ C in vacuum with revolution cycle around the Earth of about 90 minutes. Each sub-detectors was subjected to specific tests and, once assembled, other tests in flight configuration were made inside the anechoic chamber at the ESTEC ESA center (European Space Agency) in Netherlands, see figure 1.8 left. This environment, exploited in order to reduce as more as possible the reflection on the walls, is able to simulate, in a closed room, the conditions of the open spaces of infinite dimension, as a result of the absence of reflections. In order to observe the response of the detector, AMS-02 was tested using several Beam Test, at CERN, with beams of protons, electrons, positrons and photons of different energy and different inclination of the experiment with respect to the beam, figure 1.8 right. The reference system of AMS-02 has the z-axis pointing from the calorimeter to the TRD, the y-axis in the direction of curvature of the particles in the magnet and the x-axis parallel to the field lines inside the magnet.

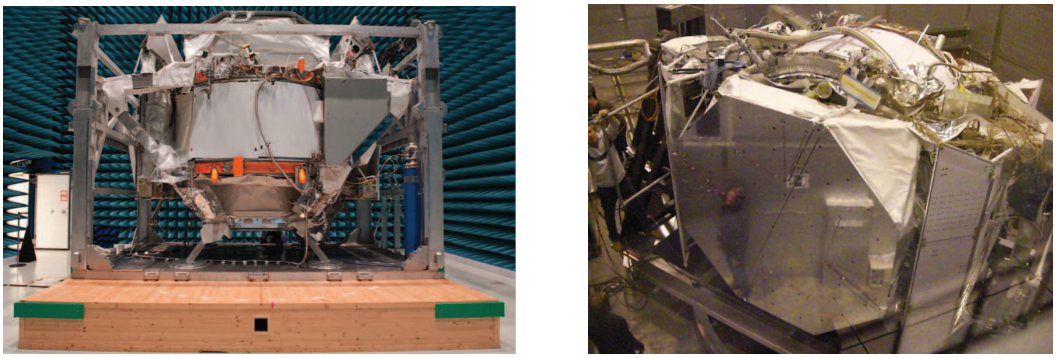

Figure 1.8: AMS-02 at ESTEC on the left and at CERN, for the beam test, on the right. Source: `http://www.ams02.org/` (2014).

AMS-02 sub-detectors

The first sub-detector on the top is the **TRD** (Transition Radiation Detector) used to identify particles through the detection of the transition radiation (TR). This radiation consists of soft X-rays which are emitted when charged particles traverse the boundary between two media with different dielectric constants. In the momentum range from 10 to 300 GeV/c, light particles such as electrons and positrons have much higher probability of emitting TR photons than heavy particles such as

protons and antiprotons. The detector consists of 20 layers of 6 mm diameter straw tubes alternating with 20 mm layers of polyethylene/polypropylene fleece radiator. The tubes are filled with a 80% - 20% mixture of Xe-CO_2 at 1.0 bar absolute from a recirculating gas system.

The **ToF** detector registers the particle transit time into AMS with a sensibility of $\sim$ 120 ps; it distinguishes particles that come from the top and from the bottom and it is the trigger of the experiment. Inside the ToF plates, there is the permanent magnet (0.15 T) that bends the particle trajectories.

Three pairs of silicon **Tracker** layers (inner Tracker) are inside the magnet and detect the positions of the transit particles. Two Tracker layers (outer Tracker) are on the top (above the TRD) and on the bottom (between RICH and ECAL) to increase the maximum detectable rigidity. Another layer is located just before the magnet to identify the entrance position. The silicon Tracker consists of 2300 double-sided silicon micro-strip sensors arranged in eight circular layers perpendicular to the magnet axis. The Tracker provides a position resolution of 8.5 μm (30 μm) in the bending (non-bending) plane. The total instrumental surface area is 6.45 m^2 with 196 k readout channels. A laser alignment system is being used to ensure the long term stability of the resolution with position accuracy of better than 4 μm.

Around the inner Tracker, the **ACC** (Anti-Coincidence Counter) rejects particles which do not enter from the magnet aperture. The ACC features a modular design, the cylinder has a diameter of 1.1 m and a height of 0.83 m and is made out of 16 scintillation panels (Bicron BC-414) with a thickness of 8 mm. The ultraviolet scintillation light through ionization losses of charged particles is absorbed by WLS (Wavelength Shifting Fibers) which are embedded into the panels. The WLS fibers are coupled to clear fiber cables for the final light transport to the photomultiplier tubes (Hamamatsu R5946). A set of two panels is being read out by the same two photomultipliers, one on top and one on the bottom, via clear fiber cables (Y-shape) in order to have redundancy and to save mass.

The Ring Imaging CHerenkov detector, or **RICH**, estimates the velocity of charged particles by measuring the vertex angle of the cone of Cherenkov light. The Cherenkov light is emitted as the particle passes through a tile of silica aerogel or sodium fluoride. The light guide material in the Unit Cell assembly is Polymethyl Methacrylate (PMMA), (PlexiglasTM). RICH measures the Cherenkov light using photomultiplier tubes. RICH is a proximity focusing device with a dual radiator configuration on top made of 92 aerogel tiles of 25 mm thickness; the refractive index is 1.050. In addition, there are sodium fluoride (NaF) tiles with a thickness of 5 mm covering an area of 34 cm x 34 cm. The NaF placement prevents the loss of

photons in the hole existing in the center of the readout plane (64 cm x 64 cm), in front of the ECAL device located below.

The last main detector is the Electromagnetic CALorimeter (**ECAL**). Incident particles interact producing showers of low-energy particles. The shape of the shower identifies the particle kind (e.g., proton or positron) and the particle total energy. ECAL is an imaging calorimeter consisting of 9 modules made of layers of lead and scintillating fibers. Its function is to completely stop particles. Each module has a 648 mm x 648 mm section and is 18 mm in depth, which corresponds to 1.8 radiation lengths. In two successive modules the fibers are rotated of 90° and follow in the x or y direction. The fibers of a module are read only at one end of the PMT (Photomultiplier Tube) of Hamamatsu (R7600-00-M4) and placed alternatively on each side. One PMT consists of 4 independent pixels. In this way, the elementary cell of the calorimeter has the size of 648 mm x 9 mm in the x-y directions and 9 mm in the z direction.

Particle mass is an indirect measurement in AMS. It is calculated starting from rigidity measured by Tracker, charge measured by Tracker, ToF and RICH, and velocity measured by RICH and ToF.

AMS-02 POCC and DATA position

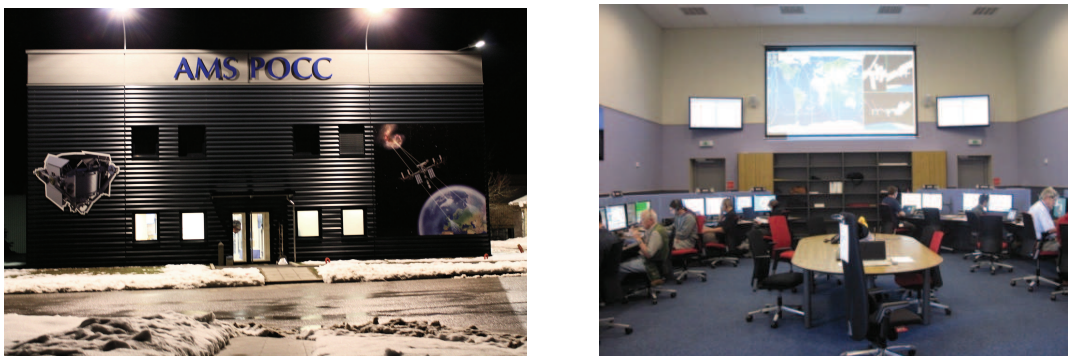

Figure 1.9: AMS-02 control room at CERN. Courtesy of S. Della Torre (left) and personal photograph by author (right).

The main control room of AMS-02 is located at the AMS Payload Operations Control Centre (POCC) at CERN (see figure 1.9). The AMS-02 payload data are sent to the ground via the White Sands Facility to the GSC (Ground Support Computers) and POIC (Payload Operation Integration Center), both located at NASA/MSFC (Marshall Space Flight Center). The POCC is where AMS operations take place, including commanding, storage and analysis of housekeeping data and partial science data analysis for rapid quality control and feedback. At CERN there is also

the SOC (Science Operations Center), that receives and stores all AMS science and housekeeping data, as well as ancillary data from NASA, ensures full science data reconstruction, calibration and alignment, archives all data and keeps data available for physics analysis. In the control room of AMS, shifter are checking every day the health status of the experiment. There are mainly 6 different positions. The LEAD one is the most important. Lead shifter has to check all the AMS apparatus in collaboration with the other sub-detector shifters and the thermal one. The INFN Milano-Bicocca group has to cover the LEAD and DATA position. The DATA shifter controls the continuous flow of data from the experiment to the International Space Station, from the station to the AMS machines at NASA and from NASA to CERN. Other activities are related to train the new shifters and to develop new procedures to compare data on the ground with those recorded on a disc on the Space Station. The data missed or corrupted on the ground (e.g., due to interruptions in the transmission) are searched on the AMS laptop on ISS, marked and then re-downloaded, extending and improving the total quantity data of AMS-02.

Chapter 2

The Magnetosphere

The magnetic field around the Earth, the geomagnetic field, plays an important role in the modification of the CR trajectories near the Earth. The main field, originated inside our planet, can be considered as a magnetic dipole with an intensity of $\sim$ 0.6 G in the polar regions and $\sim$ 0.3 G in the equatorial one. This field is well known on the surface and can be described up to some thousands of km. The magnetic fields originated outside the Earth are variable and can be superimposed to the main field; this linear summation is no more valid for distances greater than several Earth radii (one Earth radius is $R_E \sim 6378$ km). A good description of the geomagnetic field is needed for untangling primary CR (coming from the outer magnetosphere) from secondary CR produced in the atmosphere or trapped in the radiation belts. The rigidity value used for discriminating these two families depends on many parameters and it is called geomagnetic rigidity cut-off, whose analytical formula was proposed by Störmer (see section 2.1). With his studies, it is possible to explore, for example, the East-West effect: an asymmetric angular distribution for particles with opposite charge (see section 2.2). The limit of the model is that the Störmer cut-off, equation (2.1), is not time dependent, while the magnetic field is variable (secular variation of the dipole orientation and intensity) and depending also from the solar activity. Another way to distinguish between the two particle's families is to do the so called "back-tracing", in other words, to reconstruct the particle trajectory back in time from the detection position up to the magnetosphere border (see section 2.3). Different models will be presented in section 2.4 and another way to determine the rigidity cut-off with a more complex magnetic field will be proposed in section 2.5. In conclusion, an application of our model, using the AMS-02 data, is presented in section 2.5.1.

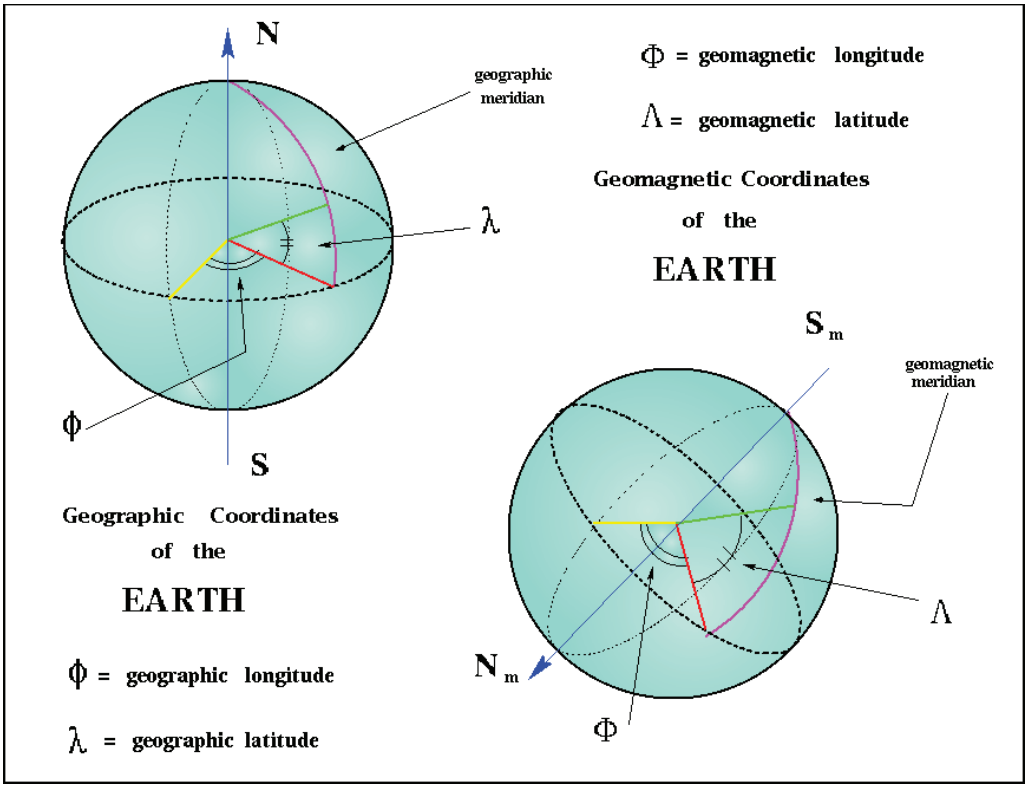

Figure 2.1: Geographic and geomagnetic reference frames.

Geographical vs Geomagnetic coordinates

The Geographic Coordinate system is defined with the X-axis in the Earth's equatorial plane and passing through the Greenwich meridian (longitude $\phi = 0°$). Its Z-axis is parallel to the rotation axis of the Earth, and its Y-axis completes a right-handed orthogonal set (latitude $\lambda = 0$ means equatorial region). The Geomagnetic Coordinate system has its Z-axis parallel to the magnetic dipole axis. The Y-axis points to the intersection between geographic equator and the geographic meridian 90 degrees east of the meridian containing the dipole axis. Finally, the X-axis completes a right-handed orthogonal set. Λ and Φ are the geomagnetic latitude and longitude respectively. The geographic coordinates of the dipole axis are derived from the International Geomagnetic Reference Field (IGRF[1]). It should be noted that the magnetic pole is moving with a speed of 2.6 km per year. Figure 2.1 reports the two coordinate systems[2].

[1]see `http://www.ngdc.noaa.gov/IAGA/vmod/igrf.html` (2014)
[2]Source `http://hpamsmi2.mi.infn.it/~wwwams/geo.html` (2014)

Internal magnetic field

The Earth's magnetic field was measured for the first time by Gauss in 1835. The geomagnetic field is originated inside the Earth by currents present in the liquid layers. The magnetic field is similar to a dipole, the center of which is offset from the center of the Earth of about 500 km and whose axis is tilted to the rotational axis by about 11°. For this reason, magnetic poles do not coincide with the geographical ones and their positions change slowly over the years. Its intensity varies over geological time-scales and, but not regular, it is also possible to have the reverse of the polarity. Tracks of these events is contained in the rocks observing the orientation of the crystals. The manner in which the Earth's magnetic field is modelled is through the decomposition into spherical harmonics. This analysis is also useful to distinguish the internal field from the external one, having available measurements at different heights from the ground to the satellites. The International Association of Geomagnetism and Aeronomy maintains and updates every five years a model of global field, hereafter the IGRF model. To develop it, they need satellite data and data from a network of ground-based observatories. The expansion in spherical harmonics is truncated to the 13^{th} degree, with 195 coefficients.

External magnetic field

The external magnetic field is not symmetric due to solar influence. In McCollough et al. (2008), an accurate analysis is made on several external models widely in use via the Office National d'Etudes et de Recherche Aérospatiales-Département Environnement Spatial (ONERA-DESP) libraries. In our work we concentrate the attention on the Tsyganenko models[3] that are semi-empirical best-fit representations for the magnetic field, based on a large number of satellite observations. The models include the contributions from major external magnetospheric sources: ring current, magnetotail current system, magnetopause currents, and large-scale system of field-aligned currents. The models adopted in this chapter are described as follow:

model T96: the spatial boundary of T96 is an hemi-ellipsoid on the dayside, which merges in the magnetotail with a cylindrical surface based on the average magnetopause of Sibeck et al. (1991). The field derives from the sum of five physically different magnetic field vectors, including contributions from the Chapman-Ferraro current ($\mathbf{B_{CF}}$), symmetric ring current ($\mathbf{B_{SRC}}$), cross-tail current sheet ($\mathbf{B_{TC}}$), large-scale field-aligned currents ($\mathbf{B_{FAC}}$) and partial penetration of the IMF into the model magnetosphere ($\mathbf{B_{INT}}$). The magnetic field

[3]see `http://geo.phys.spbu.ru/~tsyganenko/modeling.html` (2014)

data include measurements from IMP, HEOS, and ISEE satellites. The parameters of the model are the solar wind ram pressure p_{dyn}, Dst-index, transverse components (B_y and B_z) of the IMF and the dipole tilt angle. Each magnetic field source is a function of spatial position and model input parameters, where the function coefficients are determined by data fits (Tsyganenko 1995, 1996);

model TS05: TS05 was specifically developed to reproduce the storm-time magnetosphere. The field is confined within a dynamical magnetopause, based on the empirical model of Shue et al. (1997) where, on the nightside, its region of validity is limited to tailward distances $\leq 15\ R_E$. It is parametrized by dynamical solar wind inputs and includes a non-linear saturation of the field sources for strong solar wind conditions. The magnetic field data set for this model is based on 37 storm events that occurred between 1996 and 2000 and were observed by GOES, Polar, Geotail, and Equator-S satellites. TS05 model combines the T96 parameters with other six $(W_1, ..., W_6)$ defining the strengths of individual field sources; each parameter quantifies the combined effect of the interplanetary driving of the magnetospheric currents and their relaxation toward an unperturbed state (Tsyganenko & Sitnov 2005).

2.1 Rigidity cut-off

The effects of the geomagnetic field, on charged particles approaching the Earth, are mainly two. First of all, the trajectory of the incoming particle is curved leading to an arrival direction different from the one without the magnetic field. Second, an energy selection excludes low energy CR to reach the surface. The minimum rigidity value of a particle to enter from the outer magnetosphere is known as geomagnetic rigidity cut-off (R_{cut}). It depends on the arrival direction of the particles and the position of the observer located in the vicinity of the Earth. Particles with rigidity lower than the cut-off, which are located inside the magnetosphere, are trapped, and in particular climatic conditions and magnetic properties, they can create the polar aurorae; but if they are outside the magnetosphere, they can not penetrate inside and are reflected toward the interstellar space. Störmer (1956) described the geomagnetic rigidity cut-off as follow:

$$R_{cut}^{geo} = \frac{M}{r^2} \frac{\cos^4 \Lambda}{\left(\sqrt{1 - \sin\xi \sin\varphi \cos^3 \Lambda} + 1\right)^2}, \tag{2.1}$$

where M is the strength of the dipole moment, r the distance from the dipole centre, ξ the angle between the arrival direction with respect to the local magnetic Zenith, Λ the geomagnetic latitude and φ the arrival azimuthal angle of a positive particle. This last angle is null if the particles come from West, 90° if they come perpendicular on the surface and 180° if they come from East. Particles perpendicular to the surface, with same rigidity, prefer enter to the pole instead of the equator, in fact, the cut-off is proportional to $((\cos^4 \Lambda)$. The maximum cut-off on the surface (with $\varphi = 180°$) is $R_{cut}^{geo} = M/R_E^2 \simeq 59.6$ GV, where R_E is the Earth radius. Under cut-off only secondary particle, produced by interactions of primary CR with the atoms of the atmosphere and trapped by the geomagnetic field, are observable. Störmer's rigidity cut-off decreases if the detection geomagnetic latitude increases and also if particles arrival direction moves westward (East-West effect, see section 2.2). Finally, the CR intensity decreases increasing the rigidity cut-off. Thus, we expect an increment of the intensity if we move our observation direction from East to West and detection zone from equatorial to polar regions.

2.2 East-West effect

CR approaching the Earth are known to be almost isotropic (Munakata et al. 1997; Nagashima et al. 1998). According to the Lorentz force and knowing that CR are mainly constitute by positively charged particles, an asymmetric angular distribution is produced for those particles that reach low Earth orbit detectors. This azimuthal anisotropy is also called East-West effect, and was discovered in the 1930's. A difference between the intensities of cosmic rays arriving from the East and the West depending upon the charge of the primary particles where historically discussed by Rossi (1930). Johnson (1933, 1935); Rossi (1964) observed a deficit in the secondary cosmic rays (muons), produced in the atmosphere, arriving from the easterly direction with respect to the westerly direction. This azimuthal anisotropy depends on the position on the Earth, on particle rigidity and charge. At low rigidity, the effect is more visible. Three independent experiments (Johnson 1933; Alvarez & Compton 1933; Rossi 1934) found that the intensity is greater from the West, proving that most primaries are positive.

To show the separation that occurs between particles with opposite charge, we used the AMS-02 detector to explore this deviation angle of particles inside the magnetosphere. The complete analysis was presented as an Internal Note for the AMS-02 collaboration (Della Torre et al. 2013c). We considered protons, electrons and positrons collected by AMS-02 from July 2011 to March 2013. In order to

compare protons with electron and positron, we consider for this analysis the particle rigidity (R) measured in GV. Proton rigidity is obtained by the Tracker, while, for electrons and positrons, it is converted from the energy measured by the ECAL (E_{ECAL}) with:

$$R = \sqrt{E_{ECAL}(E_{ECAL} + 2E_0)}, \tag{2.2}$$

where E_0 is the electron rest energy. Particles between 10 and 50 GV were collected. The analysis was made for more than 1.6×10^8 protons, $\sim 1.1 \times 10^6$ electrons and $\sim 6 \times 10^4$ positrons. The study of the arrival directions of cosmic rays was made in a

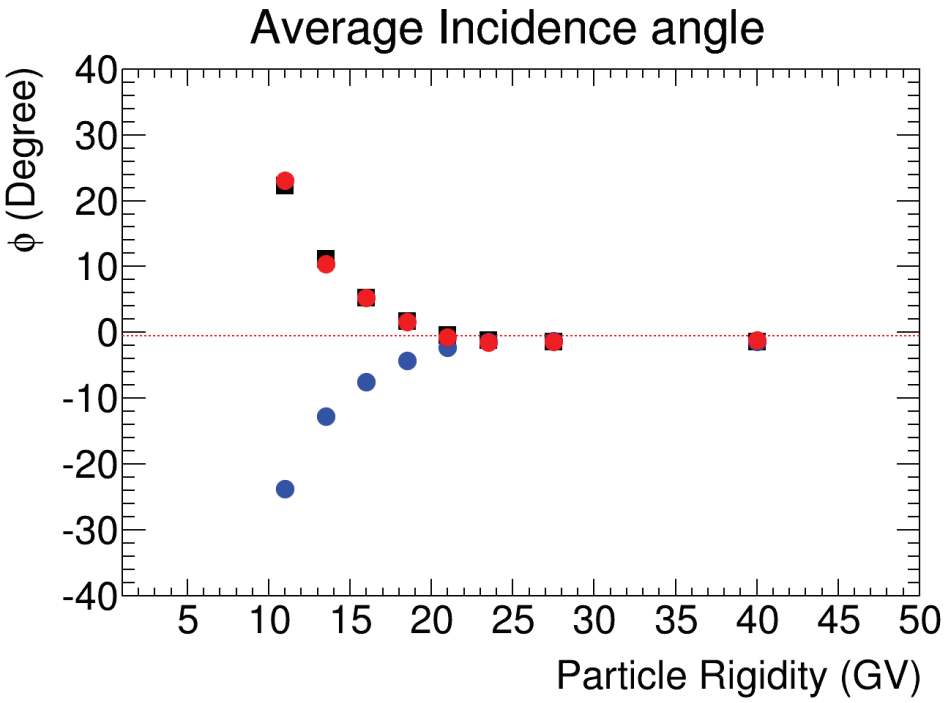

Figure 2.2: Average values of entrance angle in AMS-02 for protons (black), electrons (blue) and positrons (red) as a function of the rigidity. The dashed red line represent the mean value of the detector inclination in the frame considered ($\sim -0.6°$) (Della Torre et al. 2013c).

specific frame. This has the origin in the center of AMS-02, the azimuthal coordinate (φ) is parallel to geomagnetic longitude, positive geographic Westward, and the elevation coordinate (ϑ) is parallel to the geomagnetic latitude, positive geographic Southward. In this frame, for nominal ISS orientation, the pointing direction of AMS-02 is tilted of $-4° \sim -12°$ in the elevation coordinate, while it oscillates between -16° and 16° in azimuthal direction. This oscillation is due to an inclination of $\sim$12° of the detector with respect to the ISS local Zenith. The inclination of the ISS orbit allows the detector to be exposed to opposite directions during the North-to-South respect

to the South-to-North part of the orbit. The exposure time to geographic East and West direction is nearly the same. A mean value of the AMS-02 inclination in the chosen frame is $\sim -0.6°$. The East-West effect were observed analysing the arrival direction of protons, electrons and positrons along the φ longitudinal coordinate. The particles were divided into eight different rigidity bins from 10 to 50 GV. The mean values of the normalized counting rates, observed in the equatorial region (latitude $|\vartheta| < 10°$) at different φ, were reported in figure 2.2 as a function of the rigidity. Figure 2.2 shows the charge separation clearly visible at low rigidity. Positive particles (protons and positrons) access to the detector mainly from the geographic West side while negative particles (electrons) access mainly from the East direction. As expected, at higher rigidity the three distributions overlap one each others down to a difference of ~ 0.5 degree at rigidity greater than 23 GV. The same analysis was performed at different latitudes as shown in figure 2.3. The latitudinal regions are: β ($10° < |\vartheta| < 20°$), γ ($20° < |\vartheta| < 30°$), δ ($30° < |\vartheta| < 40°$) and ϵ ($40° < |\vartheta| < 50°$). The displacement effect due to the geomagnetic field

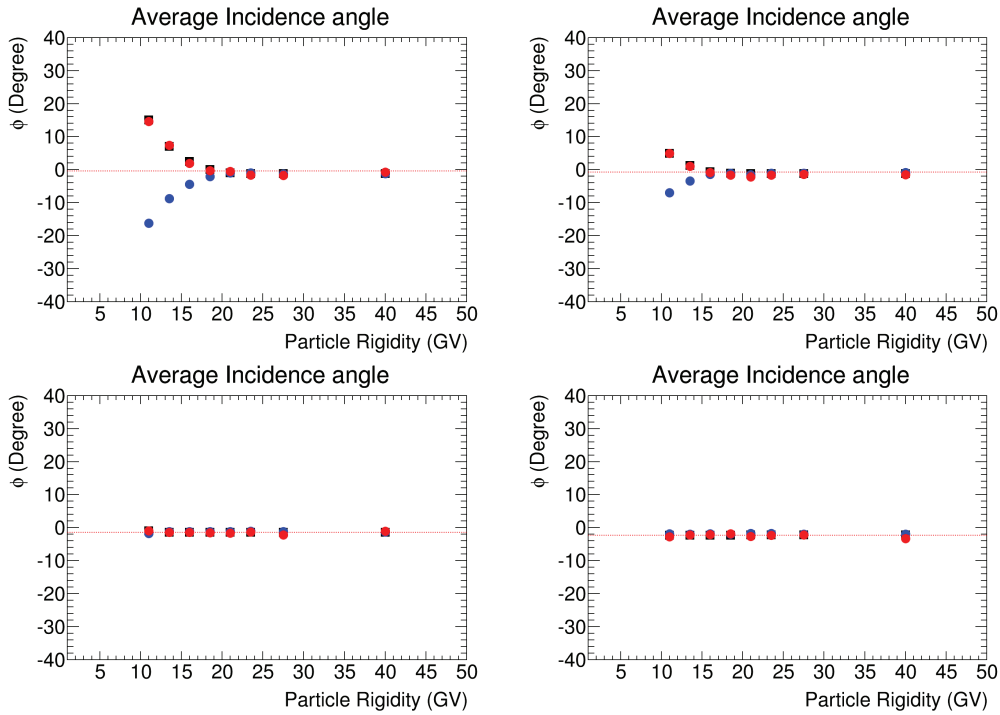

Figure 2.3: Average values of entrance angle in AMS-02 of Protons (Black), Electron (Blue) and Positron (Red) as function of rigidity and for several latitudinal regions. Starting from the top right, in clockwise direction, the presented regions are β, γ, δ and ϵ. The dashed red line represent the mean value of the detector inclination in the frame considered ($\sim -0.6°$) (Della Torre et al. 2013c).

decreases considering regions at higher latitude, where also the geomagnetic cut-off

decreases confirming the prediction.

2.3 Particle backtracing

As already mentioned, the geomagnetic rigidity cut-off discriminates between primary CR (coming form outside the magnetosphere) and secondary particles (trapped or generated inside the magnetosphere). Another method adopted to separate these two populations is to do back-tracing for each event, from the detector back to the edge of magnetosphere (for primaries), using a numerical code that includes accurate description of the geomagnetic field (see e.g., Bobik et al. 2005). The Milano-Bicocca group has developed a model of the magnetosphere referring to the Tsyganenko's studies. These models add to the well known internal dipole magnetic field also an external field, which is strongly asymmetric, with a tail that extends in opposite direction to the Sun. Having a good description of the magnetic field, the particle back-tracing from the detection position (e.g., the AMS-02 detector) to the magnetosphere border could be done using experimental data, such as solar pressure, coming from satellites around the Earth. The trajectory of the particle is reconstructed, in a unique way, according to its rigidity, arrival position and direction. For a better explanation of the back-tracing model adopted see e.g., Bobik et al. (2005, 2006a).

The code, developed by the Milano group, uses, as input parameters, the properties of the particle: mass, charge, rigidity, position (i.e., geographic coordinates) and incoming direction (reversed for back-tracing), date and time. We used different magnetic field models: IGRF as internal magnetic field, T96 or TS05 as external ones. The particle back-tracing gives us information related to the last point (position and direction) on the magnetosphere border (for primary particles), the time and length of the trajectory.

Before starting the reconstruction of the trajectory, the existence of the external parameters like the solar wind ram pressure p_{dyn}, Dst-index and transverse components (B_y and B_z) of the interplanetary magnetic field (IMF) at each given date are checked. If these parameters are available, they must to be also inside the following limits: p_{dyn} between 0.5 and 10 nPa, Dst-index between -100 and 20 nT, IMF-B_y and IMF-B_z between -10 and 10 nT (see e.g., McCollough et al. 2008, Table 4). For the TS05 models other six parameters are required; $(W_1, ..., W_6)$ are functions of solar wind density N_{sw}, speed V_{sw} and the southward interplanetary magnetic field B_z. After the checks on the parameters it is possible to start the reconstruction of the particle trajectory back in time. Figure 2.4 shows the particle trajectory reconstructed back in time using the magnetic field model (allowed and forbidden

trajectories are shown).

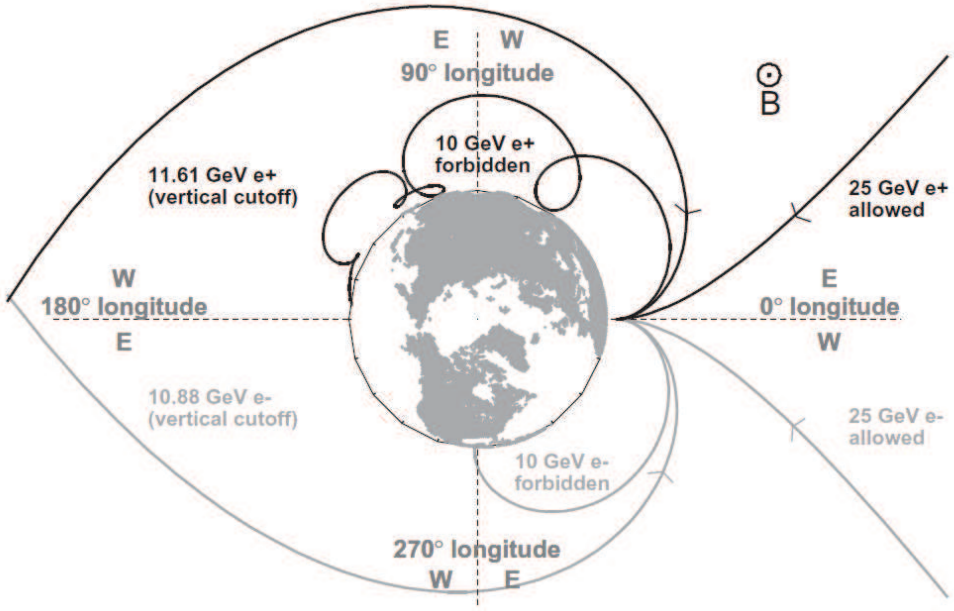

Figure 2.4: Illustration of electrons and positrons of different energies traced in the Earths magnetic field looking down on the North Pole. Depending on the cut-off, when the trajectory intersects the Earth it is taken to be forbidden (i.e., of secondary origin). Particles labelled as allowed are taken to be of Galactic origin (Ackermann et al. 2012a).

The motion equation is:

$$m\frac{d\vec{v}}{dt} = Zq\vec{v} \times \vec{B} \tag{2.3}$$

where m and Z are the relativistic mass and the number of elementary charges of the particle, $\vec{v}$ its velocity, q the electron charge and $\vec{B}$ the magnetic field. The propagation equation remains unchanged when the charge sign and the velocity of the particle are simultaneously reversed. In fact, to trace a particle back in time we used the strategy to reconstruct the trajectory of a particle with opposite charge that is going in the opposite direction. The two trajectories, if there are not energy losses, should be the same. The first step is the evaluation of the particle velocity from its rigidity. With the total magnetic field (internal IGRF-11 and external T96 or TS05 models), the Larmor radius is obtained:

$$r_L = \frac{m|\vec{v}|}{Zq|\vec{B}|} \quad \Rightarrow \quad \tau_g = \frac{2\pi r_L}{|\vec{v}|}. \tag{2.4}$$

Integration step is small enough that linear approximation is possible and a value of 10^{-3} with respect to the gyroradius is the right compromise between precision and time computation. The differential equation (2.3) is solved step by step using the Runge Kutta method. This method gives the numerical solution for ordinary differential equation. Starting from a differential equation as:

$$\frac{dy}{dt} = f(t) \tag{2.5}$$

with initial value $y(t_0) = y_0$, we can build the solution $y(t)$ moving from one point to the other using the Euler method as follows:

$$y_{n+1} = y_n + f(t_n, y_n)dt, \tag{2.6}$$

but in our Runge Kutta method we calculate the solution using the Taylor's expansion of the function $f(t)$ that for example at the second order is:

$$y_{n+1} = y_n + \frac{1}{2}h_n(f(t_n, y_n) + f(t_n + h_n, h_n f_n)), \tag{2.7}$$

where $f_n = f(t_n, y_n)$ and $h_n = t_{n+1} - t_n$. Our code uses 6^{th} order version that is faster and more precise. The Earth magnetopause is calculated using Sibeck or Shue equations (Sibeck et al. 1991; Shue et al. 1997). In the code we use the latest one (Shue). Particles are back-traced in time until they reach one of the two boundaries: the magnetopause (for primary CR) or again the AMS-02 altitude (secondary one). In the output of the code we have all the information related to the final point of the back-tracing, the total trajectory and a tag that indicates if the particle is coming from the boundary of the magnetosphere or if it is coming from an inner magnetosphere region. The TS05 model seem to be more precise especially in highly disturbed geomagnetic conditions, but it is anyway slower than T96, for this reason we made comparison between these models as reported in section 2.4.

The first analysis made with the reconstructed trajectories was the comparison between the starting and final points of the trajectory. We have done the back-tracing for $\sim 9 \times 10^7$ primary protons, $\sim 5 \times 10^5$ electrons and $\sim 4 \times 10^4$ positrons. The analysis was made evaluating the difference between the geographic longitude observed in the AMS-02 detector (ϕ_{AMS}) and geographic longitude reconstructed at the magnetopause (ϕ_{Mag}). As expected, positive particles come from higher longitude value and this difference is negative, while for negative particles occur the opposite phenomena. Figure 2.5 reports the total normalised distributions for each kind of particles. Figure 2.6, instead, shows the mean values of the different distribution as

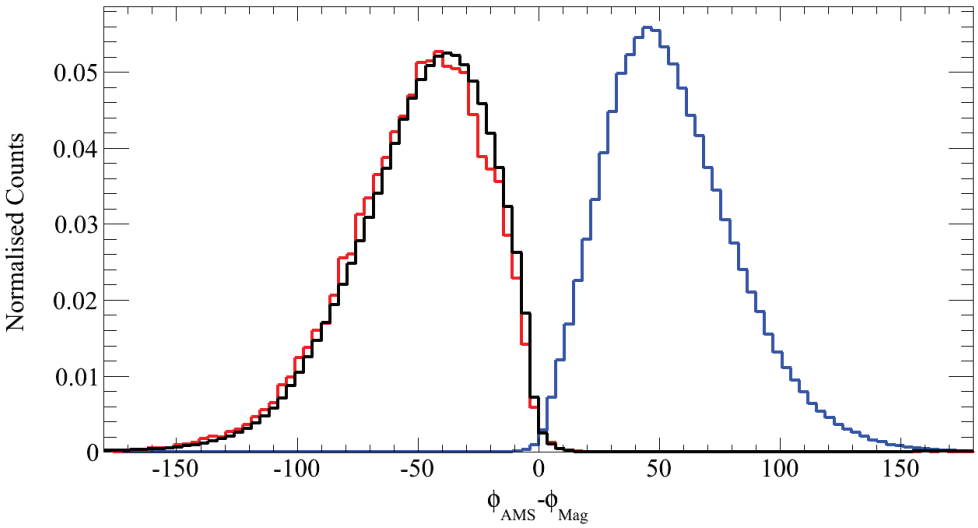

Figure 2.5: Normalised distributions of the difference between the geographic longitude detected in AMS (ϕ_{AMS}) and the geographic longitude at the magnetosphere border (ϕ_{Mag}) for primary protons (black), electrons (blu) and positrons (red).

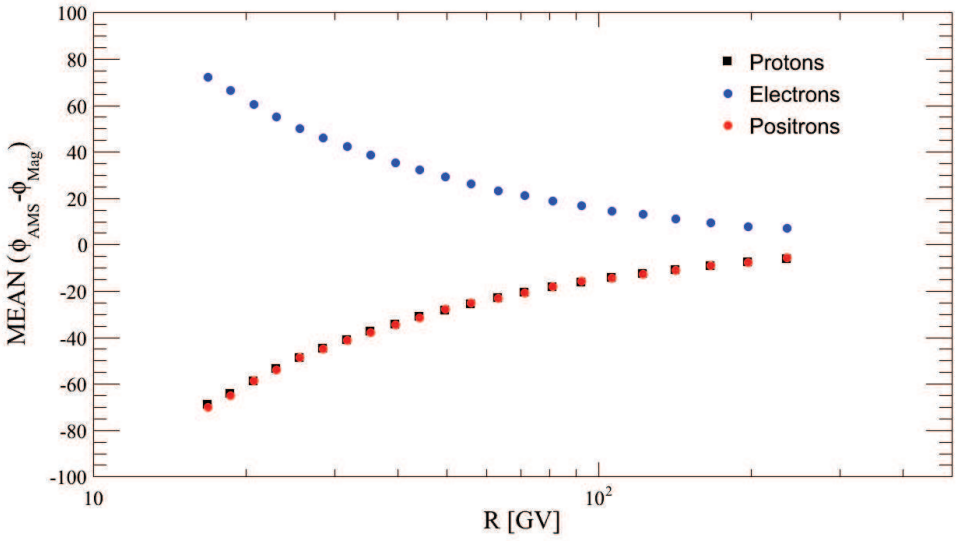

Figure 2.6: Normalised distribution of the mean value of the difference between the geographic longitude detected in AMS (ϕ_{AMS}) and the geographic longitude at the magnetosphere border (ϕ_{Mag}) as a function of the rigidity for primary protons (black), electrons (blu) and positrons (red).

a function of the rigidity. Looking at the points in figure 2.6, we can estimate, for 100 GV particles, an average deviation, inside magnetosphere, of about 20°.

2.4 Comparison of the models

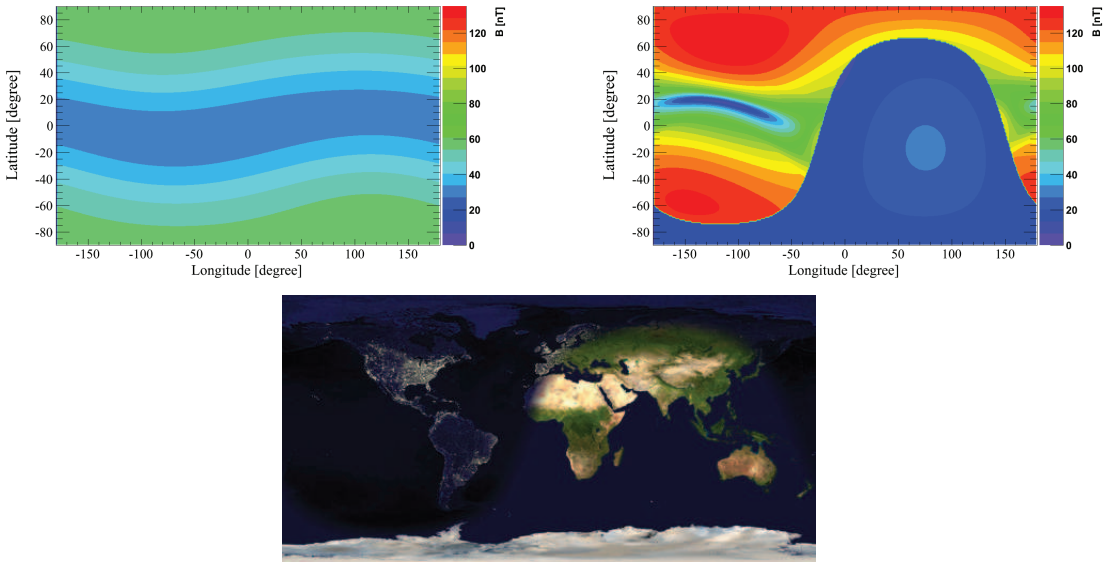

Figure 2.7: Magnetic field at 10 R_E for only internal IGRF field (top left) and for both internal IGRF and external TS05 models (top right). The bottom figure represents the day and night side, corresponding to the time of the simulation, source: `http://www.fourmilab.ch/cgi-bin/uncgi/Earth/action?opt=-p` (2014).

As reported in Boschini et al. (2013); Bobik et al. (2013b) we evaluated the effective need of an external field model. A macroscopic difference is that the IGRF representation of the geomagnetic field is essentially symmetric, while the magnetosphere is highly asymmetric, thus, the introduction of the external magnetic field seems the only possible solution. In our study we found the day-night asymmetry in the calculated B_{tot} values only with external field, perfectly corresponding to the day-night sides (see figure 2.7).

We started to compare our model predictions with the IMF data measured by satellites. Previous studies (see e.g., Huang et al. 2008; Zhang et al. 2010) demonstrated how the evolution of the Tsyganenko models was in the direction of a better agreement with measurements. Zhang et al. (2010) compared the T02 model with CLUSTER measurements, while Huang et al. (2008) shows the comparison between the TS05 model, in a period of strong negative B_z component, with GOES-8 data.

Starting from these two previous works we performed some simple tests, comparing our model calculations with both CLUSTER (for the year 2004) and GOES-8 data (during a period in 1998). As can be seen in figure 2.8 the agreement with IGRF+TS05 is much better than the only IGRF model.

The comparison with and without external field forced us to use the last one for our back-tracing. Moreover, we tested both T96 and TS05 models testing the differences in the outputs. With a sample of 2.5×10^6 simulated protons, almost 20% of them show a different nature (forbidden vs allowed trajectories) if the external field is or not used (see table 2.1). This overall difference is mainly located at high latitudes where its value is close to 100%. The difference between the two external field models, both with IGRF as internal field, is less than a 10%.

We focused our attention only on primary CR and we evaluated the accuracy

Models	IGRF	IGRF + T96	IGRF + TS05
IGRF	0%	21.5%	19.8%
IGRF + T96		0%	9.5%
IGRF + TS05			0%

Table 2.1: Different nature of particles, allowed or forbidden trajectoies, with different magnetic field models.

in the reconstructed trajectories using the T96 and TS05 models. Fixed the Shue magnetosphere model (Shue et al. 1997), we evaluated the difference in final points as a function of rigidity bins (20-30 GV, 30-40 GV, 40-50 GV and >50 GV) on a sample of 2.2×10^5 electrons detected by AMS-02 in the period between June 2011 and September 2012. First of all we show in figure 2.9 the differences, separated in latitude (λ) and longitude (ϕ) with and without the external field model TS05, where increasing the rigidity the differences decrease. For the longitude plots, the asymmetric shape is clearly due to the East-West effect. Comparing these plots with the differences between the two external field models (see figure 2.10), RMS is reduced also at low rigidity. By inspections of figure 2.10, the external field models are consistent and essential for this kind of study. In table 2.2 we report the percentage of particles for which the difference in the last reconstructed point on the magnetopause differs for more than 0.5°. The data are divided into two samples: when the solar wind pressure is below or above a mean value of $\sim$ 4 nPa. As expected from the fact that TS05 is modelled starting from high disturbancy period, in the first case ($p < 4$ nPa) the agreement is better than the second case.

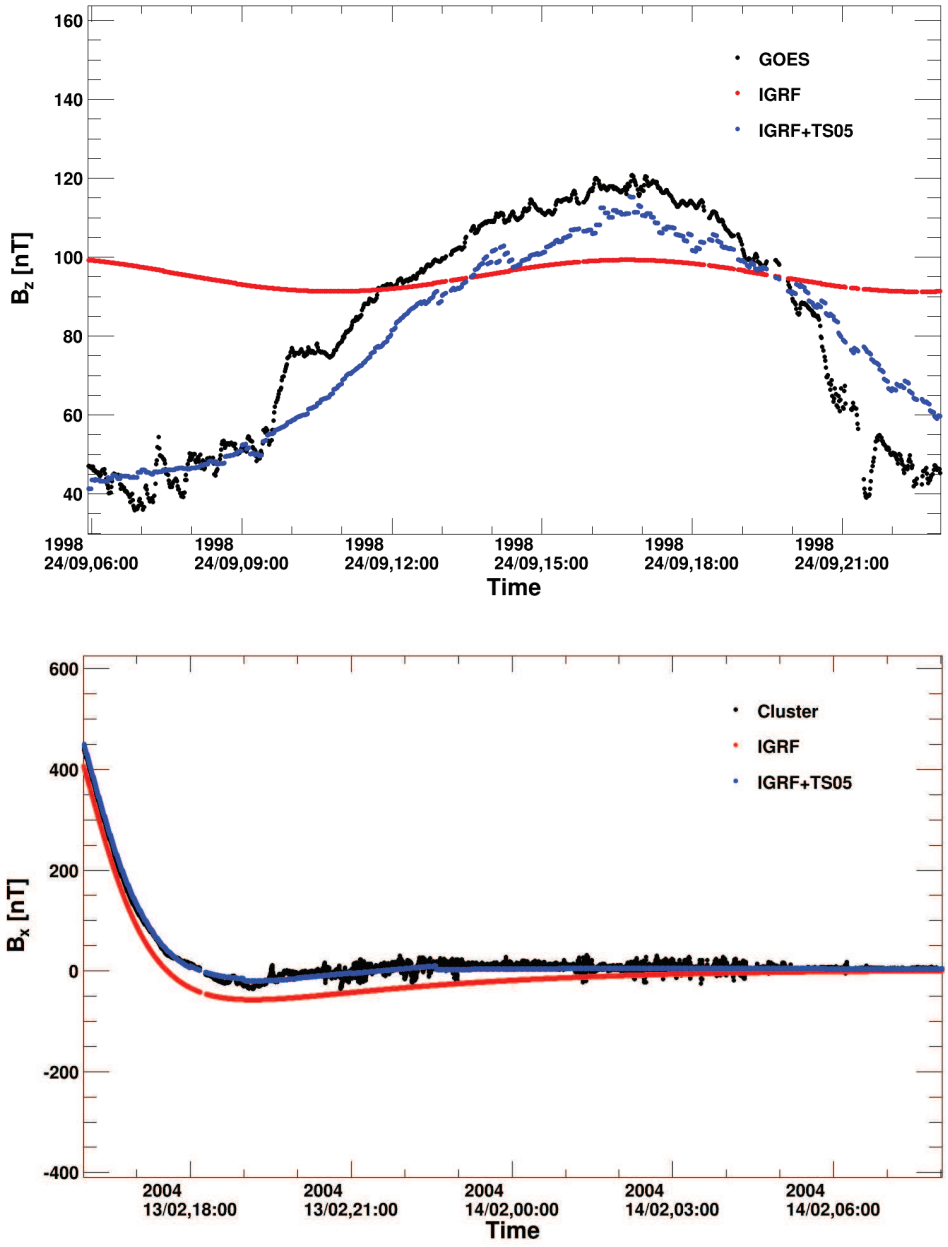

Figure 2.8: Comparison among GOES B_z-data (top panel), collected in 1998, CLUSTER B_x-data (bottom panel), collected in 2004, internal (IGRF) and internal plus external (IGRF+TS05) models (5 minutes resolution).

	All	$p < 4$ nPa	$p > 4$ nPa
$> 0.5°$ IGRF-TS05	78.8%	78.4%	85.1%
$> 0.5°$ T96-TS05	10.6%	9.4%	38.8%

Table 2.2: Percentage of particles with last point difference greater than 0.5° for IGRF-TS05 and T96-TS05 - rigidity bin 20-30 GV.

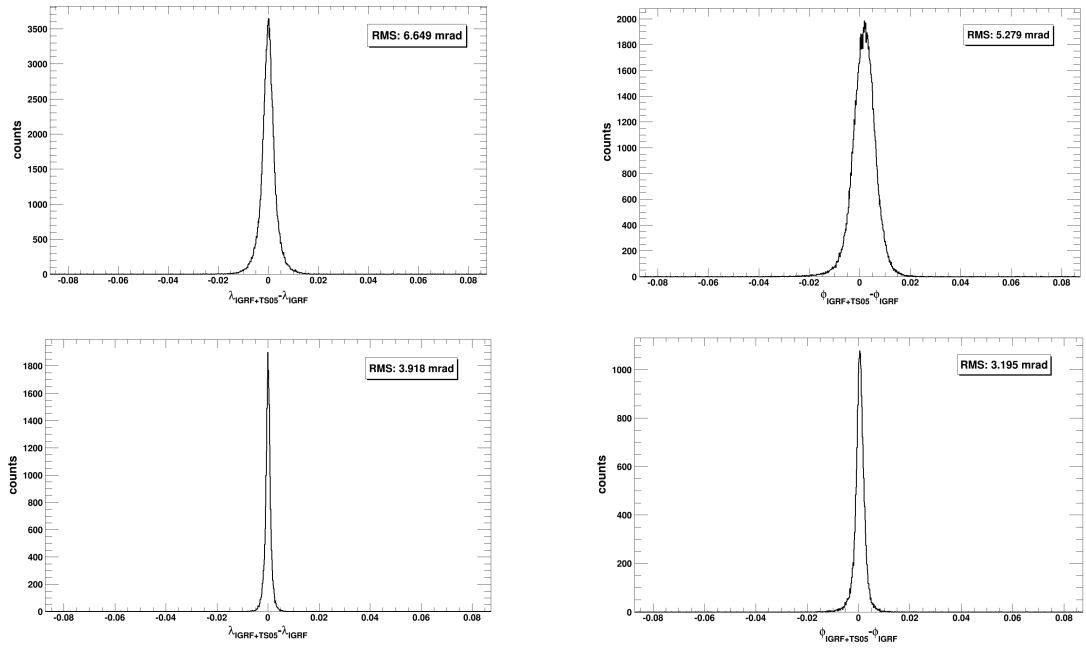

Figure 2.9: Latitudinal (left) and longitudinal (right) difference of last point (magnetopause) for electrons in the rigidity range between 20 and 30 GV (upper), and for rigidity above 50 GV (lower) for IGRF and IGRF+TS05 fields (Bobik et al. 2013b).

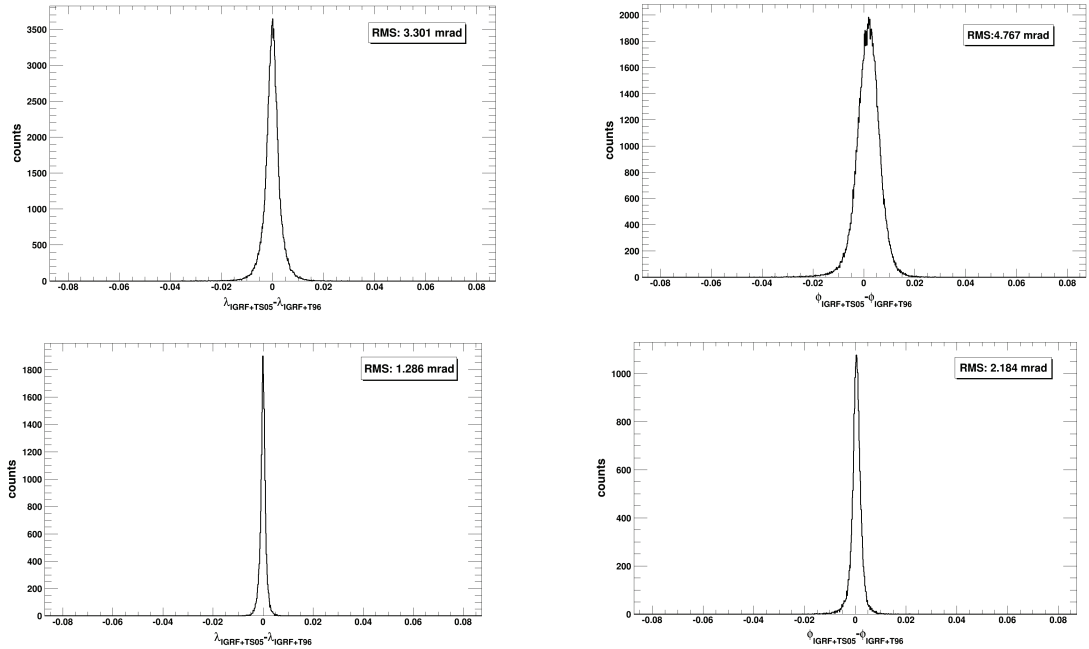

Figure 2.10: Latitudinal (left) and longitudinal (right) difference of last point (magnetopause) for electrons in the rigidity range between 20 and 30 GV (upper), and for rigidity above 50 GV (lower) for IGRF plus external field models T96 or TS05 (Bobik et al. 2013b).

2.5 Rigidity cut-off with TS05 model

Using the internal (IGRF) plus external (TS05) magnetic field models it is not yet possible to write a simplified expression for the particle cut-off as in the Störmer case, see e.g., equation (2.1). In fact, this value should depend on many factors concerning not only the particle properties, but also the surrounding environment that is time dependent. To determine a discriminating rigidity factor, above which particles are primary, can be done as follow. Starting from the particle back-tracing in different magnetosphere configurations (e.g., different solar conditions) it is possible to evaluate, for a particular geographic region or a specific time binning, a rigidity range in which both particle's family (primary and secondary CR) are present. In this way it is possible to determine, by means of the back-tracing, the minimum rigidity of the primaries (in the sample) and the maximum rigidity of the secondaries.

In our case, we divided the geographic map (latitude and longitude) into cells of $2^\circ \times 2^\circ$. For each particle belonging to 76 random days, chosen during the three years of AMS-02 data taking, we have done the back-tracing and, for each cell, we registered the primary CR with the minimum rigidity and the secondary CR with the maximum rigidity. The map with the minimum rigidity of primaries indicates that a particle detected with rigidity below that values is, in a very good approximation, a secondary CR. Vice versa, the map with the maximum rigidity of secondaries ensures that particles detected with an higher rigidity are essentially primaries CR. Figure 2.11 concern all protons collected by AMS-02 in those 76 days (from July 2011 to June 2013) with an opening angle of 40 degree with respect to the z-axis of the experiment. The big hole at about -25 degree latitude and about -50 degree longitude in the maps is the South Atlantic Anomaly (SAA), always excluded from this analysis. The SAA is the region where the bottom part of the Van Allen belts is closest to the surface of the planet; in this area the intensity of cosmic radiation is greater than in any other area of the Earth. The top panel regards the analysis with the only IGRF internal field; while the bottom one represents the TS05 cut-off. Analysing this latter panel of figure 2.11, it is possible to see that the maximum rigidity cut-off reaches value lower than 30 GV in the magnetic equatorial region and decrease below 5 GV near the magnetic poles.

The differences between the IGRF plus TS05 model and the only IGRF one is emphasized by figure 2.12, where we made the ratio between the bottom and the top maps in figure 2.11 under the same conditions. Figure 2.12 shows a central region, in geographic coordinates, with a rigidity cut-off, coming from the back-tracing with both internal and external magnetic field, higher ($\sim 20\%$ more) with respect to the one produced with the only IGRF model. While, in the other regions, the ratio is

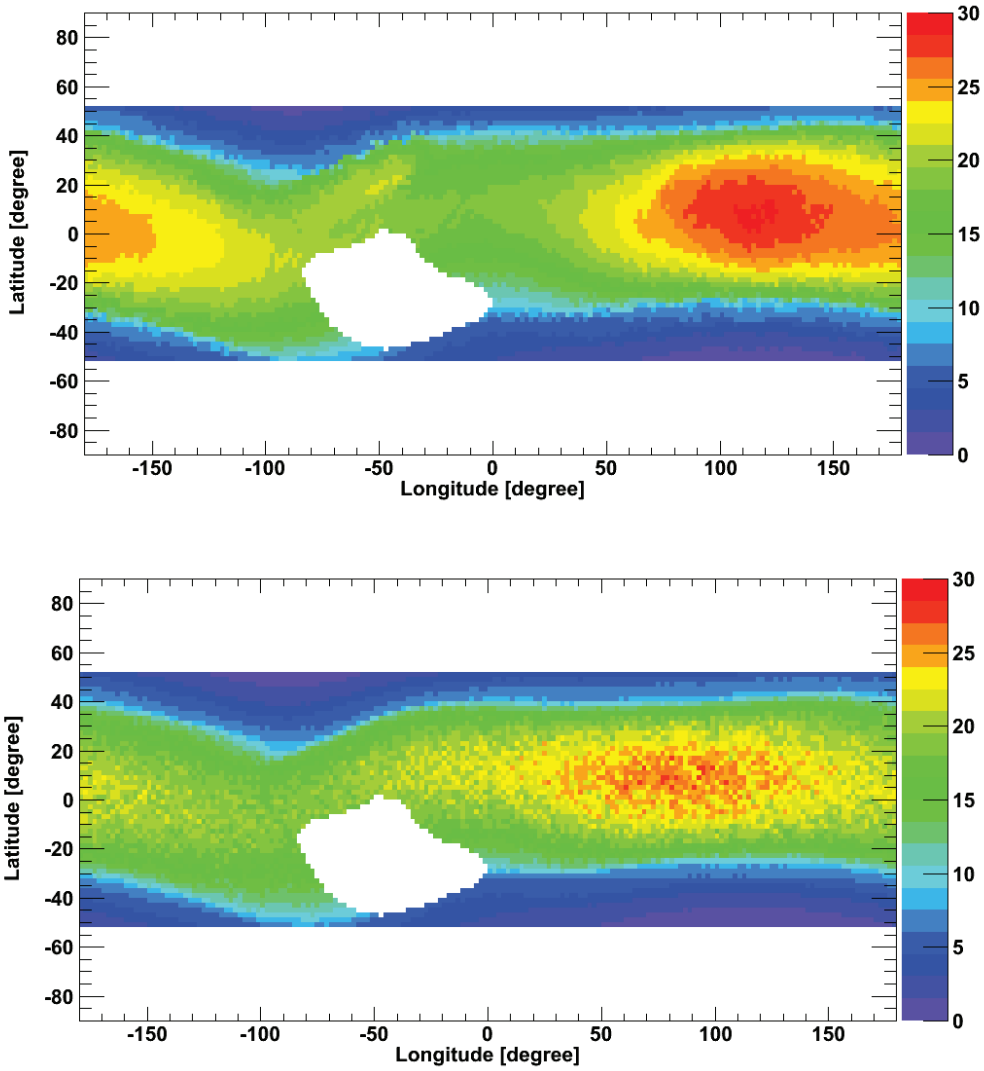

Figure 2.11: Geographic maps, divided in $2° \times 2°$ cells, with the rigidity cut-off using the only IGRF model (top panel) and the maximum secondary CR rigidity (bottom panel) using both internal-IGRF and external-TS05 models. The color intensity is proporzional to the particle rigidity. The opening angle in the particle selection is 40 degree with respect to the AMS-02 z-axis.

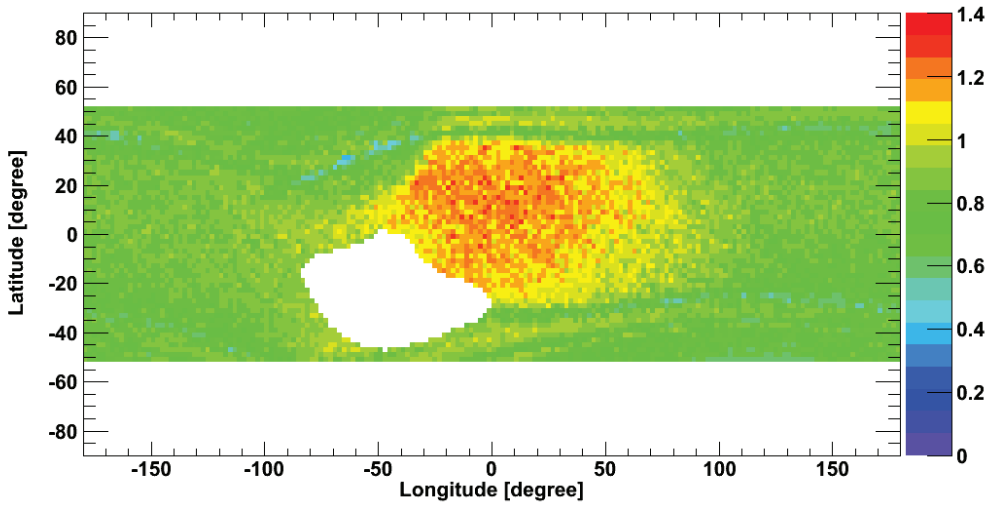

Figure 2.12: Ratio between the map with the maximum rigidity cut-off found using internal (IGRF) and external (TS05) field models (bottom graph of figure 2.11) and the same map using the only IGRF model for the backtracing (top graph of figure 2.11).

equal or lower.

We made the same analysis reducing the opening angle, i.e., selecting protons with arrival directions inside 25 degree with respect to the AMS-02 z-axis. The difference between the two opening angles regards the AMS-02 geometry and the kind of CR analysis. Analysis requiring particles in the inner tracker (layers 2-8) acceptance (opening angle of 40 degree) are characterised by higher statistics and lower maximum detectable rigidity ($\sim$ 250 GV) (Zuccon, P. et al. 2013). Using the full span approach (tracker layers 1-9), the acceptance of the experiment is restricted to an opening angle of 25 degree, the statistics is lower than the previous one and the maximum detectable rigidity increases up to $\sim$ 2 TV (Zuccon, P. et al. 2013). The maximum rigidity for secondary particles collected in an opening angle of 25 degree are reported in figure 2.13. The graph in figure 2.13 shows lower rigidity cut-off with respect to the bottom panel of figure 2.11 due to the closer opening angle that inhibits the entrance of high energy secondary particles in the experiment.

2.5.1 Primary particles

The studies reported in this chapter lead to two main results. The first one regards the incoming particle direction reconstructed at the magnetopause. This leads to observe the isotropy or anisotropy of the CR-sky showing the areas where these

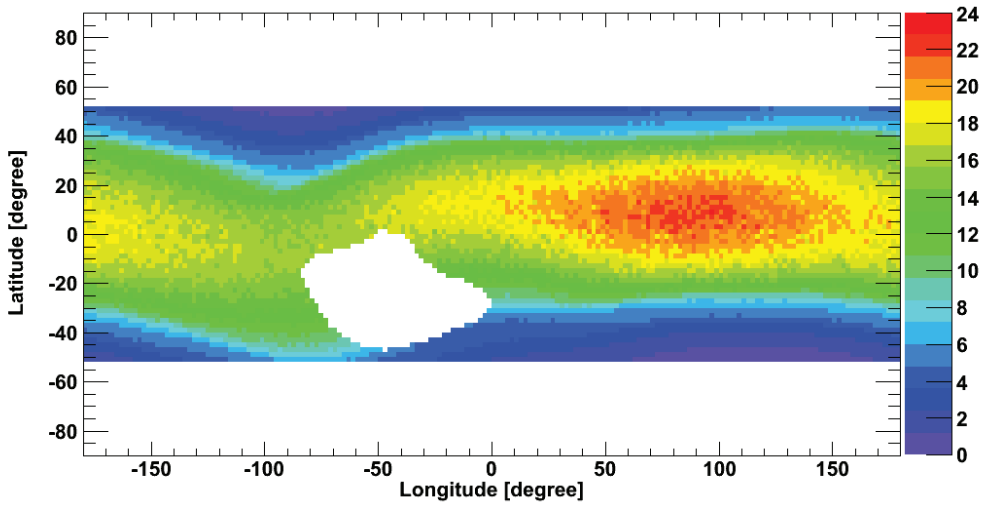

Figure 2.13: Geographic maps, divided in $2° \times 2°$ cells, with the rigidity cut-off using both internal-IGRF and external-TS05 models. The color intensity is proporzional to the particle rigidity. The opening angle in the particle selection is 25 degree with respect to the AMS-02 z-axis.

particles could be produced. As already mentioned, magnetic fields influence the trajectory of the particles. Thus, the back-tracing technique can be used to reconstruct the final position and direction at the magnetopause creating a map of asymptotic direction at the magnetosphere border. We will remind that the geomagnetic field is the highest field experienced by CRs in the proximity of a detector in low Earth orbit as AMS-02. I will discuss later, in section 4.3, the anisotropy of the arrival directions of CR.

The second main result is related to the CR spectrum at lower rigidity (that, for the AMS-02 experiment in nominal conditions, imply $R \lesssim 30$ GV, see e.g., figure 2.11, top and middle panels). Below approximately this limit, the geomagnetic field plays an important role in the modification of the particle trajectory. Starting from the detection position, the particle back-tracing shows allowed and forbidden trajectories. CRs that reach the Earth surface, coming from the outer magnetosphere, describe allowed trajectories, while CRs with rigidity lower than the local geomagnetic cut-off are produced in atmosphere or trapped in the radiation belts and they can not reach the boundaries of this region. Thus, for rigidity lower than about 30 GV, primary particles must be well separated among those reaching the AMS-02 position. The other particles can be even separated in two populations: secondary and trapped ones. Following this second approach, we analysed the AMS-02 data over an integral period of three years, from July 2011 to June 2013. Using optimised

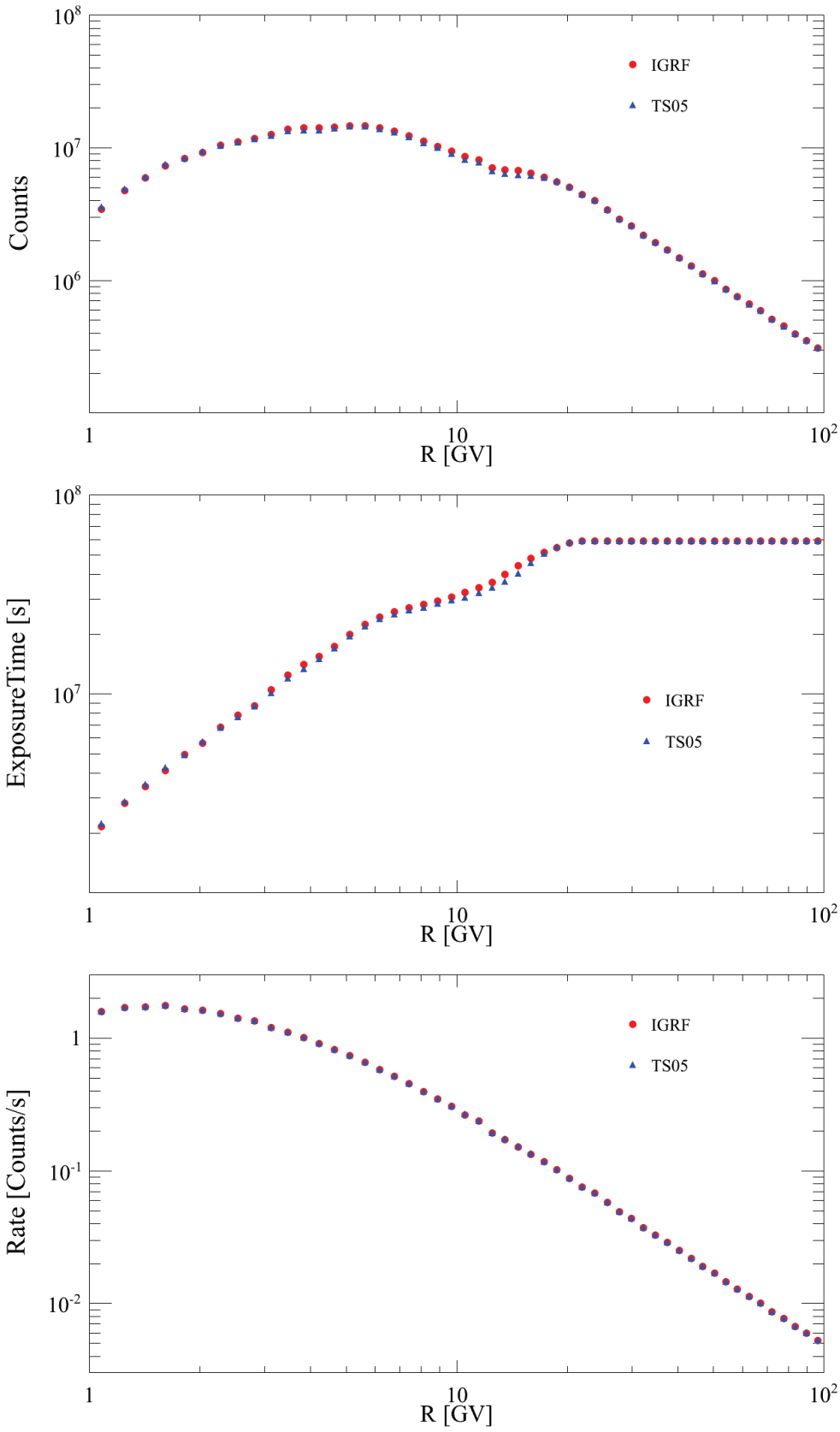

Figure 2.14: Proton counts, exposure times and rates for an opening angle of 25 degree. Red points represent the analysis made with the only IGRF model, while blue ones the analysis adding the TS05 external field model.

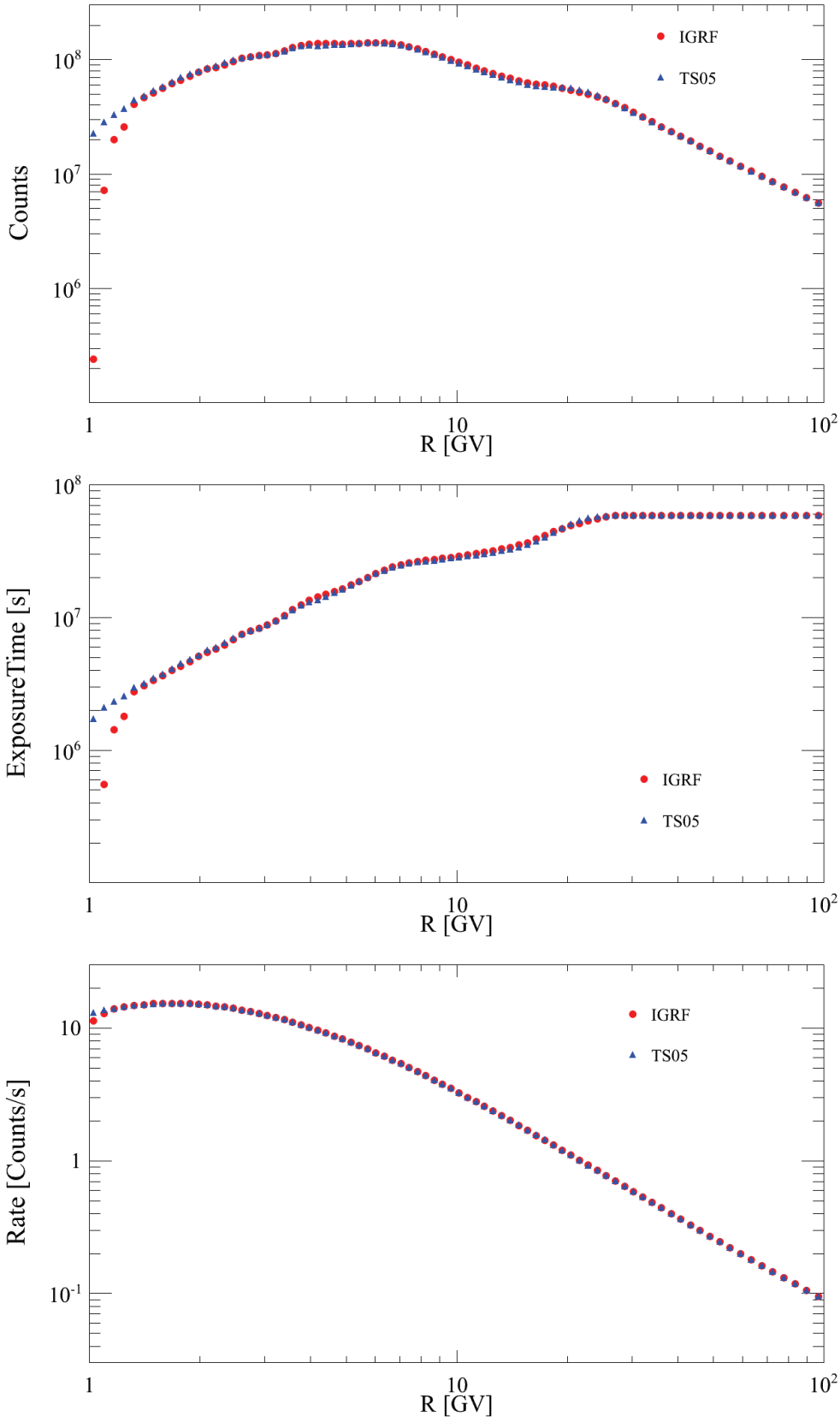

Figure 2.15: Proton counts, exposure times and rates for an opening angle of 40 degree. Red points represent the analysis made with the only IGRF model, while blue ones the analysis adding the TS05 external field model.

cuts, provided by the collaboration for the protons identification, we evaluated the particle rate (ratio between particle counts and exposure time) for the full period. In the first case, we selected protons above the IGRF cut-off; while, in the second one, we collected protons above the rigidity cut-off provided by the bottom map of figure 2.11 and figure 2.13.

The proton counts, exposure times and rates for an opening angle of 25 degree (figure 2.14) and 40 degree (figure 2.15) with respect to the AMS-02 z-axis. The red points represent the analysis made with the only IGRF model, while blue ones the analysis adding the TS05 external field model. To emphasized the difference between the two analysis (the rates where we used the only IGRF and the IGRF plus TS05 models), we made the ratio between them. The ratio using an opening angle of 25 degree is reported in the top panel of figure 2.16. The differences are inside 2% over the full rigidity range. The maximum discrepancy appears between 10 and 20 GV, where the two magnetic field models are more different in the geographic equatorial region (25 degree means to use a very narrow opening angle and the cut-off is more or less the vertical one). The bottom graph of figure 2.16 represents the same things, but with a 40 degree as opening angle. The differences are inside 2% down to ~ 1 GV, where the discrepancy increases in the geographic pole regions.

We want to remark that this preliminary analysis is performed above a very wide AMS-02 data taking period. Higher discrepancy can be observed in days affected by strong solar events like flares or coronal mass ejections (CME). Differences above three years of data are contained into 2% over the full rigidity range. This result is reported in Aguilar et al. (2015) for the evaluation of the proton flux observed with AMS-02.

A step forward, using the IGRF plus TS05 magnetic field models, is to study the secondary CR. Figure 2.17 reports the minimum rigidity of primaries in geographic coordinates. For each cell, all the rigidity values between the minimum primary (figure 2.17) and the maximum secondary (figures 2.11 and 2.13) are described by a transmission function as reported in Bobik et al. (2006b). An almost pure sample of secondary protons, produced in atmosphere and trapped in the geomagnetic field, are represented by particles with rigidity lower than the one reported in figure 2.17.

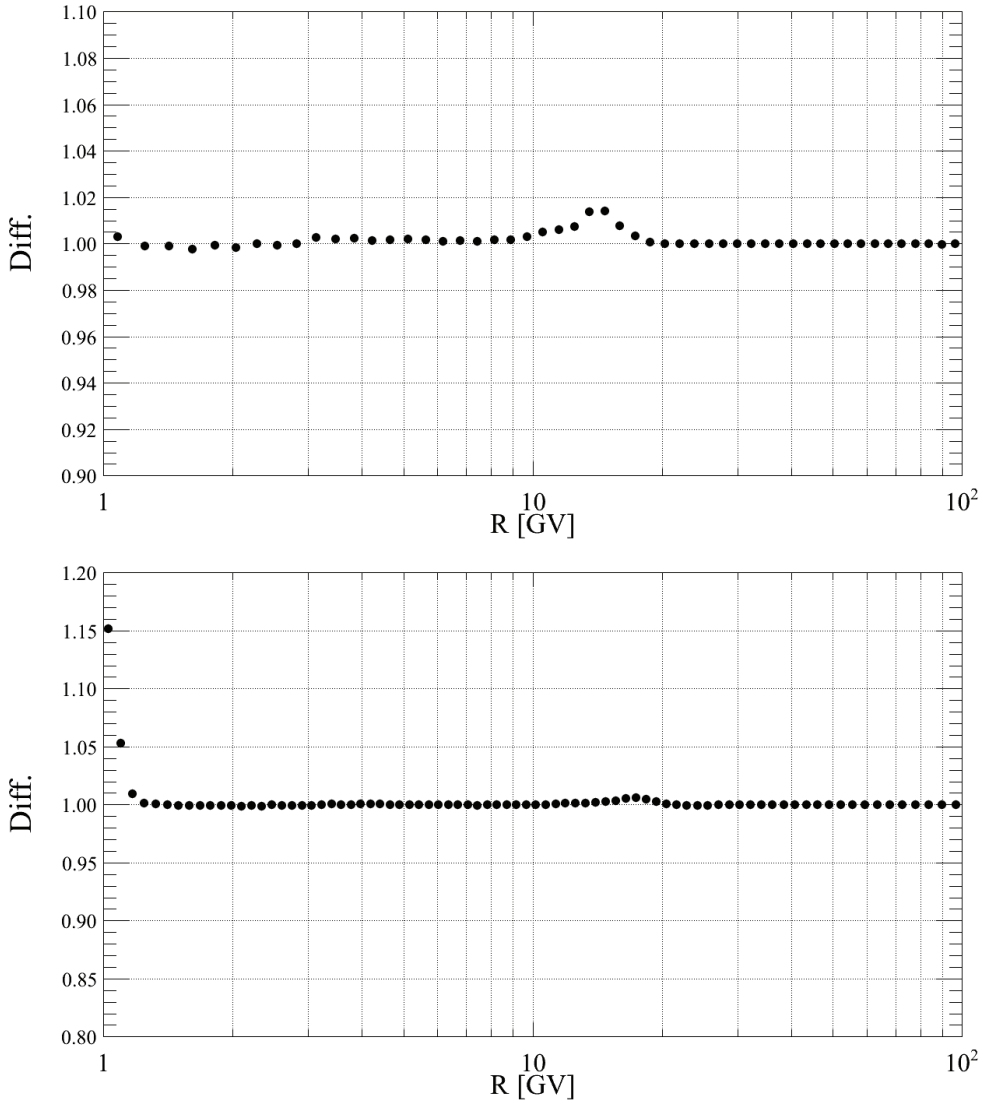

Figure 2.16: Ratio between the proton rate evaluated using the TS05 plus IGRF magnetic fields model with respect to the only IGRF one for the opening angle 25 degree (top panel) and 40 degree (bottom panel).

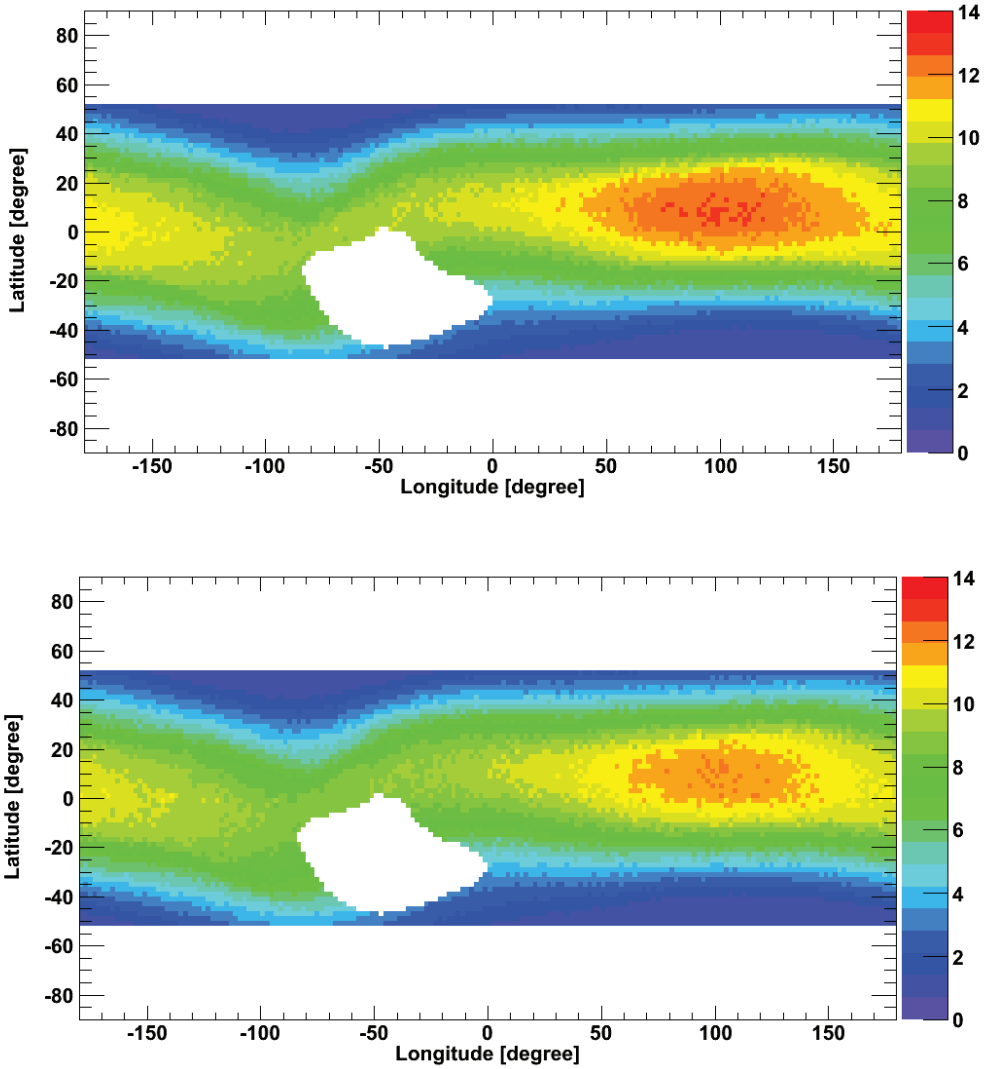

Figure 2.17: Geographic maps, divided in $2° \times 2°$ cells, with the rigidity of the minimum primaries in 25 degree (top panel) and 40 degree (bottom panel) of opening angle, using both internal-IGRF and external-TS05 field models. The color intensity is proporzional to the particle rigidity.

Chapter 3

Local Interstellar Spectra above modulated energies

Above $\sim$ 10 GeV, it is commonly acknowledged that, inside the heliosphere, particle propagation is no longer affected by solar modulation, thus the omnidirectional distribution is the one determined by the local interstellar spectrum (LIS), that is the one observed in the ISM. Cosmic rays are commonly divided into two categories: primary and secondary. Primary cosmic rays are those particles that are produced by sources e.g., throughout the life of the stars and especially in the final stage, when the gravitational collapse, supernovae and remnants of these explosions emit large quantities of energy releasing and accelerating ions and electrons in the interstellar medium. During the travel in the Galaxy it is possible that these particles interact with the atoms of the ISM and with electromagnetic radiation losing energy and creating new particles, resulting, for example, from the fragmentation of the nuclei involved. These particles are called secondary cosmic rays (see section 3.2). In this chapter, we focus the attention on CR electrons and positrons. Recent experiments, PAMELA and AMS-02, have been recording these particles in space for some years. Their data confirm that, at $\sim$ 10 GeV, the electron flux is $\sim$ 1% of the proton one, while the positrons are $\sim$ 8% of the electrons (see section 3.1). We divide electrons and positrons in primary and secondary particles. For instance, the main component of the electron spectrum is that produced by supernova remnants, while positrons were supposed to be mainly originated from the decay of muons produced by CR interactions with the ISM (see section 1.2 and e.g., Moskalenko & Strong 1998); these particles are commonly referred to as secondaries. Primary plus secondary CR spectra outside the region interested by the solar activity (i.e., the heliosphere) are known as local interstellar spectra. Moreover, we will refer to electrons produced in SNR and in the ISM as the "classical" electron LIS and to positrons produced

in the ISM as the "classical" positron LIS (e.g., "classical" LIS, hereafter cLIS). In section 3.3, a cosmic ray propagation code (GALPROP) is used to determine these spectra and comparisons with the experimental ones are reported in section 3.4. The propagation of electrons and positrons is characterized by an high energy loss rate due to interactions with the magnetic and radiation fields. For this reason, sources of high energy CR electron or positron must be located in a very close region (distance lower than ~ 2 kpc) from our Solar System (section 3.5 3.6). We will discuss other primary sources of electrons and positrons in chapter 4.

3.1 Recent experimental data

Before 2006, more than ten experiments measured the cosmic ray electron and positron fluxes between 0.1 and 100 GeV. Hereafter, we will report the references and the data-taking period corresponding to the different experiments: AMS01 (1998/06) (AMS-01 Collaboration et al. 2007; Alcaraz et al. 2000), AESOP00 (2000/08) (Clem & Evenson 2002), AESOP02 (2002/08) (Clem & Evenson 2004), AESOP06 (2006/08) (Clem & Evenson 2009), AESOP94 (1994/08) (Clem et al. 1996), AESOP97+98 (1997/09 and 1998/08) (Clem et al. 2000), AESOP99 (1999/08) (Clem & Evenson 2002), CAPRICE94 (1994/08) (Boezio et al. 2000), CAPRICE98 (1998/05) (Boezio et al. 2001), HEAT94 (1994/05) (Barwick et al. 1998), HEAT94+95 (1994/05 and 1995/08) (DuVernois et al. 2001), HEAT95 (1995/08) (DuVernois et al. 2001), HEAT-pbar (2000/06) (Beatty et al. 2004), MASS91 (1991/09) (Grimani et al. 2002), TS93 (1993/09) (Golden et al. 1996).

The first surprising result of PAMELA experiment arrived in 2009 when the collaboration published the positron fraction, that is the ratio of positron flux to the sum of electron and positron fluxes $\phi_{e^+}/(\phi_{e^+} + \phi_{e^-})$, in the energy range between 1.5 and 100 GeV (Adriani et al. 2009). The data sample were updated one and two years later (Adriani et al. 2010; Adriani et al. 2013). In all cases, an anomalous positron abundance with respect to the theoretical model predictions was observed (see e.g., section 3.3 and 3.4). For the first time, the positron fraction, above the region affected by the solar modulation ($E \gtrsim 10$ GeV), increases with the energy. In few years also the FERMI[1] (Ackermann et al. 2012b) and AMS-02 experiment (Aguilar et al. 2013) confirmed this unexpected slope (see Figure 3.1). For these experiments, the misidentification of protons is the largest source of background in the positron fraction estimation. This can occur if electron- and proton-like interaction patterns are confused in the calorimeter or TRD data. The proton-to-positron

[1]See Appendix B for few information regarding the FERMI experiment

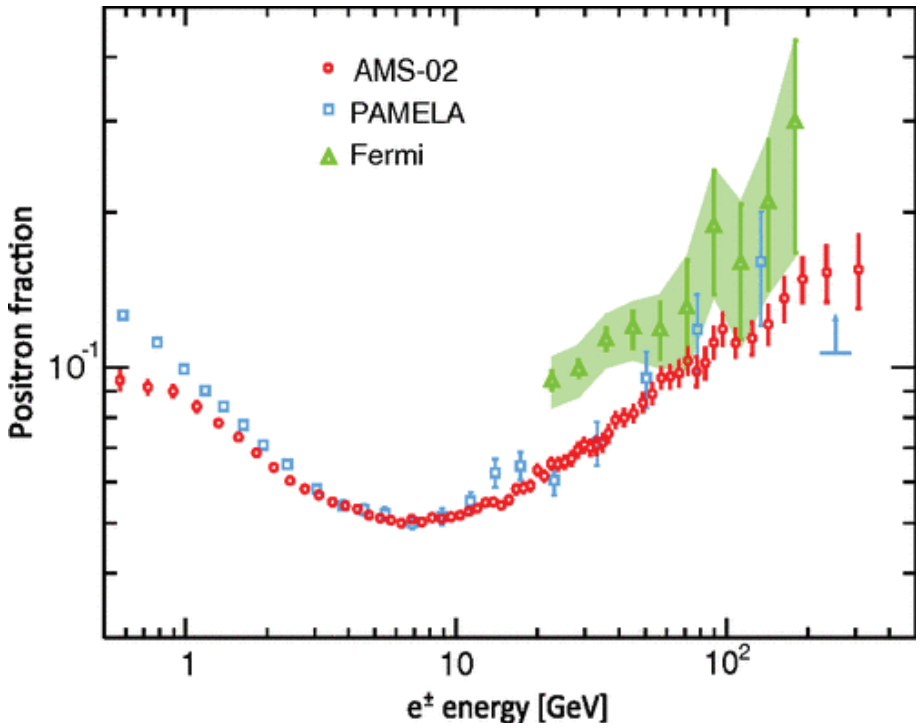

Figure 3.1: Positron fraction recorded by PAMELA (Adriani et al. 2013), FERMI (Ackermann et al. 2012b) and AMS-02 (Aguilar et al. 2013) experiment.

separation increases from approximately 10^3 at 1GV to approximately 10^4 at 100 GV for PAMELA (Adriani et al. 2009) and 10^6 for AMS-02 at 400 GeV/c (Aguilar et al. 2013). Both PAMELA and AMS-02 have a permanent magnet on board to distinguish the charge of the particles. The FERMI-LAT does not have a magnet for charge separation; for this reason, it used the shadow imposed by the Earth and its offset direction for electrons and positrons due to the geomagnetic field to measure, separately, the spectra of CR electrons and positrons from 20 GeV to 200 GeV. In Figure 3.2 the positron fraction for the experiments from 1990 up to 2014 is reported. At energy below ∼10 GeV, the discrepancies of the different set of data are due to the solar modulation. As explained in Bobik et al. (2012), the different behaviour for the two species of charged particles, occurring in periods with different magnetic field polarity (A), may be due to the particle drift effects in the heliosphere. During periods with $A > 0$ (e.g., AMS-01 mission) the positrons ratio is higher than the one measured during a period with opposite field polarity $A < 0$ (e.g., PAMELA mission).

In the last few years, PAMELA and AMS-02 explored also the high energy part (lower than 1 TeV) of the separated electron and positron spectra. Figures 3.3, 3.4 and 3.5 show the recent results with respect to the previous experiments. Pamela

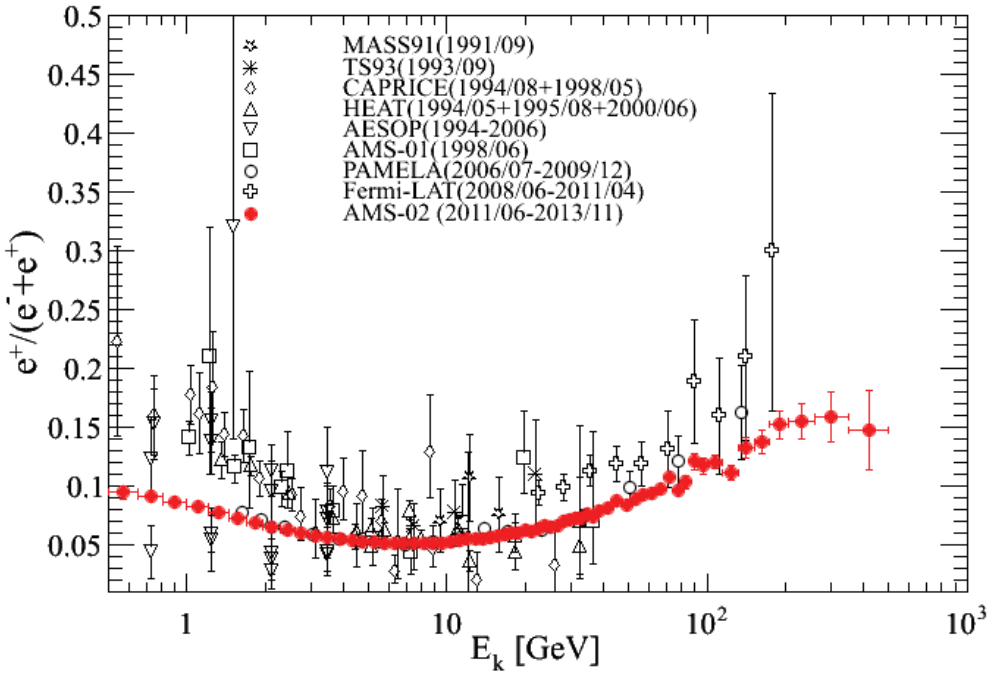

Figure 3.2: Positron fraction recorded by the experiments from 1990 up to 2014. The dates between brackets are related to the data taking periods of the experiments.

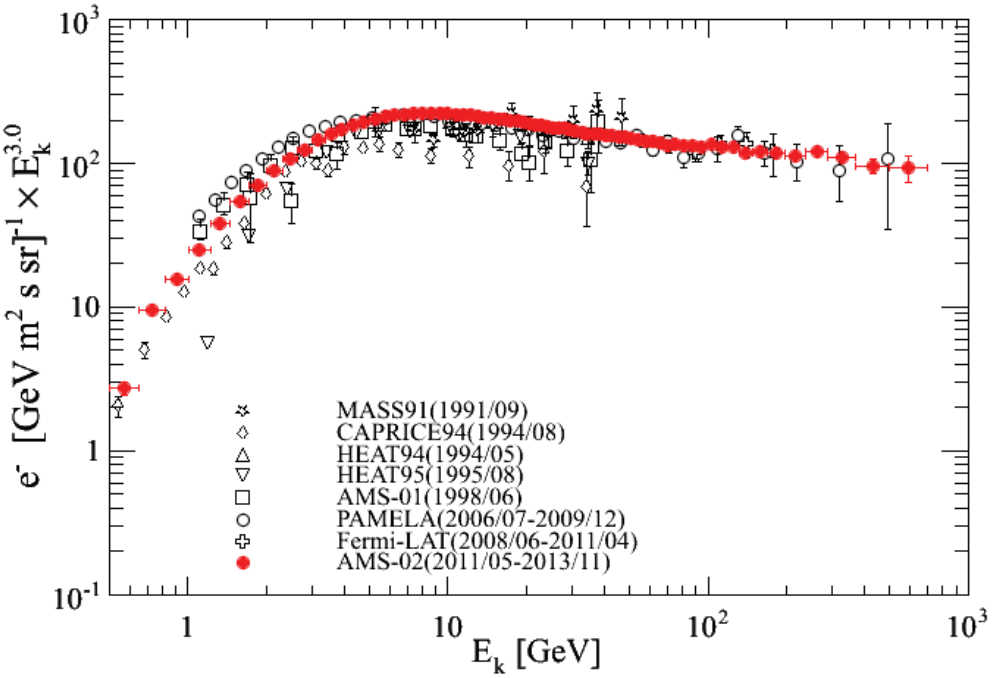

Figure 3.3: Electron flux recorded by the experiments from 1990 up to 2014.

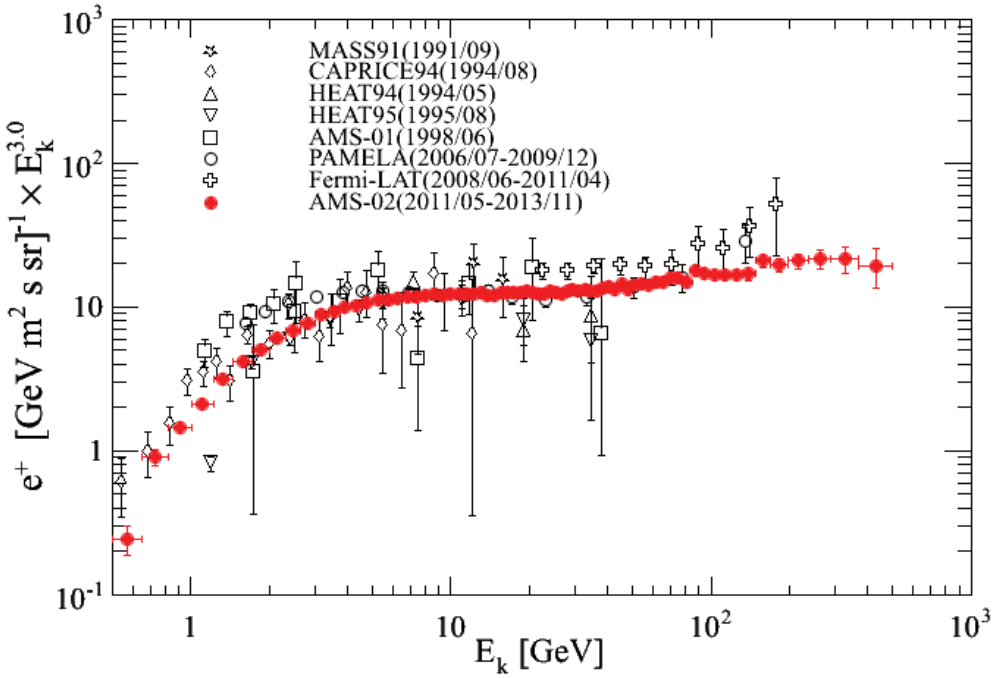

Figure 3.4: Positron flux recorded by the experiments from 1990 up to 2014.

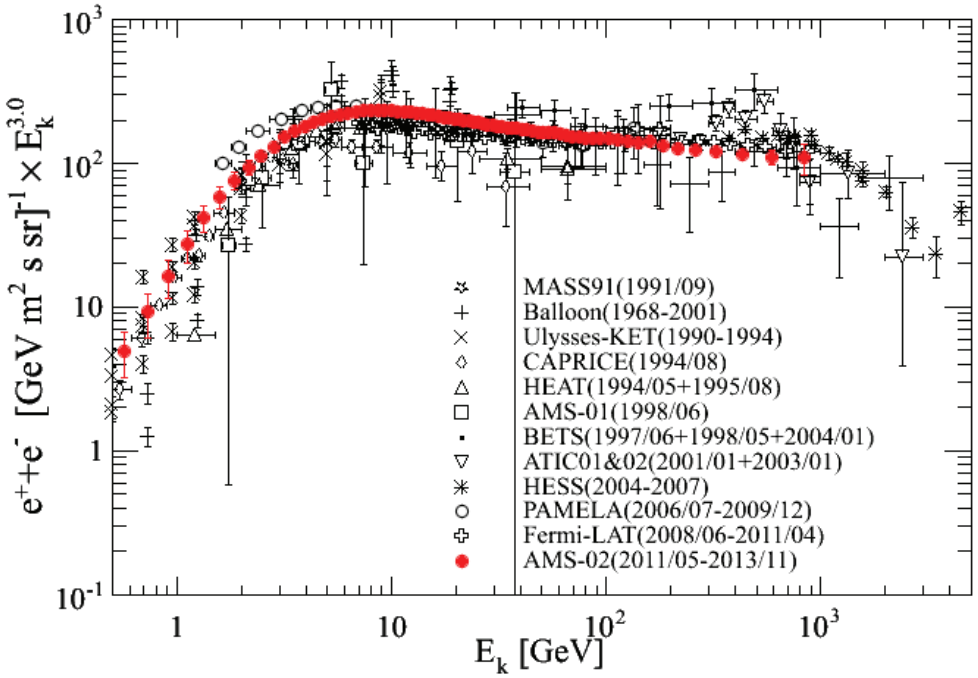

Figure 3.5: Electron plus positron flux recorded by the experiments from 1990 up to 2014.

observed electrons during a total acquisition time of approximately 1200 days in the energy interval 1-625 GeV. The total systematic uncertainty on the flux was found to increase from about 4% at 1 GV/c to about 7% at 600 GV/c. The single power-law fit represents well the data ($\chi^2/ndf = 8.7/13$) with a resulting spectral index of -3.18 ± 0.05 (Adriani et al. 2011). The total systematic uncertainty on the positron flux, instead, was found to vary from $\sim 6\%$ at 2 GV to $\sim 20\%$ above 100 GV (Adriani et al. 2013). AMS-02 experiment measured electrons from 0.5 to 700 GeV and positrons from 0.5 to 500 GeV. Above 10 GeV, above the effects of solar modulation, the spectral indices for positrons and electrons are significantly different. Single power-law fits over different energy ranges show that γ_{e^+} hardens from -2.97 ± 0.03 (fit over 15.1-31.8 GeV) to -2.75 ± 0.05 (fit over 49.3-198 GeV). Correspondingly, γ_{e^-} hardens from -3.28 ± 0.03 (fit over 19.0-31.8 GeV) to -3.15 ± 0.04 (fit over 83.4-290 GeV) and then levels off (Aguilar et al. 2014a). The AMS-02 collaboration published also the electron plus positron flux Aguilar et al. (2014b). A total of 10.6×10^6 $(e^+ + e^-)$ events have been identified with energies from 0.5 GeV to 1 TeV from May 19, 2011, to November 26, 2013. From 30.2 GeV to 1 TeV, the flux can be described by a single power law with $\gamma = -3.170 \pm 0.008$(stat+syst)$\pm$0.008(energy scale uncertainty). In these work we will use the most recently AMS-02 data to try to understand possible astrophysical sources that contribute to these fluxes.

3.2 Cosmic ray propagation

The propagation of cosmic rays in the Galaxy can be simplified by equation (1.12) as in (see e.g., Ginzburg & Syrovatskii 1964, Chap. 3 and Ginzburg & Ptuskin 1976):

$$\frac{\partial n_i}{\partial t} = Q_i + \vec{\nabla} \cdot \left[D_i \, \vec{\nabla} n_i \right] + \frac{\partial}{\partial E} \left[b_i \, n_i \right] - p_i n_i + P_i, \tag{3.1}$$

where the time evolution of the energy density $n_i = dN_i/dE$ of cosmic ray species i with energy E depends on the source term Q_i, diffusion coefficient D_i, the change of the particle energy per unit time b_i, catastrophic processes p_i (e.g., Bremsstrahlung process for electrons or transformations of nuclei) and nuclei collisions P_i. Equation (3.1) accounts for i) the propagation of primary components like, e.g., electrons, protons and carbon nuclei mainly accelerated in SNRs (e.g., Ginzburg & Syrovatskii 1964, Chap. 4) and ii) the production of secondary spectra like, e.g., positrons and boron nuclei produced from interaction of primary CRs with the ISM. In this chapter, different from the previous one, we refer to secondary CR as particles produced in the ISM instead to ones produced in the atmosphere (as used in the previous

chapter).

Our galaxy, the Milky-Way, is a disc containing material in form of condensed objects ($\sim 10^{10} - 10^{12}$ stars) and diffuse matter (the interstellar medium) with an average density of about 1 atom/cm^3. It consists of about 90% hydrogen and the remaining $\sim 10\%$ of helium. The evidence for CRs, pervading the entire galactic space, stems from the observation of the diffuse galactic radio noise which comes from all the galaxy and from the halo surrounding the disc. This radiation is commonly accepted as due to synchrotron radiation emitted by cosmic ray electrons and positrons spiralling along the weak interstellar magnetic field lines. Figure 3.6 shows the map of the sky observed at a frequency of 408 MHz. At the center of the figure 3.6, the

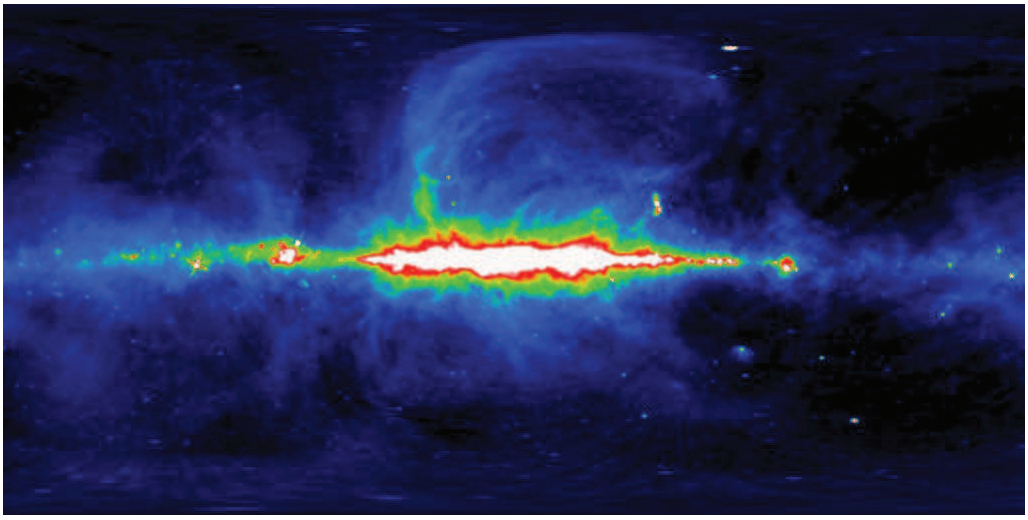

Figure 3.6: Sky map Haslam 408 MHz in galactic coordinates (Haslam et al. 1982).

high concentration of photons is due to synchrotron emission and bremsstrahlung. The latter depends on the presence of interstellar gas that is concentrated in a thickness of about ± 100 pc above and below the galactic plane. Outside this region, the emission of photons is the only synchrotron component observed in the radio band of the electromagnetic radiation. Finally, if electrons pervade the galaxy, there is no reason to doubt that energetic nuclei exist also therein. Estimation of energetics and number densities of potential CR sources such as supernovae in the Galaxy are adequate to explain the CR intensities near Earth. These observations suggest a simple model in which CR are generated in galactic objects and injected into interstellar space.

The motion of a CR in the Galaxy is influenced by the nature of the magnetic fields therein. The interstellar magnetic field is divided into two components: the first one is the regular component direct along the spiral arms of the galaxy, while the sec-

ond one consists in an irregular and random component (see e.g., Schlickeiser 2002, Chap. 2). In this way, cosmic rays propagate along a random path and the process is described by a diffusive model. From cosmic rays and radio-astronomical data, the value of the diffusion coefficient is typically assumed $\sim 10^{28} - 10^{29}\,\mathrm{cm^2 s^{-1}}$. The spatial and momentum diffusion derives from the cosmic ray scattering on MHD wave and discontinuities. Locally, this diffusion is anisotropic and occurs along the magnetic field, while the isotropization is accounted by the strong large scale ($\sim 100\,\mathrm{pc}$) fluctuations of the galactic magnetic field (e.g., Ptuskin et al. 2006; Strong et al. 2007). The scattered mean free path (λ) depends on Larmor radius (r_L), on the ratio of energy densities in ordered (B_0) and turbulent (δB) magnetic field and on the maximum Alfven wavelength (L, determined by the physics of turbulent input at large eddies) (e.g., Schlickeiser 2002; Ptuskin et al. 2006):

$$\lambda \simeq r_L^{\delta} \left(\frac{B_0}{\delta B}\right)^2 L^{1-\delta}, \tag{3.2}$$

where $\delta \sim 0.3$. If $B_0 = 3\,\mu\mathrm{G}$, $\delta B = 0.9\,\mu\mathrm{G}$, $L = 10^{21}$ cm and $\delta = 0.34$, we can evaluate a mean free path $\lambda \sim 10^{19} E_{GeV}^{\delta}$ cm. The diffusion coefficient depends on the mean free path as follows:

$$D = \frac{1}{3}\beta c\lambda \simeq 10^{29} E_{GeV}^{\delta} \mathrm{cm^2 s^{-1}}. \tag{3.3}$$

From equation (3.3), we can derive the spatial diffusion coefficient described by e.g., Strong et al. (2007):

$$D(E) = D_0 \left(\frac{E}{E_0}\right)^{\delta}. \tag{3.4}$$

In addition to spatial diffusion, the scattering of CRs on randomly moving MHD waves leads to a stochastic acceleration which is described in the transport equation (3.1) as diffusion in momentum space. Distributed acceleration may be responsible for the peaks in the ratios of secondary to primary nuclei at about 1 GeV. Above this energy, the acceleration mechanism seems absent. Another CR transport could be the convection, a wind that drives the particles in the Galaxy. In section 3.3 and 3.4, we will propose some examples concerning the influence of some galactic parameters, like the heigh of the Galaxy and the diffusion parameters, on the CR fluxes. One of the most important aspect that affects the CR propagation are the gas, the radiation and magnetic fields. From these phenomena it is possible to study the secondary production and the energy losses of the particles.

Some ratios between different fluxes of CRs are very important to determine the

parameters of the transport equation. Ratios between primaries species (e.g., carbon over oxygen, C/O) are practically insensitive to the change of the diffusion parameter values because they have the same origin and undergo the same physical processes. Moreover, these ratios are very useful to determine the parameters related to the sources (e.g., Maurin et al. 2001). Ratios between secondary and primary species, like boron over carbon B/C or $(^{10}\mathrm{B}+^{11}\mathrm{B})/(^{12}\mathrm{C}+^{13}\mathrm{C}+^{14}\mathrm{C})$ (boron is only secondary), are influenced by parameters related to convection and re-acceleration. As reported by Strong et al. (2007), there are five secondary unstable nuclei used to estimate the parameters of propagation: ^{14}C, ^{10}Be, ^{26}Al, ^{36}Cl and ^{54}Mn. By studying the relationship of these fluxes with respect to the spectra of primary nuclei, such as $^{10}\mathrm{Be}/^{9}\mathrm{Be}$, it is possible to determine the height of the galactic halo ($z_h = 4-6$ kpc). Since the secondary radioactive nuclei can travel only a few hundred parsecs, the relationship with the stable primary nuclei, which come from throughout the region, allows to determine the diffusion coefficient and the size of the region. Three isotopes: ^{59}Ni (7.6×10^4 yr), ^{57}Co (0.74 yr) and ^{56}Ni (6 d) decay only by electron capture (K-capture) (Strong et al. 2007). If the secondary acceleration of these particles occurs before the decay, the latter is suppressed. By the way, with all the data available now, it is not possible to ensure that CR propagation models are or not in agreement with the re-acceleration or other phenomena.

3.3 GALPROP

CR propagation models are based on simplifying assumptions which allows to obtain solutions, usually numerically, easily comparable with the experimental data. The analytical solutions are very useful in simple cases to see the trends of the spectra reproduced as a function of the quantity used, but they become very complicated, while numerical analysis can return the distribution of cosmic rays in each point in space and for each kind of particle. Furthermore, the analytical models are valid only under certain restrictions, such as neglecting the energy losses or the variations of the density, which numerical models do not. Hereafter, we will use the GALPROP model to evaluate the local interstellar spectra.

The GALPROP code[2] numerically solves equation (3.1) for different CR species in a cylindrically symmetric space (Vladimirov et al. 2011) and returns the local interstellar spectrum for the specific particle at the Solar System. The solution of equation (3.1) depends on parameters like the boundary conditions of the galactic effective volume for CR diffusion (radius $R_{Gal.}$ and height $h_{Gal.}$), the diffusion co-

[2]http://galprop.stanford.edu/webrun.php (2014)

efficient as a function of the energy (approximated by $D(E) = D_0(E/E_b)^{\delta}$, Strong et al. 2007; Ptuskin et al. 2006) and the injection spectra characterized by power laws with different spectral indices for nuclei, protons (γ_p) and primary electrons (γ_e). To determine these parameters, we compared the so obtained LIS's with the experimental data above ∼10 GeV (where the solar modulation effects are negligible); then we tuned the coefficients minimizing the discrepancies. The calculated LIS's were normalized at 50 GeV with measured proton and electron fluxes at Earth. For proton and electron spectra, we used the AMS-02 data (Haino, S. & the AMS-02 Collaboration 2013; Aguilar et al. 2014a), while for the ratios: B/C, Be/B, Be/C, Li/B, Li/Be and Li/C, we referred to the online cosmic ray database reported in Maurin et al. (2013). The available data are best described using the parameters in table 3.1. These parameters are "standard" parameters used also in other works

Parameter	Value
$R_{Gal.}$	30 kpc
$h_{Gal.}$	±4 kpc
D_0	$5.8 \cdot 10^{28}$ cm^2 s^{-1}
δ	0.33
E_0	4 GeV
v_A	30 km s^{-1}
γ_p	1.98 ($E < 9$ GeV), 2.42 ($E > 9$ GeV)
γ_e	1.7 ($E < 4$ GeV), 2.68 ($E > 4$ GeV)

Table 3.1: Propagation parameters used in GALPROP code to determine the LIS's.

(see e.g., Delahaye, T. et al. 2010). In section 3.2, we discuss the importance of the ratios between secondary and primary CR fluxes. Figures 3.8, 3.7 and 3.9 report the GALPROP LIS for different kind of these ratios. The black solid line in each graph comes from the GALPROP simulation. The discrepancies below ∼ 10 GeV are due to the solar effects, in fact, the GALPROP LIS's are not modulated. Figure 3.7 reports the ratio between two primary CR species. Both carbon and oxygen are supposed to be produced and accelerated by the same sources and this hypothesis is confirmed by the flatness of the ratio in the full energy range. Measurements of the abundance of secondary cosmic-ray nuclei, produced in spallation processes (like boron), relative to the abundance of their parent primary cosmic-ray species (like carbon) can be used to investigate the energy dependence of the galactic propagation path-length and finally the diffusion coefficient (see figure 3.8). At the end, figure 3.9 reports other ratios between secondary (Li, Be and B) and primary (C) CRs.

The electron GALPROP LIS consists of particles produced in SNR and in the

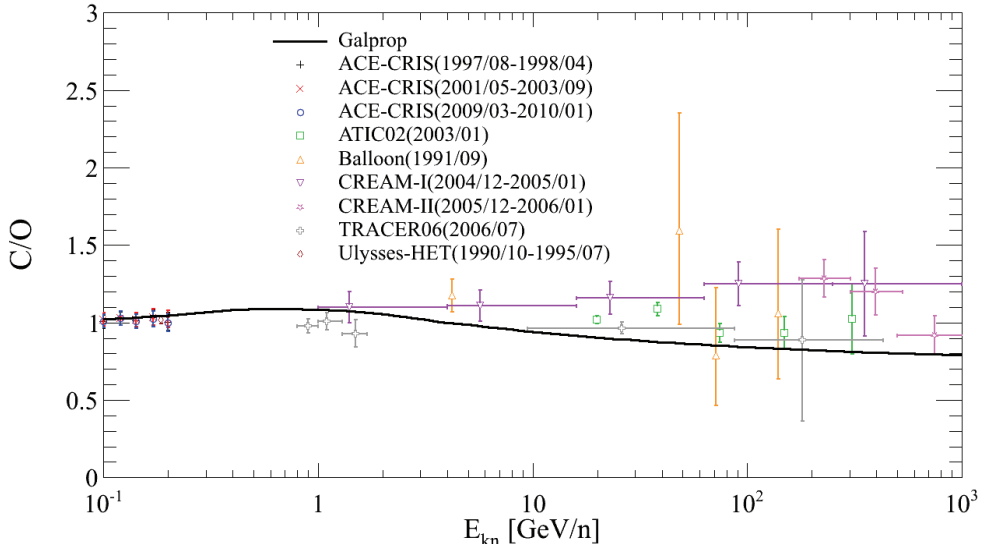

Figure 3.7: Carbon over oxygen ratio observed by experiments, collected in the online cosmic ray database reported in Maurin et al. (2013), from 1990 up to now; the ratio between LIS's from GALPROP, using the parameters reported in table 3.1, is also reported.

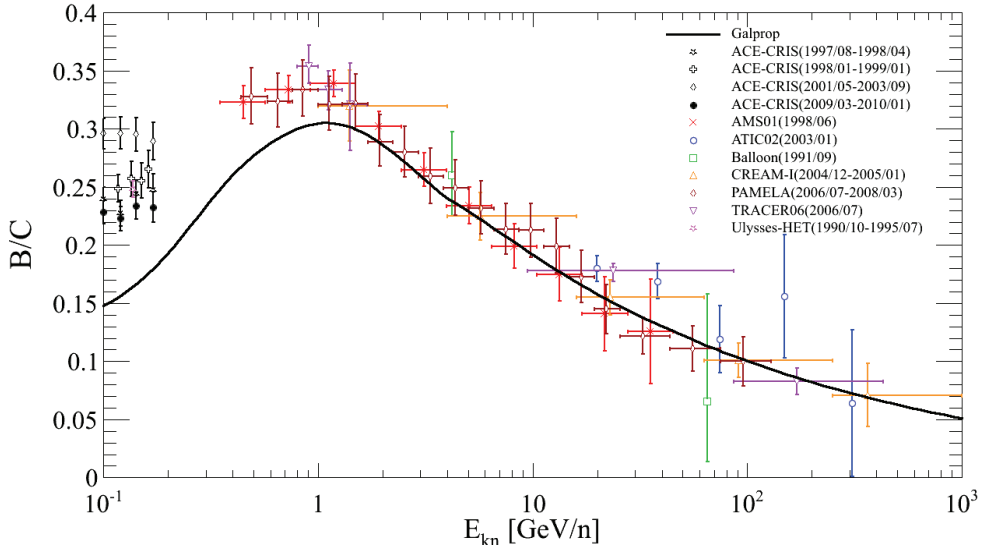

Figure 3.8: Boron over carbon ratio observed by experiments, collected in the online cosmic ray database reported in Maurin et al. (2013), from 1990 up to now; the ratio between LIS's from GALPROP, using the parameters reported in Table 3.1, is also reported.

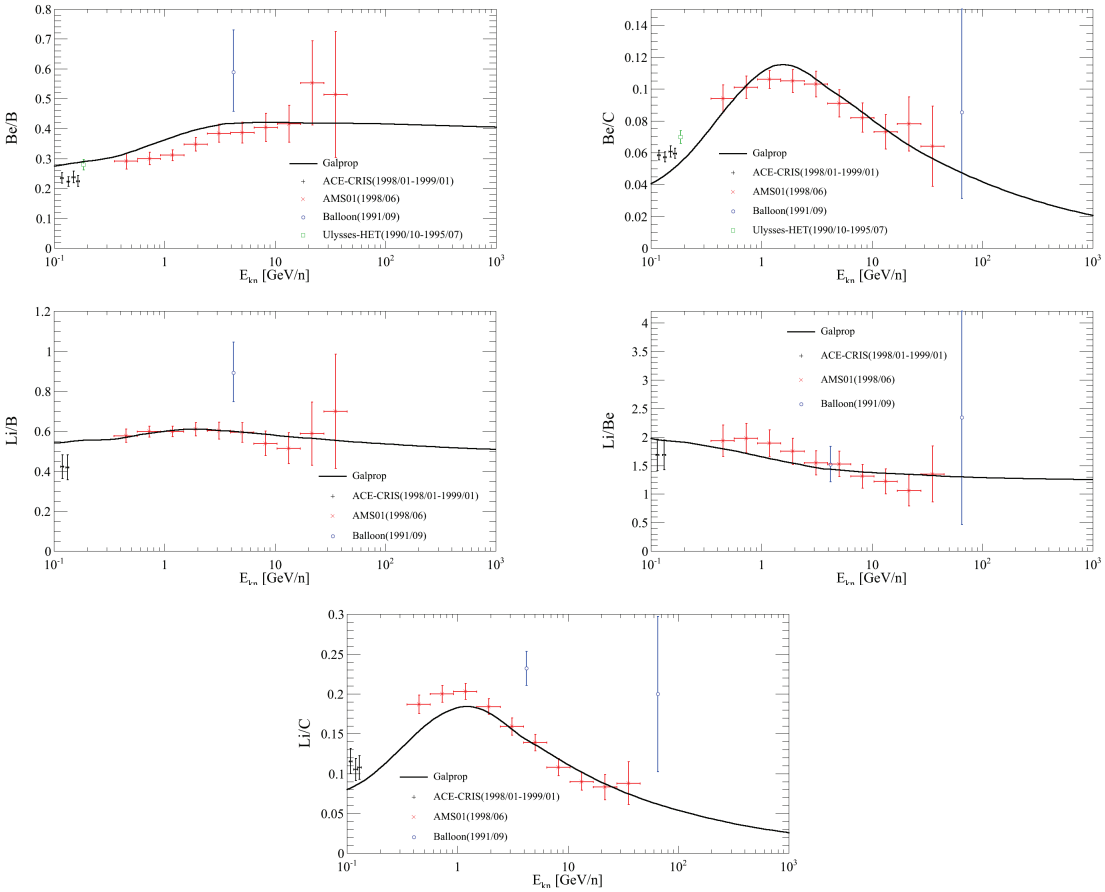

Figure 3.9: Other ion ratios observed by experiments, collected in the online cosmic ray database reported in Maurin et al. (2013), from 1990 up to now; the ratios between LIS's from GALPROP, using the parameters reported in Table 3.1, are also reported.

ISM (electron "classical" LIS, hereafter electron cLIS), while the positron one regards only particles produced in the ISM (positron "classical" LIS, hereafter positron cLIS). In figure 3.10 we reported the comparison between cLIS's and AMS-02 data for electrons and positrons. The cLIS's are represented in the energy range under analysis (the region affected by solar modulation, below 10 GeV, is out of our interest). As already mentioned, the GALPROP positron cLIS is underestimated for

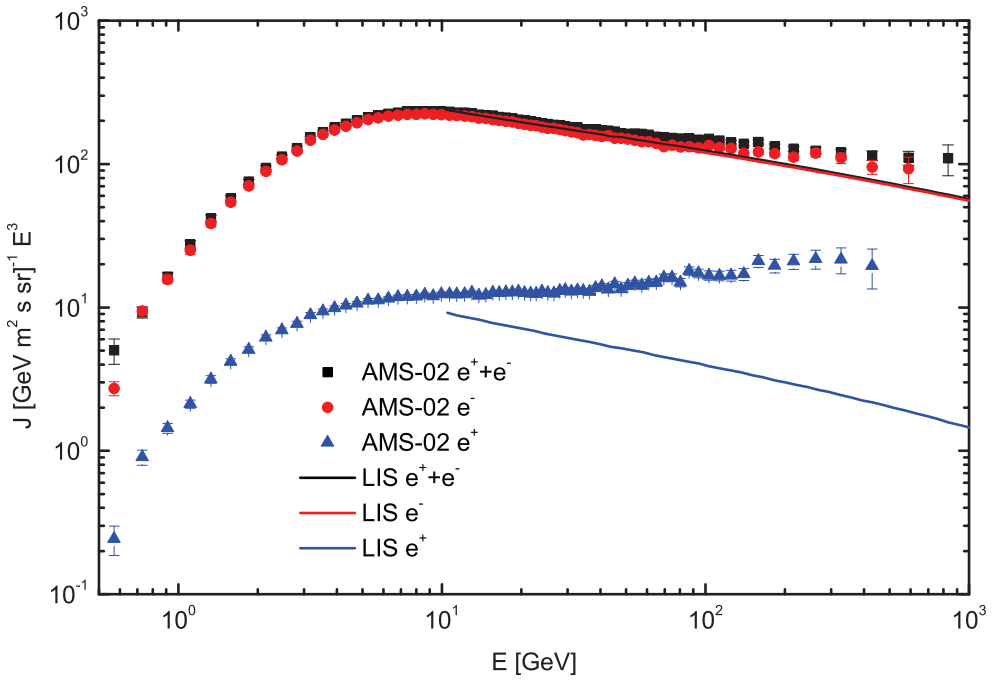

Figure 3.10: Electron and positron omnidirectional intiensities observed by AMS-02 (Aguilar et al. 2014a) and their cLIS's from GALPROP (obtained with the parameters reported in Table 3.1).

energy above 10 GeV, while the electron one is underestimated above $\sim$ 90 GeV. We want to focus the attention on the high energy part of these fluxes and ratios because we will present later a possible interpretation to the positron and electron fluxes. Above $\sim$10 GeV, it is possible to elude the solar modulation effects (Strauss & Potgieter 2014), convection and reacceleration mechanism (Delahaye, T. et al. 2010). In addition to energy losses (discussed in section 3.6 for electrons and positrons) and the injection spectral indices, three parameters are responsible for the CR propagation in the Galaxy: D_0 and δ defining the diffusion coefficient and the half thickness of the diffusion zone $h_{Gal.}$ (see equation 3.4). These parameters are self-consistently constrained with ratios of secondary to primary nuclei (as pointed out in this chapter and in Maurin et al. 2001). The parameters have been changed, as reported in section 3.4, to find different configurations to explain data. The uncertainty in those

parameters leads to systematic errors in positrons and electrons cLIS's.

3.4 Electron and positron spectra excess

The omnidirectional intensity excess for electrons and positrons are shown in figure 3.11. The difference between the observed AMS-02 spectra and GALPROP

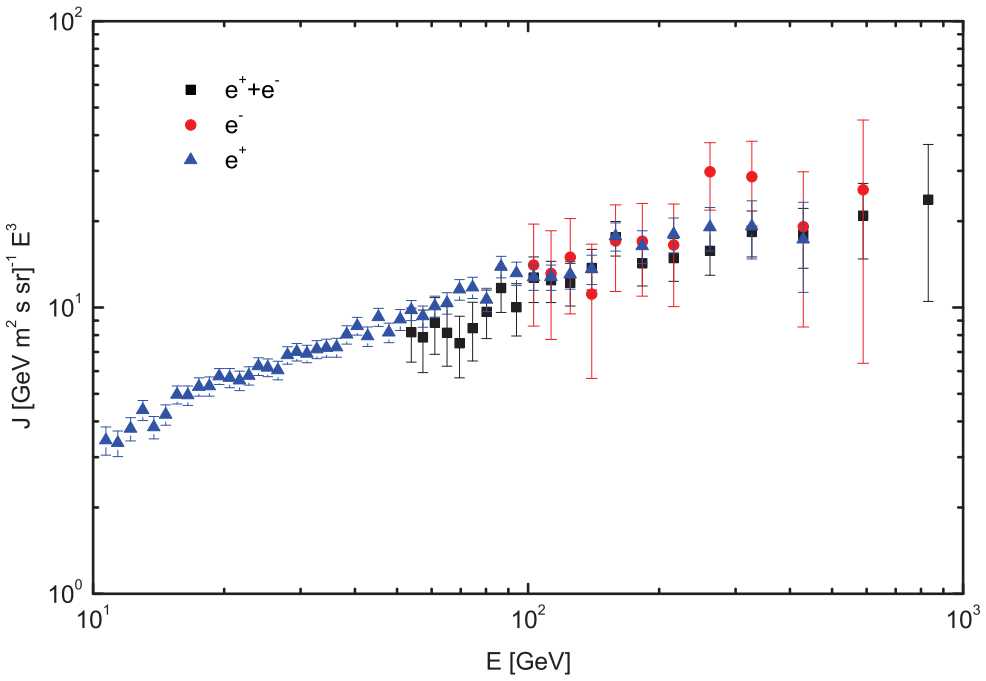

Figure 3.11: Omnidirectional intensity excess for electrons, positrons and half of all electron, obtained as a difference between the AMS-02 flux and the corresponding "classical" LIS.

cLIS's were calculated for energy above $\sim$ 10 GeV (where the solar modulation effects are negligible) and requiring at least a difference (above 10%) between the two fluxes. Under these constraints, the electron and positron signals are reported for energy above 90 GeV and above 10 GeV, respectively. We report also the electron plus positron spectrum, above 50 GeV, divided by a factor two for a comparison with respect to the other data. The error bars of these data come from the experimental observations. We can remark how these excess spectra of positrons and electrons can be fitted using similar power laws. The electron signal spectral index, resulting from the fit, is $-(2.503 \pm 0.353)$, for positrons we have $-(2.502 \pm 0.030)$, while for electron plus positron spectrum we have $-(2.568 \pm 0.088)$. The points of Fig. 3.11 are dependent on the parameters used in GALPROP. To explore this issue, we altered one by one the main GALPROP parameters responsible for the diffused

spectra (the galactic height and the diffusion coefficient). The ranges inside which we varied the values are reported in table 3.2 (see Delahaye, T. et al. 2010 for a better explanation related to the variability of the diffusive parameters). The systematic

Parameters	Range
Galactic height (kpc)	$2 < h_{Gal.} < 6$
Diffusion Coefficient Constant (cm^2s^{-1})	$4 \cdot 10^{28} < D_0 < 10^{29}$
Diffusion Coefficient Index	$0.3 < \delta < 0.4$

Table 3.2: Ranges of propagation parameters used in GALPROP code to determine the errors in the LIS evaluation.

uncertainties due to the choice of the GALPROP parameters result in a systematic change of the omnidirectional intensities in figure 3.11. In figure 3.12, we report the positron excess obtained subtracting the positron cLIS to the AMS-02 data as in figure 3.11 for energy above 20 GeV. The blue band keeps into account the variation of the GALPROP parameters reported in table 3.2 as systematic uncertainty. The

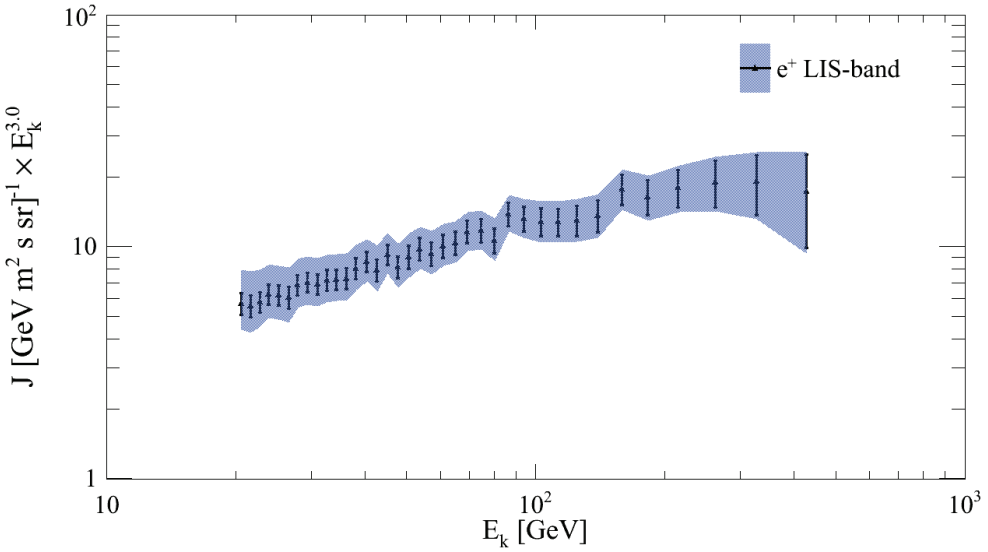

Figure 3.12: Excess omnidirectional intensities for positrons (full triangle), obtained as a difference between the AMS-02 flux and the corresponding LIS. The band is due to the GALPROP parameters changed as in table 3.2.

variation can be accounted as a scale factor of $\sim 5\%$ at 100 GeV and above, while at lower energy it is $\leq 20\%$. This scale factor is mostly constrained by the fit on the positron spectrum. The higher absolute values of the electron bins lead to higher fluctuations under the GALPROP parameters change; for this reason we report only the positron analysis.

3.5 Electrons and positrons propagation in the Galaxy

The electrons in cosmic rays can be measured either directly, studying the flux, or indirectly, through the analysis of the electromagnetic radiation emitted in the galaxy (see e.g., figure 3.6). This latter method involves the observation of the electromagnetic radiation spectrum in the radio region, X- and gamma-rays. The radio band consists mainly of synchrotron radiation emitted by electrons that interact with the magnetic field of the galaxy. An analysis carried out by Platania et al. (1998) shows a spectral index $\alpha \sim 0.8$ for frequencies $0.4 < \nu_{\mathrm{GHz}} < 7.5$. With the following formula:

$$E(\mathrm{GeV}) \simeq 7.9\sqrt{\frac{\nu_{\mathrm{GHz}}}{B(\mu\mathrm{Gauss})}}, \tag{3.5}$$

we can obtain the energy of the particle that produced the radiation ($2.9 < E(\mathrm{GeV}) < 12.5$), while the spectral index of the electrons, in the same energy range, turns out to be $\gamma = 2\alpha + 1 \sim 2.6$. A charged particle travelling from its source to the solar neighbourhood is affected by several processes. Particles interacting with magnetic fields describe random walks in real space (diffusion) and momentum space (diffusive reacceleration). Galactic wind introduces a spatial convection with a consequently adiabatic losses process. Particles lose energy via interactions with cosmic matter, magnetic and radiation fields. In our case, we are focusing on particles with energy $E > 10$ GeV. Above this limit, the propagation of electrons and positrons in the galaxy is dominated by space diffusion and energy losses (Delahaye, T. et al. 2010; Lin et al. 2010). The transport equation (3.1) can be simplified in equation (3.6). The energy loss rate term keeps into account the ionization process (that depends on the logarithm of the energy) and bremsstrahlung (linear in energy) with the atoms of the ISM, synchrotron and inverse Compton effect with the magnetic and radiation fields respectively (both depending on the square of the energy). Following the approach reported in e.g., Ginzburg & Syrovatskii (1964); Malyshev et al. (2009), the time evolution of the energy density $n_e(\vec{x}, E, t)$ of electrons or positrons from a single source distant $\vec{x}$ from the Solar System, with energy E and after a diffusion time t, is:

$$\frac{\partial n_e(\vec{x}, E, t)}{\partial t} = Q(\vec{x}, E) + \vec{\nabla} \cdot \left[D(E) \vec{\nabla} n_e(\vec{x}, E, t) \right] + \frac{\partial}{\partial E} \left[b(E) n_e(\vec{x}, E, t) \right], \tag{3.6}$$

where $Q(\vec{x}, E)$ is the source term, $D(E)$ the diffusion coefficient depending on energy. In equation (3.6), the term $b(E)$ accounts the rate of energy lost resulting for

energy losses due to ionization, Bremsstrahlung, synchrotron and inverse Compton processes (see e.g., Schlickeiser 2002, Chap. 4). However, above ~ 1 GeV, the relevant mechanisms are synchrotron and inverse Compton (see section 3.6 for a better explanation). Furthermore, above few GeV, using an average interstellar magnetic field of 3 μG and the photon radiation fields reported in Delahaye, T. et al. (2010) (Table 2, model M1), the fit of the total energy loss rate can be described by a power law as in:

$$\frac{dE}{dt} = -b(E) \sim -b_0 E^2, \tag{3.7}$$

where $b_0 \sim 7 \cdot 10^{-17}$ GeV^{-1}s^{-1} (value in agreement with those reported in e.g., Kobayashi et al. 2004; Atoyan et al. 1995). Due to the high rate of energy loss, a positron or an electron of 100 GeV dissipates most of its energy in about 10^6 years and can diffusively travel up to a typical distance of about 2 kpc. Sources of the high-energy positron and electron excesses, observed by PAMELA (see Adriani et al. 2009) and AMS-02 (see Aguilar et al. 2013), are located in a region relatively close, ~ 2 kpc, to the Earth. The general solution of equation (3.6) requires to introduce the Green function $G(\vec{x_1}, E, t, \vec{x_0}, E_0, t_0)$ which satisfies:

$$\frac{\partial G}{\partial t} - \frac{\partial}{\partial E}\left[b(E)G\right] - D(E)\frac{\partial^2 G}{\partial x^2} = \delta(\vec{x_1} - \vec{x_0})\delta(E - E_0)\delta(t - t_0), \tag{3.8}$$

and its solution is:

$$G(\vec{x_1}, E, t; \vec{x_0}, E_0, t_0) = \frac{1}{b(E)} \frac{1}{(4\pi\lambda_d^2)^{3/2}} e^{-\frac{|\vec{x_1} - \vec{x_0}|^2}{4\sigma_d^2}} \delta(t - t_0 - t')\theta(E_0 - E), \tag{3.9}$$

where λ_d is the mean distance travelled by particles with initial energy $E_0 = E/(1 - b_0 t E)$ down to energy E resulting from both energy loss and diffusion processes given by

$$\lambda_d(E, E_0) = \left(\int_E^{E_0} \frac{D(E')dE'}{b(E')}\right)^{1/2}, \tag{3.10}$$

while

$$t'(E, E_0) = \int_E^{E_0} \frac{dE'}{b(E')}. \tag{3.11}$$

These equations have few limits. Both the ISM magnetic and radiation fields vary in space, consequently the diffusion coefficient and the energy loss function depend on the coordinates: $D = D(E, x)$ and $b = b(E, x)$, but in this case there is not a simple analytic solution to equation (3.6). In this work we do not enter into this topic, a simple calculation was made in appendix B of Malyshev et al. (2009). For an injection spectrum described by a power law with index (α) and an exponential

energy cut-off (E_{cut}), e.g.,

$$Q(E) = Q_0 E^{-\alpha} \exp\left(-\frac{E}{E_{cut}}\right), \tag{3.12}$$

Malyshev et al. (2009), following Ginzburg & Syrovatskii (1964, chap. 5), determined the interstellar diffused spectra of electrons and positrons from equation (3.6), as:

$$\begin{aligned} J(\vec{x}, E, t) &= \frac{\beta c}{4\pi} n_e(\vec{x}, E, t) \\ &= \frac{\beta c}{4\pi} \frac{Q_0}{(4\pi\lambda_d^2)^{3/2}} E^{-\alpha} (1 - b_0 t E)^{\alpha-2} \\ &\quad \times \exp\left[-\frac{E}{E_{cut}(1 - b_0 t E)}\right] \exp\left(-\frac{|\vec{x}|^2}{4\lambda_d^2}\right). \end{aligned} \tag{3.13}$$

The example made with the injection spectrum of equation (3.12) is justified in chapter 4 where it is used as source spectrum from pulsars and their nebulae.

The cosmic ray electron and positron spectra, reported in equation (3.13) from a single source, depend significantly on the distance of the source (see figure 3.13) and from the time spent by particles to diffuse in the ISM (see figure 3.14). The spectra were evaluated using spectral index ($\alpha = 2.2$), energy cut-off ($E_{cut} = 10$ TeV), energy loss coefficient ($b_0 = 7 \cdot 10^{-17}$ GeV^{-1}s^{-1}) and normalization factor ($Q_0 = 8.23 \cdot 10^{48}$ GeV$^{\alpha-1}$). Figure 3.13 reports the diffuse spectrum as a function of the energy. The

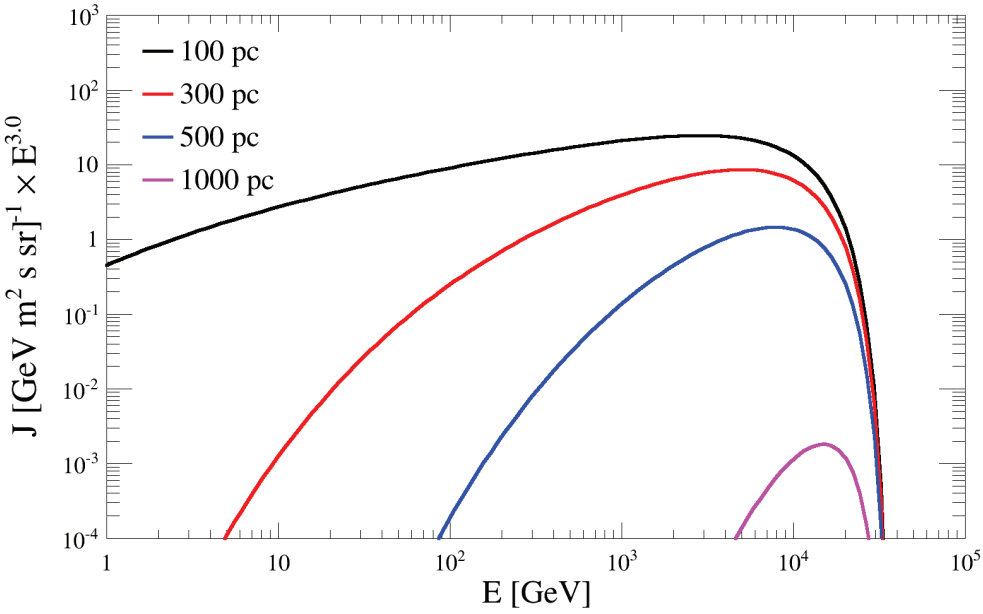

Figure 3.13: Propagated spectra from a source at different distances and a diffusion time of 10000 years.

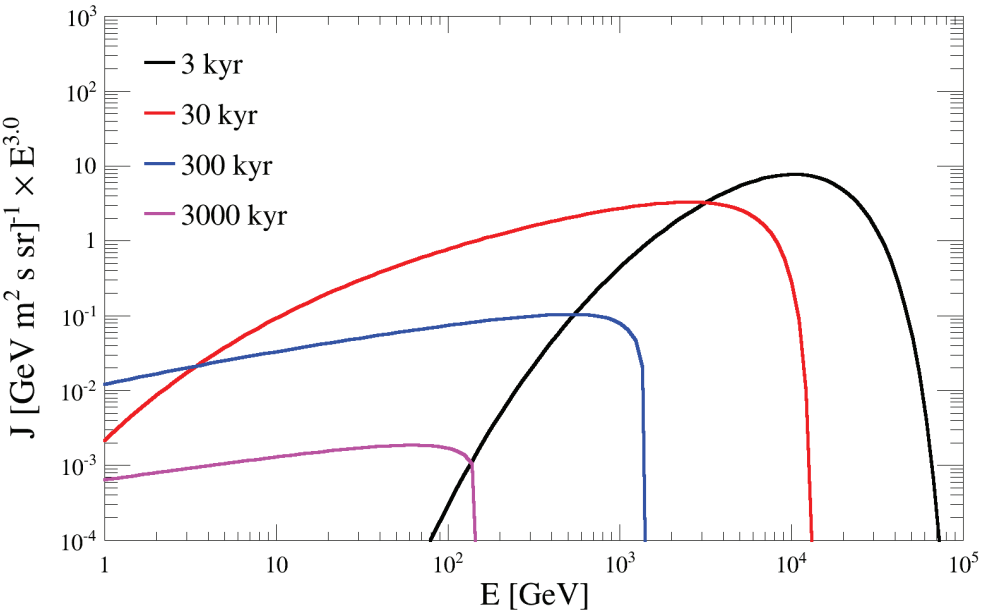

Figure 3.14: Propagated spectra from a source distant 290 pc at different diffusion time.

different color represent the different travelled distance. Contribution of far sources (e.g., $d = 1$ kpc) are mainly at high energy due to the faster particles, while for close ones (e.g., $d = 100$ pc) the contribution of the low energy particles increases. A similar effect is reported in figure 3.14 where the different spectra depend on the diffusion time (related to the distance travelled). Injecting particles at a fixed distance, the high energy part of the spectrum arrives first (peak at 3 kyr) and then continues to diffuse to higher distance (the energy cut-off decreases increasing the time).

The cut-offs of the spectra are due to the energy loss, very important for these kinds of particles. Using different coefficient for b_0, we report the results in figure 3.15. This graph evidences that an higher energy loss rate leads to a low energy cut-off of the spectra, vice-versa, when particles lose less energy the cut-off is higher.

In presence of no energy loss now we consider a pure diffusive process, the mean distance travelled by particles is:

$$R_d = \sqrt{4D(E)t} \tag{3.14}$$

and the energy density n_e is:

$$n_e(\vec{x}, E, t) = \frac{Q_0 E^{-\alpha} \exp\left(-\frac{E}{E_{cut}}\right)}{(\pi R_d^2)^{3/2}} \exp\left(-\frac{|\vec{x}|^2}{R_d^2}\right). \tag{3.15}$$

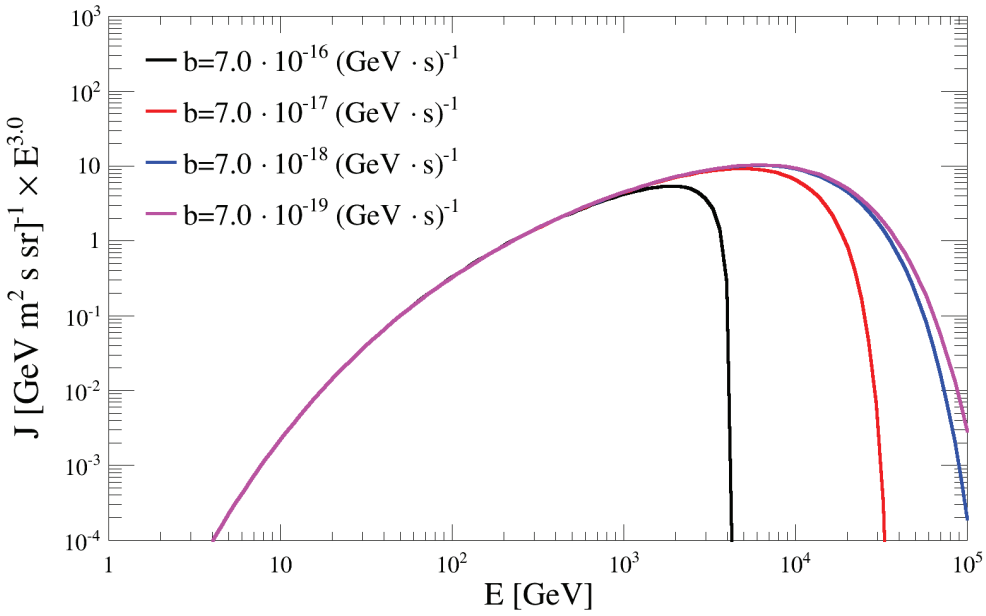

Figure 3.15: Propagated spectra from a source distant 290 pc with a diffusion time of 10000 years and different energy loss coefficient.

The strong dependence of a cut-off in the diffuse spectra from the energy loss term leads to consider these processes in a more exhaustive way (see discussion in section 3.6).

3.6 Energy loss rate of CRe$^{\pm}$ in ISM

Electrons and positrons rapidly lose their energy through four fundamental processes: ionization, bremsstrahlung, synchrotron and inverse Compton effect.

Ionization process

Charged particles passing through a medium lose their kinetic energy via electromagnetic interactions, excitation or ionization processes (see e.g., Leroy & Rancoita 2009, Chap. 2.1.6). The last process involves the production of fast electrons (δ-rays) that can ionize again (secondary ionization). The electron energy lost in the material depends on the differential cross section for the process ($e^-e^- \rightarrow e^-e^-$). At low energies, the process is described by the Mott scattering, while, at high energies, the relativistic extension is described by Møller one (see e.g., Mandl & Shaw 2010, Chap. 8) which provides a maximum energy transfer equal to half of the initial one. For positrons, in the process ($e^+e^- \rightarrow e^+e^-$) described by the Bhabha scattering, the maximum energy transferred is the full energy of the incoming particle. The

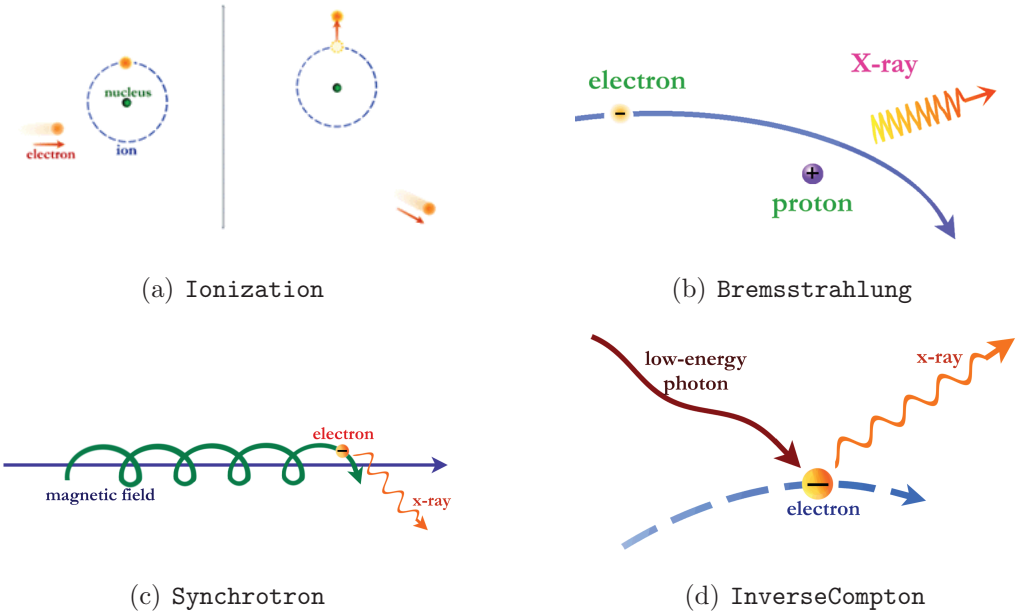

(a) `Ionization` (b) `Bremsstrahlung`

(c) `Synchrotron` (d) `InverseCompton`

Figure 3.16: Electron (positron) energy loss schemes.
Source: `http://www.astro.wisc.edu/~bank/` (2014).

rate of energy lost by electrons and positrons in ordinary matter for ionization is exhaustively described in Seltzer & Berger (1984). The complete formula is:

$$-\left.\frac{dE}{dt}\right|_{Ion} = \frac{3}{4}\sigma_T c m_e c^2 \frac{\rho N_A Z}{A\beta^2} B(\gamma) \tag{3.16}$$

$$B(\gamma) = B_0(\gamma) - 2\ln\left(\frac{I}{mc^2}\right) - \delta, \tag{3.17}$$

where:

$\sigma_T = \frac{e^4}{6\pi\epsilon_0^2 m_e^2 c^4}$	Thomson cross section;
m_e	elettron mass;
e	electron charge;
c	speed of light in vacuum;
$n_A = \frac{\rho N_A}{A}$	target density (atoms/cm^3);
Z, A	atomic and mass number;
ρ	medium density;
$n_e = n_A Z$	electron density of the medium;
β	ratio between particle velocity and the speed of light;
γ	$E/m_e c^2$;
I	mean eccitation energy;
δ	density effect correction factor.

For electrons, $B_0(\gamma)$ is equal to:

$$B_0(\gamma) = \ln\left[\frac{\left(\gamma^2-1\right)^2}{2\left(\gamma+1\right)}\right] + \frac{1}{\gamma^2} + \frac{1}{8}\left(1-\frac{1}{\gamma}\right)^2 - \frac{1}{\gamma}\left(2-\frac{1}{\gamma}\right)\ln 2, \tag{3.18}$$

while for positrons:

$$B_0(\gamma) = \ln\left[\frac{\left(\gamma^2-1\right)^2}{2\left(\gamma+1\right)}\right] + 2\ln 2 - \frac{\beta^2}{12}\left[23 + \frac{14}{\gamma+1} + \frac{10}{\left(\gamma+1\right)^2} + \frac{4}{\left(\gamma+1\right)^3}\right]. \tag{3.19}$$

The density effect correction could be expressed in three different regimes and the formula (3.17) becomes:

$$B(\gamma) = \begin{cases} B_0(\gamma) + b_0 - b_4\left(\frac{p}{mc}\right)^2 & \text{if } E \le E_0 \\ B_0(\gamma) + 1 - 2\ln\left(\frac{p}{mc}\right) + b_1 - b_2\left[1 - \frac{2\ln\left(\frac{p}{mc}\right)}{b_3}\right]^k & \text{if } E_0 < E < E_1 \\ B_0(\gamma) + 1 - 2\ln\left(\frac{p}{mc}\right) + b_1 & \text{if } E \ge E_1 \end{cases} \tag{3.20}$$

Remember that:

$$E^2 = p^2c^2 + m^2c^4 = \gamma^2 m^2 c^4 \;\Rightarrow\; \frac{p}{mc} = \sqrt{\gamma^2-1} \tag{3.21}$$

The parameters in equation (3.20) were calculated by Seltzer & Berger (1984):

$b_0 = -2\ln\left(\frac{I}{mc^2}\right)$

$b_1 = -2\ln\left(\frac{\hbar\omega_{pl}}{mc^2}\right)$

$b_2 = \left[\delta_0 + 1 + 2\ln\left(\frac{I}{\hbar\omega_{pl}}\right) - 2\ln\left(\frac{p_0}{mc}\right)\right]\left[\frac{\ln\left(\frac{p_1}{mc}\right)}{\ln\left(\frac{p_1}{p_0}\right)}\right]^k$

$b_3 = 2\ln\left(\frac{p_1}{mc}\right)$

$b_4 = \frac{\delta_0}{\left(\frac{p_0}{mc}\right)^2}$

where $b_4 = 0$ for conductive mediums. ω_{pl} is the plasma frequency:

$$\omega_{pl} = \sqrt{\frac{e^2 n_e}{\epsilon_0 m_e}}. \tag{3.22}$$

The parameters Z, Z/A, I, ρ, $\hbar\,\omega_{pl}$, E_0, E_1, b_0, b_1, b_2, b_3, b_4, k are tabulated in Seltzer & Berger (1984).

In our case, we assumed a mean hydrogen density in the galaxy as $n_H \sim 10^6$ m^{-3}. Our Solar System is in a special region of the galaxy called Local Bubble (Welsh & Shelton 2009) of $\sim$ 100 pc big with a lower hydrogen density of $n_H \sim 5 \cdot 10^3$ m^{-3}, with a consequently lower energy loss rate. Moreover, the helium abundance

is about 10% of the hydrogen one.

Bremsstrahlung emission

The bremsstrahlung occurs in presence of a nuclear field with the consequent emission of electromagnetic radiation (see e.g., Leroy & Rancoita 2009, Chap. 2.1.7). In classical mechanics we have two regimes of validity which depend on the impact parameter b. If $b > r_{atom}$ the nuclear charge is completely screened by the atomic electrons with the result that the nuclear field loses its effect on the incoming particle; if $b < r_{atom}$ it does not have any masking effect and the nuclear field is the Coulomb field of a point charge Ze. In quantum mechanics, the impact parameter depends on the Heisenberg Uncertainty Principle. Bethe & Heitler (1934) derived in quantum mechanics, the formula of the energy loss rate for electrons in a field of a heavy nucleus, point like and without spin under the Bohr approximation ($2\pi\alpha Z \ll 1$) where $\alpha = e^2/(4\pi\epsilon_0\hbar c)$ is the fine structure constant. If we neglect the screen we have:

$$mc^2 \ll E_0 \ll 137\frac{mc^2}{Z^{1/3}} \tag{3.23}$$

and the energy loss rate becomes:

$$-\left.\frac{dE}{dt}\right|_B = \frac{3}{8\pi}\sigma_T c\alpha n_A EZ(Z+1)\left[4\ln\left(\frac{2E}{mc^2}\right) - \frac{4}{3}\right]. \tag{3.24}$$

If we have the screen:

$$E_0 \gg 137\frac{mc^2}{Z^{1/3}} \tag{3.25}$$

the energy loss rate is:

$$-\left.\frac{dE}{dt}\right|_B = \frac{3}{8\pi}\sigma_T c\alpha n_A EZ(Z+i)\left[4\ln\left(\frac{183}{Z^{1/3}}\right) + \frac{2}{9}\right], \tag{3.26}$$

where i comes from the screen of the nuclear charge by atomic electrons:

$$i = \frac{\ln\left(\frac{530}{Z^{2/3}}\right)}{\ln\left(\frac{183}{Z^{1/3}}\right) + \frac{1}{18}}. \tag{3.27}$$

Equations (3.24) and (3.26) must be corrected for electron energy less than 2 MeV (Elwert correction), energy up to 50 MeV (Koch-Motz correction) and energy above 50 MeV (Olsen correction) (see e.g., Leroy & Rancoita 2009, Chap. 2.1.7). These corrections are kept into account adding a term $(-f(Z))$ inside square brackets in

equations (3.24) and (3.26):

$$f(Z) = 1.2021\left(\alpha Z^2\right) \quad \text{low Z} \qquad f(Z) = 0.925\left(\alpha Z^2\right) \quad \text{high Z} \tag{3.28}$$

Electrons and positrons behave in a different way because electrons are attracted from the nucleus and rejected by the atomic electrons, vice-versa positrons are attracted by the atomic electrons and rejected by the nuclear charge. This difference occurs only at energies below some MeV. The ratio $\Re = (dE/dt|_{e^+})/(dE/dt|_{e^-})$ given by the energy loss rate for bremsstrahlung of positrons with respect to electrons is:

$$0 < \Re < 1 \quad \text{for} \quad 10^{-7}\, MeV < \frac{E}{Z^2} < 10^{-1}\, MeV. \tag{3.29}$$

For electrons (positrons) with energy above few MeV it is assumed a complete screen (see e.g., Gould 1975; Blumenthal & Gould 1970; Berger & Seltzer 1964).

Synchrotron radiation

At high energy ($E > 1$ GeV), electrons and positrons fast lose their energy via two fundamental processes: synchrotron emission and inverse Compton effect. The first one occurs when an electron or positron spirals in a magnetic field emitting electromagnetic radiation tangents to the trajectory. The name comes from the first observation of this phenomenon that was observed in particle accelerator called synchrotron. Given a particle that describes a helical motion around the magnetic field lines and assuming a uniform field (adiabatic hypothesis) the energy loss rate is proportional to the square of the energy of the particle according to the law (see e.g., Blumenthal & Gould 1970):

$$-\left.\frac{dE}{dt}\right|_S = \frac{4\sigma_T c}{3\left(m_e c^2\right)^2} U_{mag} E^2, \tag{3.30}$$

where:

$$U_{mag} = \frac{B^2}{2\mu_0} \tag{3.31}$$

is the energy density of the magnetic field (B). The interstellar magnetic field value is about $B \sim 3 \times 10^{-10}$ T with a consequently energy density of $\sim 2 \times 10^5$ eV/m^3.

Inverse Compton effect

The Compton effect is one of the process that highlights the corpuscular nature of the electromagnetic radiation and it is related to the interaction between a quantum

of radiation (photon) and a free electron. If the electron, before being hit by the photon, has an energy low enough to be considered at rest, then, it can subtract energy to incident photon (classical Compton effect). If the electron has an initial energy not negligible, the photon can subtract energy from the electron (inverse Compton effect). Applying the conservation of energy and momentum, it is possible to calculate the energy change of the photon after the collision. The interesting result shows that, in some cases, the photon gains energy from electron. This process is cancelled if the electron is not relativistic or photon has a low frequency. The inverse Compton effect (IC) can be also seen as a loss of energy by the electron that depends on the energy density of the photons, i.e.:

$$U_{ph} = \int_0^{+\infty} \epsilon \cdot n(\epsilon) d\epsilon, \tag{3.32}$$

where $n(\epsilon)d\epsilon$ is the photon distribution ($\epsilon = h\nu$ is the photon energy) that, for a black body (BB), is:

$$n(\epsilon)d\epsilon = \frac{8\pi\epsilon^2}{h^3c^3} \frac{d\epsilon}{e^{\frac{\epsilon}{k_bT}} - 1}. \tag{3.33}$$

Evaluating the integral in equation (3.32) with equation (3.33) we obtain (see appendix A):

$$U_{ph} = \frac{8\pi}{h^3c^3} \int_0^{+\infty} \frac{\epsilon^3 d\epsilon}{e^{\frac{\epsilon}{k_bT}} - 1} = \frac{8\pi}{h^3c^3} (k_bT)^4 \int_0^{+\infty} \frac{x^3 dx}{e^x - 1} = \frac{4\pi}{c} \frac{\sigma}{\pi} T^4, \tag{3.34}$$

where:

$$\sigma = \frac{2\pi^5 k_b^4}{15c^2h^3} \tag{3.35}$$

is the Stefan-Boltzmann constant. The mean value of the photon energy for a BB is:

$$\begin{aligned} \langle \epsilon \rangle &= \frac{\int_0^{+\infty} \epsilon n(\epsilon) d\epsilon}{\int_0^{+\infty} n(\epsilon) d\epsilon} = k_bT \frac{\pi^4}{15 \cdot 2 \cdot \zeta(3)}, \\ \langle \epsilon^2 \rangle &= \frac{\int_0^{+\infty} \epsilon^2 n(\epsilon) d\epsilon}{\int_0^{+\infty} n(\epsilon) d\epsilon} = (k_bT)^2 \frac{24 \cdot \zeta(5)}{2 \cdot \zeta(3)}, \end{aligned} \tag{3.36}$$

where ζ is the Riemann Zeta function (see appendix A).

The energy loss rate for IC depends on the initial electron and photon energy. In the not relativistic limit, $\Gamma_e = \frac{4\epsilon\gamma}{mc^2} \ll 1$, it is possible to use the Thomson approximation in which the Compton cross section is used because the scattered photon energy is higher than the one before the interaction (Blumenthal & Gould

1970):

$$-\left.\frac{dE}{dt}\right|_{IC\,T} = \frac{4}{3}\sigma_T c U_{ph}\left[\left(\frac{E}{mc^2}\right)^2 - 1\right]. \tag{3.37}$$

Using the Klein-Nishina cross section, equation (3.37) is corrected as:

$$-\left.\frac{dE}{dt}\right|_{IC\,T*} = \frac{4}{3}\sigma_T c U_{ph}\left[\left(\frac{E}{mc^2}\right)^2 - 1\right]\left[1 - \frac{63}{10}\frac{E\left\langle\epsilon^2\right\rangle}{\left(mc^2\right)^2\left\langle\epsilon\right\rangle}\right] \tag{3.38}$$

If both electron and photon energy are high, $\Gamma_e \gg 1$, the energy loss rate is:

$$\begin{aligned}
-\left.\frac{dE}{dt}\right|_{IC\,KN} &= \frac{3}{8}\sigma_T c\left(mc^2\right)^2\int_0^{+\infty}\frac{n(\epsilon)}{\epsilon}\left[\ln\left(\frac{4\epsilon E}{\left(mc^2\right)^2}\right) - \frac{11}{6}\right]d\epsilon \\
&= \frac{3\pi}{h^3c^3}\sigma_T c\left(mc^2\right)^2\left(k_bT\right)^2\int_0^{+\infty}\frac{x}{e^x-1}\left[\ln\left(\frac{4k_bTE}{\left(mc^2\right)^2}\right) + \ln x - \frac{11}{6}\right]dx \\
&= \frac{\pi^3}{2h^3c^3}\sigma_T c\left(mc^2\right)^2\left(k_bT\right)^2\left[\ln\left(\frac{4k_bTE}{\left(mc^2\right)^2}\right) - \frac{5}{6} - C_E + C_l\right],
\end{aligned} \tag{3.39}$$

with:

$$\begin{aligned}
\int_0^{+\infty}\frac{x}{e^x-1}dx &= \frac{\pi^2}{6} \\
\int_0^{+\infty}\frac{x\ln x}{e^x-1}dx &= -\frac{\pi^2}{6}\left(-1 + C_E\right) + \zeta'(2)
\end{aligned} \tag{3.40}$$

$$C_E = 0.577216 \qquad\qquad C_l = \frac{6}{\pi^2}\zeta'(2) = -0.569961 \tag{3.41}$$

where C_E is the Euler constant. Delahaye, T. et al. (2010) reports a parametrization to connect the Thomson to the Klein-Nishina limits. Assuming $\alpha_{IC} = \frac{\gamma k_b T}{m_e c^2}$, the energy loss rate due to IC with BB photons is:

$$-\left.\frac{dE}{dt}\right|_{IC} = \begin{cases}
\frac{4}{3}\sigma_T c U_{ph}\left[\left(\frac{E}{mc^2}\right)^2 - 1\right] & \alpha < 3.8\cdot 10^{-4} \\
10^{-45}\frac{E^2(k_bT)^4}{\alpha}e^{\sum_{i=0}c_i(\ln\alpha)^i} & 3.8\cdot 10^{-4} < \alpha < 1.8\cdot 10^3 \\
\frac{\sigma_T}{16}\frac{(m_e c k_b T)^2}{\hbar^3}\left[\ln(4\alpha) - 1.9805\right] & \alpha > 1.8\cdot 10^3
\end{cases} \tag{3.42}$$

where: $c_i = \{74.77,\ -0.1953,\ -0.0997,\ 0.004352,\ 0.0003546,\ -0.0000301\}$. A black body is an ideal body that absorbs and radiates in the spectrum according to the Planck's law (3.33). The bodies in nature are gray bodies, their distributions differ from the BB one by a factor, emissivity, which is defined as the ratio of the energy

radiated from the surface of the body (U_{ph}) with respect to the one emitted by a black body at the same temperature (U_{ph}^{BB}). In this case, you can always normalize the equation (3.42) by a factor U_{ph}/U_{ph}^{BB} to obtain the correct rate of energy lost (see e.g., Delahaye, T. et al. 2010).

The radiation field in the interstellar medium is composed by four contributions: the cosmic microwave background (CMB), the infrared component (IR), the visible light due to stars (Star) and ultraviolet (UV) light. The following table 3.3 shows the temperature values T_0, U_{ph} and U_{ph}^{BB} densities, the normalization factor K_{norm} to be introduced as a factor in equation (3.42) and the mean value of the photon energy $\langle\epsilon\rangle$. Figure 3.17 reports the contributions of the energy loss rate due to the

Radiation	T_0 [K]	U_{ph} [eV/m^3]	U_{ph}^{BB} [eV/m^3]	K_{norm}	$\langle\epsilon\rangle$ [eV]
CMB	2.726	259952	259952	1	$6.34 \cdot 10^{-4}$
IR	33.07	254000	$5.639 \cdot 10^{9}$	$4.50 \cdot 10^{-5}$	$7.70 \cdot 10^{-3}$
Star	313.32	54700	$4.543 \cdot 10^{13}$	$1.20 \cdot 10^{-9}$	$7.29 \cdot 10^{-2}$
UV	3249.3	370000	$5.255 \cdot 10^{17}$	$7.04 \cdot 10^{-13}$	0.7564
	6150.4	229000	$6.746 \cdot 10^{18}$	$3.39 \cdot 10^{-14}$	1.432
	23209.0	118900	$1.368 \cdot 10^{21}$	$8.69 \cdot 10^{-17}$	5.403

Table 3.3: Temperature, energy density and mean value of the interstellar radiation field.

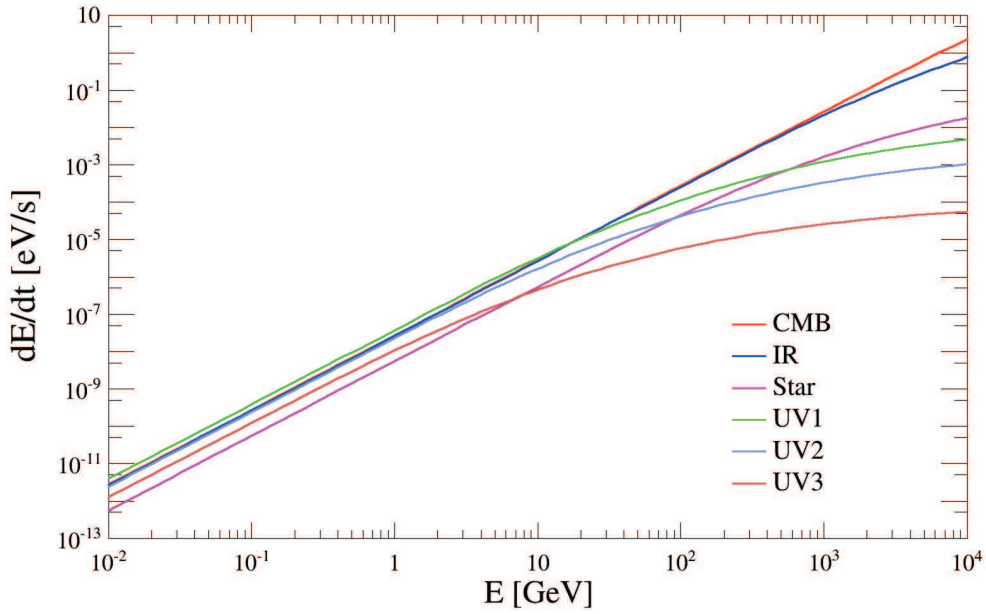

Figure 3.17: Energy loss rate due to inverse Compton effect in ISM with different radiation fields.

six inverse Compton kinds of interactions in the galaxy. We note that, for energies

above 10 GeV, the dominant contribution is due to the cosmic background radiation that permeates the universe.

The sum of the contributions due to all the energy loss rates is shown in figure

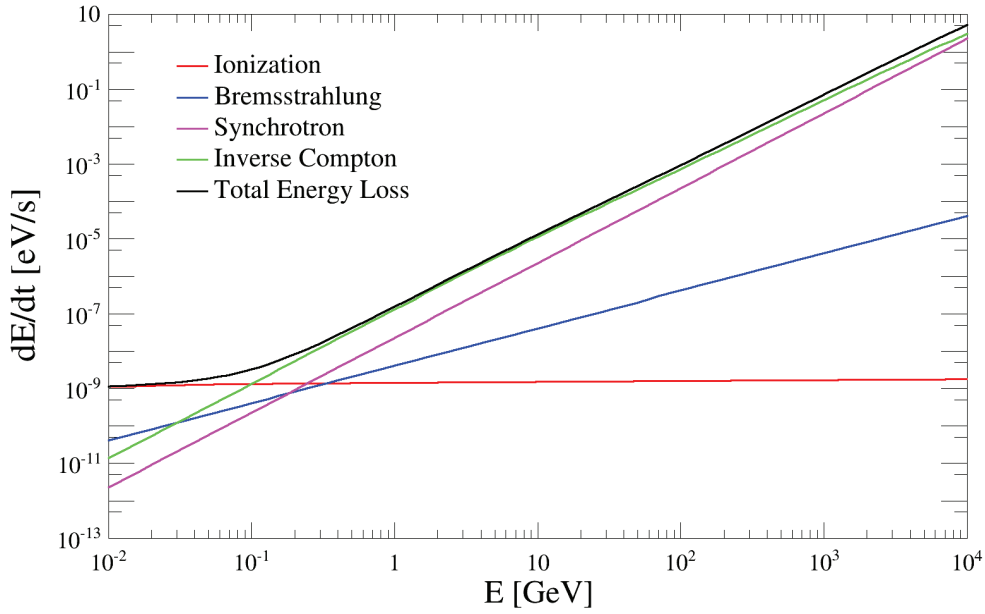

Figure 3.18: Energy loss rate due to ionization, Bremsstrahlung, synchrotron, inverse Compton effect and the total contribution.

3.18. For $E > 1$ GeV, the dominant contribution depends on the square of the initial energy due to synchrotron and inverse Compton effects. Using the total contribute of figure 3.18, it is possible to calculate the time and the maximum distance that these particles can reach before losing all their energy,

$$\tau_{max} = \frac{E}{\frac{dE}{dt}} \underbrace{\sim}_{E>1\text{ GeV}} \frac{E}{bE^2}, \tag{3.43}$$

where b is the contribution due to the synchrotron and inverse Compton energy loss. Using equation (3.10), or for simplicity (3.14), the maximum average diffusive path depends on this time τ_{max} and diffusion coefficient[3] ($D_0 \simeq 5.8 \cdot 10^{28}$ cm^{2}s^{-1}). An electron with an initial energy of 100 GeV can travel for ~ 2 kpc. For this reason, in the next chapter, we will discuss possible sources of electrons and positrons distant less than 2 kpc.

[3]For the choice of the parameter of the diffusion coefficient see section 3.3

Chapter 4

Primary astrophysical sources of electrons and positrons

As presented in section 3.4, we are searching for a candidate responsible for the electron-positron pairs production; i.e., we are looking for an interpretation of the electron and positron excesses shown in figure 3.11. Without considering more exotic explanations, e.g., in the framework of dark matter scenarios (Yuan et al. 2013; Feng et al. 2014; Ibe et al. 2013), we focus the attention on astrophysical sources. In this chapter, we will investigate on the possible final states of a star, its neutron star (NS). After a brief presentation of these objects, we explore the physics of pulsars (PSR), rotating magnetized neutron stars, that lose their energy through electromagnetic radiation of the magnetic dipole whose spinning around a tilted axis (see section 4.1). Within a simplified model, it is possible to determine the main physical PSR parameters (like magnetic field or energy loss) starting from the rotational frequency (ν) of the pulsar, its first ($\dot{\nu}$) and second ($\ddot{\nu}$) derivative (section 4.1.1, 4.1.2 and 4.1.3). In section 4.1.4, we present the photon data, detected by the FERMI experiment. Among these sources, we selected those characterised by an higher photon emission around the object, the so called pulsar wind nebula (PWN, see section 4.2). Interpreting the gamma-ray spectrum of these PWN's as due to synchrotron and inverse Compton emissions of electrons and positrons produced by the pulsars, we evaluate the particle spectrum as a function of the time (section 4.2.1). The Vela-X object is the best candidate (relatively close and young source) to interpreter the AMS-02 electron and positron excess (section 4.2.2). A so important source, responsible for the main contribution in the CR electron and positron spectra, could give us information related to an anisotropic signal in the arrival directions of the particles. Analytic results, of anisotropy from Vela-X, are reported in section 4.3.

4.1 Pulsars

It is commonly accepted that when a massive star collapse, a large amount of material is released creating a supernova remnant, while the remaining mass collapses into a neutron star (Baade & Zwicky 1934). Pulsars were first discovered observationally in 1967 by Jocelyn Bell Burnell and Antony Hewish (Hewish et al. 1968). Pacini (1967) predicted the phenomena associated to the intense magnetic fields of a neutron star rapidly rotating. Shortly following the 1967, Gold (1968) and Pacini (1968) argued the connection between pulsars and rotating NS. The discovery of many more pulsars came quickly. In 1968, the Vela pulsar (Large et al. 1968) and the Crab pulsar (Staelin & Reifenstein 1968) were discovered. The first pulsar observed in optical frequencies was the Crab (Cocke et al. 1969). In the same year, the first X-ray pulsations were discovered, from the same source, from an X-ray detector on a rocket. Today over 2300 pulsars are known (see e.g., the ATNF catalogue[1] and Manchester et al. 2005). They are characterised by a compact core of neutrons that was left at the centre of the supernova explosion when the outer layers of the star were blown off. Pulsars are quickly rotating, extremely dense (about $6.65 \cdot 10^{17}$ kg/m^3) and small objects with a strong magnetic field (typically 10^{14} G). The strong magnetic field and the fast rotation (the average rotation period is of the order of 1 s but approaches 1 ms in the most rapidly rotating cases) come from the conservation of the magnetic field and angular momentum during their formation.

In a contracting fluid, magnetic field lines will remain frozen in and, in the same way, when the supernova progenitor collapses, the total magnetic flux must be conserved. The flux of $\vec{B}$ through a surface S is given by the integral:

$$\Phi_B = \int_S B dA. \tag{4.1}$$

The conservation of the magnetic flux leads to the following equality:

$$\int_{S_{star}} B_{star} dA_{star} = \int_{S_{NS}} B_{NS} dA_{NS}. \tag{4.2}$$

The integrals over the areas are the spherical surface of the objects and they will depend on the radius of the star (R_{star}) or neutron star (R_{NS}):

$$B_{NS} = B_{star} \frac{R_{star}^2}{R_{NS}^2}. \tag{4.3}$$

[1] `http://www.atnf.csiro.au/people/pulsar/psrcat/` (2014)

Pulsars have a typical radius of $\sim$ 10 km that is relatively small compared to 10^6 km for a typical star. From equation (4.3), typical pulsars have magnetic fields of the order of 10^{14} G compared to $\sim 10^3$ G in a main sequence star. Similarly, the angular momentum is conserved in the collapsing star:

$$\Omega_{star} \cdot I_{star} = \Omega_{NS} \cdot I_{NS}, \tag{4.4}$$

during which the angular velocity ($\Omega = 2\pi/P$, P is the rotational period) increases. Using $I = (2/5)mR^2$, the inertial momentum of a sphere with mass m and radius R, the conservation leads to:

$$P_{NS} = P_{star} \frac{R_{NS}^2}{R_{star}^2}. \tag{4.5}$$

Typically the rotation period of a pulsar is around 1 s compared to 25 days for a main sequence star such as the Sun.

4.1.1 The oblique rotator

The simplest model describes a pulsar as a rotating magnetic dipole whose axis is tilted with respect to the rotational axis by an angle ϑ (see Figure 4.1). The energy

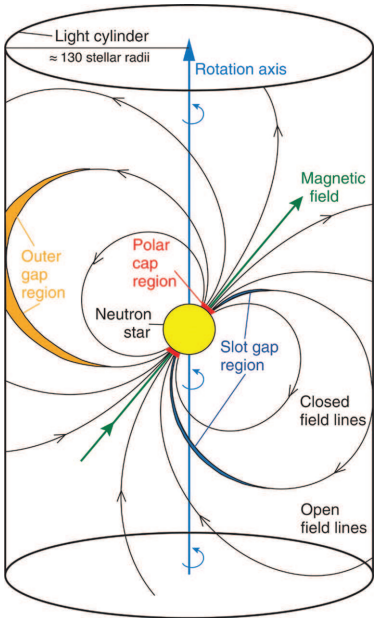

Figure 4.1: A sketch of the pulsar's magnetosphere. Credit: Magic Collaboration `http://www.sciencemag.org/content/322/5905/1221.figures-only` (2014).

output from the pulsar is assumed to come from the rotational kinetic energy (E_{rot})

stored in the neutron star which is released as pulsar spin down:

$$E_{rot} = \frac{1}{2} I \Omega^2, \tag{4.6}$$

where we can assume a moment of inertia $I \sim 10^{45}$ g/cm^2. The rate of energy loss is:

$$\frac{dE_{rot}}{dt} = I\Omega\dot{\Omega} = -4\pi^2 I \frac{\dot{P}}{P^3}. \tag{4.7}$$

It is commonly believed that the spin down luminosity comes from the rotational energy via magnetic radiation. If the magnetic field is assumed as a dipole (magnetic moment: $M = B_p R_{NS}^3/2$), the magnetic radiation power is:

$$P_{rad} = \frac{1}{6c^3} B_p^2 R_{NS}^6 \Omega^4 \sin^2\vartheta, \tag{4.8}$$

where $\Omega = 2\pi/P$ is the angular velocity of the pulsar and B_p is the magnetic field strength at the pole. Imaging that all the rotational energy rate goes in magnetic radiation,

$$P_{rad} = -\frac{dE_{rot}}{dt}, \tag{4.9}$$

the magnetic field is:

$$B_p = \sqrt{\frac{3c^3 I}{2\pi^2 R_{NS}^6}} \sqrt{P\dot{P}}. \tag{4.10}$$

For a pulsar, both the period P and the period derivative $\dot{P} = dP/dt$ can be directly observed. From equation (4.9) is it possible to deduce also a relation for $\dot{\Omega}$:

$$\dot{\Omega} = -\frac{B_p^2 R_{NS}^6 \sin^2\vartheta}{6c^3 I}\Omega^3 = -\frac{2M_\perp^2}{3c^3 I}\Omega^3 = -k\Omega^3. \tag{4.11}$$

For a generic magnetic field (instead of a magnetic dipole), equation (4.11) becomes:

$$\dot{\Omega} = -k\Omega^n, \tag{4.12}$$

where n is the braking index that is hard to measure due to timing noise and glitches in the pulsar's phase. Up to now, the braking index was measured in few pulsars and in all cases $n < 3$. This suggests that there are additional processes, besides magnetic dipole radiation, that contribute to the energy release. From equation:

$$\ddot{\Omega} = -nk\Omega^{n-1}\dot{\Omega} = n\frac{\dot{\Omega}^2}{\Omega}, \tag{4.13}$$

it is possible to evaluate the braking index n as:

$$n = \frac{\Omega\ddot{\Omega}}{\dot{\Omega}^2} = 2 - \frac{P\ddot{P}}{\dot{P}^2}. \tag{4.14}$$

The solution of the differential equation (4.12), assuming that k is time independent, give us the information about the pulsar age τ_{age} as a function of Ω, $\dot{\Omega}$ and the initial angular velocity Ω_0:

$$\tau_{age} = \frac{\Omega}{(1-n)\dot{\Omega}}\left[1 - \left(\frac{\Omega}{\Omega_0}\right)^{n-1}\right]. \tag{4.15}$$

Remembering equation (4.12), it is possible to rewrite equation (4.15) as:

$$\tau_{age} = \frac{P}{(n-1)\dot{P}} - \tau_0, \tag{4.16}$$

where $\tau_0 = \Omega_0/[(1-n)\dot{\Omega}_0]$ is the initial spin-down time scale of the pulsar. The integration of equation (4.12) can be also used to evaluate Ω:

$$\Omega = \left[\Omega_0^{1-n} + (n-1)kt\right]^{-\frac{1}{n-1}} \tag{4.17}$$

and consequently:

$$\dot{\Omega} = -k\Omega^n = -k\left[\Omega_0^{1-n} + (n-1)kt\right]^{-\frac{n}{n-1}}. \tag{4.18}$$

The evaluation of the spin-down luminosity (L_{sd}) comes from equation (4.9) (Pacini & Salvati 1973):

$$L_{sd} = -I\Omega\dot{\Omega} = kI\Omega_0^{n+1}\left[1 + \frac{(n-1)kt}{\Omega_0^{1-n}}\right]^{-\frac{n+1}{n-1}}. \tag{4.19}$$

Defining $L_0 = kI\Omega_0^{n+1}$ the initial spin-down luminosity, it is possible to rewrite equation (4.19) as:

$$L_{sd} = L_0\left[1 + \frac{(n-1)L_0P_0^2}{4\pi^2 I}t\right]^{-\frac{n+1}{n-1}} = L_0\left(1 + \frac{t}{\tau_0}\right)^{-\frac{n+1}{n-1}}. \tag{4.20}$$

If $n = 3$, pulsars which are relatively old ($P_0 \ll P$), we obtain what is called the characteristic age of the pulsar:

$$\tau_c = \frac{P}{2\dot{P}}. \tag{4.21}$$

Usually the observable pulsar parameters are its period and the first period derivative. If also the second period derivative is known, the evaluation of n is possible from equation (4.14). Now, if τ_{age} or P_0 are known, it is possible to evaluate all the other pulsar parameters as the spin-down luminosity. We will see in the next sections that the first case (τ_{age} is known) is represented by the Crab object, while the second one (P_0 is assumed known) can be used for Vela.

4.1.2 The pulsar distance

Another pulsar parameter that it is possible to determine is its distance. There are, at least, three method for this measure:

- the first method, distances determined by the annual trigonometric parallax measurements, is used for few relatively nearby pulsars;

- the most commonly used technique to obtain radio pulsar distances exploits the pulse delay as a function of wavelength by free electrons along the path to Earth. A distance can be computed from the dispersion measure (DM) that is the integrated column density of free electrons between the observer and a pulsar (Cordes & Lazio 2002). A wave packet in plasma will propagate with the group velocity:

$$v_g = c\sqrt{1 - \frac{\omega_{pl}^2}{\omega^2}} \tag{4.22}$$

  where $\nu_{pl} = \omega_{pl}/2\pi = \sqrt{4\pi n_e e^2/m_e}/2\pi$ is the plasma frequency depending on the electron density n_e. Now, if we suppose that an astrophysical object, e.g., a pulsar, emits a pulse of radiation at $t = 0$ and the distance to the pulsar is L, the travel time spent by a frequency $\nu = \omega/2\pi$ is:

$$\begin{aligned} t &= \int_0^L \frac{dL}{v_g(\omega)} \approx \int_0^L \frac{dL}{c}\left(1 + \frac{1}{2}\frac{\omega_{pl}^2}{\omega^2}\right) \\ &= \frac{L}{c} + \frac{1}{2c\omega^2}\int_0^L \omega_{pl}^2 dL = \frac{L}{c} + \frac{e^2}{2\pi m_e c\nu^2} DM, \end{aligned} \tag{4.23}$$

  where the dispersion measure (DM) is defined as

$$DM = \int_0^L n_e dL. \tag{4.24}$$

  Knowing the electron density it is possible to evaluate the pulsar distance inverting equation (4.23);

- a third method, kinematic, associates the pulsar with objects whose distance can be measured from the Doppler shift of absorption or emission lines in the neutral hydrogen (HI) spectrum, together with a rotation curve of the Galaxy.

4.1.3 The pulsar magnetosphere

The basic picture of a pulsar magnetosphere was first presented in Goldreich & Julian (1969). The magnetic dipole of the rotating NS creates a quadrupole electric field. For NS, the electric potential produced is much larger than the gravitational force and acts as a powerful particle accelerators. Particles in the outer layers of the pulsar are accelerated to relativistic speeds by the strong electromagnetic field; these particles follow the magnetic field lines away from the pulsar. The particles' acceleration along these magnetic field lines results in the emission of curvature radiation which is seen when the emitting pole passes a distant observer, creating the pulsed emission for which these objects are known. Some relativistic electrons which are accelerated away from the surface of the neutron star escape at the magnetic poles, where the field lines are not closed; these electrons enter the surrounding supernova remnant and their interaction with the SNR create a pulsar wind nebula. Inside the magnetosphere the interactions between photons and the high magnetic fields generate pairs (Sturrock 1971; Erber 1966) that can generate again curvature photons. At the end, electromagnetic showers are produced. On the other hand, there is still much debate about the location of the gamma-ray emission. In the polar cap (PC) model, the gamma-ray emission arises inside one stellar radius (Ruderman & Sutherland 1975; Daugherty & Harding 1996). In the outer gap (OG) and slot gap (SG) models, gamma-ray emission is predicted near the pulsar's light cylinder (the cylinder centred on the pulsar and aligned with the rotation axis at whose radius the co-rotating speed equals the speed of light) (Cheng et al. 1986; Zhang L. 2001; Romani 1996; Harding et al. 2008).

4.1.4 Pulsar photon spectrum

Pulsars are among the most likely sources of electron-positron pairs. Due to their energy loss, the particle spectrum must be related to the photon one. In this section we present the gamma-ray spectrum of these sources.

Over 2300 pulsars are now listed in the ATNF pulsar catalogue[2] (Manchester et al. 2005). These sources were discovered by radio telescopes. Some of them were observed in the optical band and few in X-ray bands. The satellites those start

[2] `http://www.atnf.csiro.au/research/pulsar/psrcat/` (2014)

to observe the sky in the high energy gamma-ray domain (photon energy > 30 MeV) were: SAS-2, COS-B and CGRO with EGRET. The third EGRET catalogue (Hartman et al. 1999) included 271 sources, some of them are associated with regions around pulsars. In this section, we restricted the analysis on the pulsars reported in the second Fermi Large Area Telescope (LAT) catalogue of gamma-ray pulsars (Abdo et al. 2013) (see appendix B). The LAT is sensitive to gamma-rays with energies in the range from 20 MeV to greater than 300 GeV, and its on-axis effective area is ~ 8000 cm^2 for $E > 1$ GeV. The first Fermi catalogue summarizes 46 pulsed detections using the first six months of data taken. Using 3 years of data, this second catalogue reports a list of 117 pulsars significantly detected by the LAT with three methods (Abdo et al. 2013). 61 of the gamma-ray emitting pulsars were observed in locations previously marked and detected in radio or X-ray energies. Others 36 objects were searched blindly using gamma-ray data because some pulsars are known to emit only gamma-rays. Finally, the positions of unidentified LAT sources which could potentially be associated with pulsars were found in regions characterised by radio emission. This method leads to detect other 20 new millisecond pulsars. The scatter plot reported in figure 4.2 reports the characteristic age and distance of these objects where available. Known pulsars as Crab (J0534+2200), Geminga

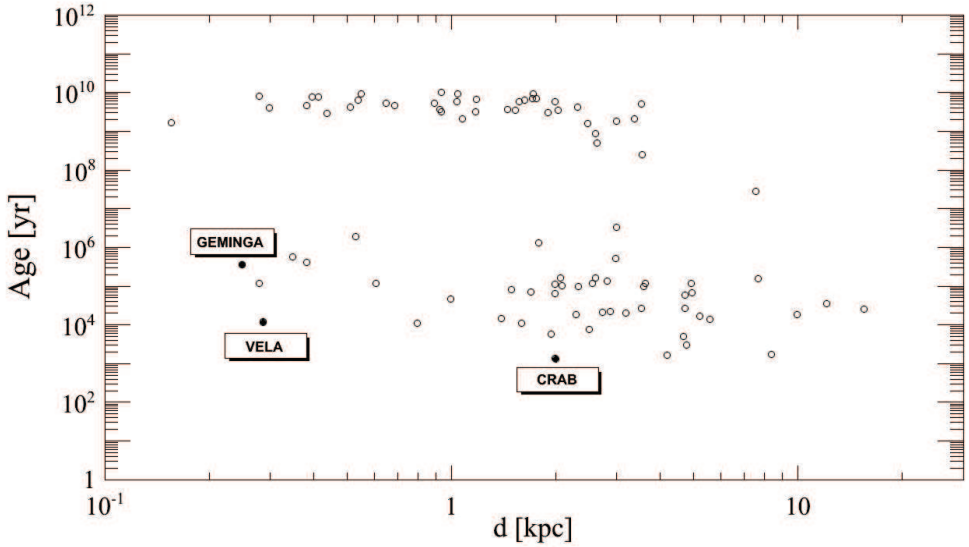

Figure 4.2: Scatter plot with age and distance of pulsar presented in the second Fermi catalogue (Abdo et al. 2013). Crab, Vela and Geminga are reported in full dots.

(J0633+1746) and Vela (J0835-4510) are also reported. The family of objects with characteristic age higher than 10^8 years is composed by millisecond pulsars. In table 4.1 we reports the parameters of all the pulsars in the second FERMI catalogue

inside two kpc from the Solar System.

Table 4.1: The pulsar parameters are reported: period P, period time derivate $\dot{P}$, distance d, age τ_c and spin-down luminosity $\dot{E}_{sd}$.

Pulsar name	P	$\dot{P}$	L_{sd}	d	τ_c
	ms	10^{-15} s s^{-1}	10^{34} erg s^{-1}	kpc	kyr
J0007+7303	315.89	357	44.8	1.4	14.0195
J0023+0923	3.05	1.09e-05	1.51	0.69	4.43343e+06
J0030+0451	4.87	1.02e-05	0.362	0.28	7.56475e+06
J0034-0534	1.88	4.98e-06	1.72	0.54	5.98129e+06
J0101-6422	2.57	4.8e-06	1.01	0.55	8.48317e+06
J0205+6449	65.73	190	2640	1.95	5.48121
J0248+6021	217.11	55	21.2	2	62.5436
J0340+4130	3.3	5.9e-06	0.787	1.73	8.86192e+06
J0437-4715	5.76	5.73e-05	0.291	0.156	1.5927e+06
J0534+2200	33.63	420	43600	2	1.26866
J0613-0200	3.06	9.59e-06	1.2	0.9	5.05556e+06
J0614-3329	3.15	1.78e-05	2.2	1.9	2.80386e+06
J0631+1036	287.8	105	17.3	1	43.4278
J0633+1746	237.1	11	3.25	0.25	341.511
J0659+1414	384.89	55	3.81	0.28	110.877
J0751+1807	3.48	7.78e-06	0.721	0.4	7.08705e+06
J0835-4510	89.36	125	690	0.287	11.3266
J1024-0719	5.16	1.85e-05	0.046	0.386	4.4192e+06
J1057-5226	197.11	5.83	3.01	0.35	535.681
J1124-3653	2.41	5.75e-06	1.71	1.72	6.64072e+06
J1231-1411	3.68	2.12e-05	0.515	0.438	2.75029e+06
J1418-6058	110.58	169	494	1.6	10.3671
J1446-4701	2.19	9.85e-06	3.68	1.46	3.52269e+06
J1514-4946	3.59	1.87e-05	1.6	0.94	3.04172e+06
J1600-3053	3.6	9.5e-06	0.73	1.63	6.00406e+06
J1614-2230	3.15	9.62e-06	0.378	0.65	5.18802e+06
J1658-5324	2.44	1.1e-05	3.02	0.93	3.5145e+06
J1713+0747	4.57	8.53e-06	0.344	1.05	8.48854e+06
J1732-3131	196.54	28	14.6	0.609	111.214
J1741-2054	413.7	17	0.947	0.384	385.569
J1741+1351	3.75	3.02e-05	2.18	1.08	1.96739e+06

(Continued on next page)

(Continued from previous page)

J1744-1134	4.07	8.92e-06	0.411	0.417	7.22929e+06
J1809-2332	146.79	34.4	43	1.7	67.6089
J1810+1744	1.66	4.63e-06	3.97	2	5.68059e+06
J1836+5925	173.26	1.5	1.14	0.53	1830.09
J1858-2216	2.38	3.87e-06	1.13	0.94	9.74388e+06
J1902-5105	1.74	9e-06	6.86	1.18	3.06318e+06
J1952+3252	39.53	5.83	372	2	107.43
J2017+0603	2.9	8.3e-06	1.3	1.57	5.53587e+06
J2021+4026	265.32	54.2	11.4	1.5	77.5598
J2043+1711	2.38	5.7e-06	1.27	1.76	6.61558e+06
J2043+2740	96.13	1.23	5.46	1.8	1238.28
J2051-0827	4.51	1.28e-05	0.542	1.04	5.58255e+06
J2124-3358	4.93	2.06e-05	0.367	0.3	3.7918e+06
J2214+3000	3.12	1.5e-05	1.92	1.54	3.29556e+06
J2229+6114	51.64	77.9	2230	0.8	10.503
J2241-5236	2.19	8.7e-06	2.6	0.513	3.98833e+06
J2302+4442	5.19	1.33e-05	0.382	1.19	6.18275e+06

Table 4.1: The pulsar parameters are reported: period P, period time derivate $\dot{P}$, distance d, age τ_c and spin-down luminosity $\dot{E}_{sd}$.

In the fourth column of table 4.1, the spin-down luminosity is evaluated from equation (4.19) as follow:

$$L_{sd} = -I\Omega\dot{\Omega} = 4\pi^2 I\dot{P}P^{-3}; \tag{4.25}$$

while the sixth column report the characteristic age calculated using equation (4.21).

The pulsar photon spectra were fitted with an exponentially cut-off power-law equation:

$$\frac{dN}{dE} = KE^{-\Lambda}\exp\left(-\frac{E}{E_{cut}}\right) \tag{4.26}$$

in which the three parameters are the photon index at low energy (Λ), the energy cut-off (E_{cut}) and the normalization factor (K). The energy cut-offs recording in Abdo et al. (2013) are reported in figure 4.3. It is possible to see that all the cut-offs are below 10 GeV. In the next sections, we will discuss the very high energy photon emissions observed around some pulsars (in a region called nebula that surround these objects) in which higher electrons and positrons interact with the magnetic

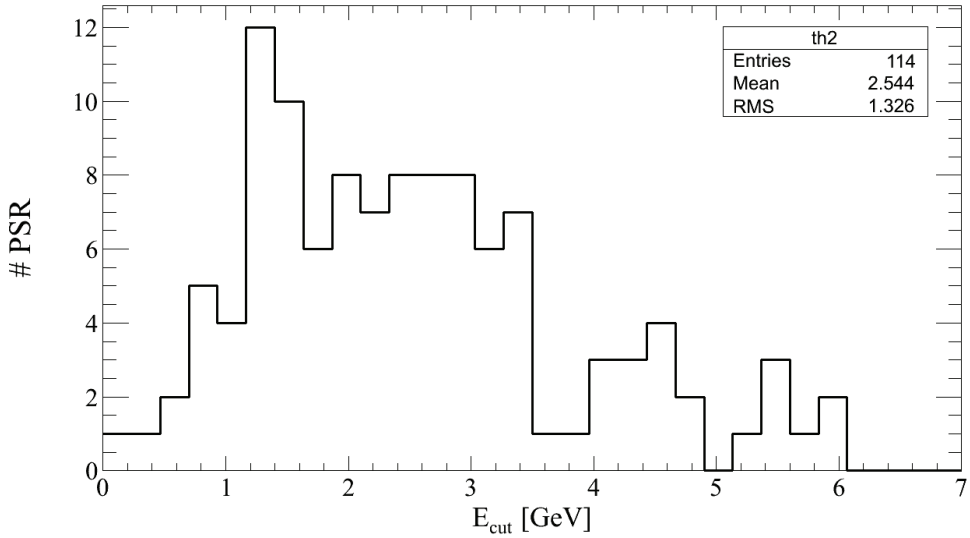

Figure 4.3: Energy cut-offs for pulsars presented in the second Fermi catalogue (Abdo et al. 2013).

and radiation fields. These particles may be responsible for the excess spectra for electrons above ~ 90 GeV and positrons above ~ 10 GeV (see figure 3.11).

4.2 Pulsar Wind Nebula

Pulsar wind nebula identifies a region around the pulsar where a relativistic magnetized wind is populated with electron and positron pairs (Kaspi et al. 2006; Blasi & Amato 2011). The gamma ray spectra of PWN reach very high energy, for instance, tens of TeV. Pulsar wind nebulae are widely believed to be responsible for the acceleration of cosmic rays up to energies of 10^{15} eV (see Rees & Gunn 1974; Kennel & Coroniti 1984a,b). The central pulsar converts its spin-down power into a relativistic wind injected near the magnetosphere. The electrons and positrons in the wind, interacting with the shock front, are accelerated and get a power-law energy spectrum. They radiate at lower energies, from radio frequencies to X-ray, through the synchrotron process in the magnetic field of the nebula. The higher energy part of the spectrum comes from inverse Compton scattering on the radiation field composed by: synchrotron radiation in the PWN, cosmic microwave background (CMB), infrared and star-light photons (see e.g., de Jager & Harding 1992; Atoyan & Aharonian 1996; Hillas et al. 1998). The observed synchrotron emission is usually used to extract the electron energy distribution (Hillas et al. 1998; de Jager et al. 1996). The observed high-energy emission from the Crab Nebula has been modelled in detail by several authors (see de Jager & Harding 1992; Atoyan & Aharonian 1996; de Jager

et al. 1996; Hillas et al. 1998; Bednarek & Bartosik 2003). High-energy processes in other PWNe such as that of the Vela-SNR, the nebulae around PSR 1706-44, PSR 1509-58, 3C 58, CTB 80 and other few nebulae have been also studied in detail in Aharonian et al. (1997); Du Plessis et al. (1995); Sefako & de Jager (2003); Horns et al. (2006); Bednarek & Bartosik (2003). It is also possible that the production of gamma-rays in the interactions of hadrons with the matter of the supernova could contribute to the higher energy end of the observed spectrum, especially in the case of younger nebulae (see Cheng et al. 1990; Atoyan & Aharonian 1996; Bednarek & Protheroe 1997; Horns et al. 2006). In the next section the procedure to get electron and positron injection spectra responsible to the PWN gamma-ray spectrum will be presented.

4.2.1 Particle spectrum from PWN

To evaluate the energy spectrum of electrons and positrons at the source, we follow the approach described in Zhang et al. (2008). This method is similar with others reported in Tanaka & Takahara (2010); Martín et al. (2012). For a given pulsar, the evolution of the spin-down power $L(t)$ is given by equation (4.20) hereafter reported:

$$L_{sd}(t) = L_0 \left[1 + \frac{(n-1)P_0^2 L_0 t}{4\pi^2 I}\right]^{-\frac{n+1}{n-1}}, \tag{4.27}$$

where L_0 and P_0 represent the spin-down power and pulsar period at the pulsars birth, n is the braking index assumed to be constant, and I is the moment of inertia. A relativistic wind of electrons produced within the light cylinder of the pulsar is injected into the PWN. This spectrum is assumed to be a broken power law with different indices and an energy break E_b. The radio electron component dominates below E_b and has an index α_1, while the wind electron component is dominant above E_b, with an index α_2 (Atoyan & Aharonian 1996). Following Venter & de Jager (2007), we assume that the electron injection rate at the shock radius r_s of the PWN follows a broken power law with indices α_1 and α_2 and energy break E_b:

$$Q(E_e, t) = \begin{cases} Q_0(t)(E_e/E_b)^{\alpha_1} & \text{if } E_e < E_b, \\ Q_0(t)(E_e/E_b)^{\alpha_2} & \text{if } E_e > E_b, \end{cases} \tag{4.28}$$

where E_e is the particle kinetic energy and $Q_0(t)$ can be derived by requiring the continuity of the two power law:

$$\int_{E_{min}}^{E_{max}} Q(E_e, t) E_e dE_e = \eta L_{sd}(t), \tag{4.29}$$

with η the conversion factor of the spin-down power $L_{sd}(t)$ into particle luminosity. Substituting equations (4.27) and (4.28) into equation (4.29) we have:

$$Q_0(t) = \eta L_{sd}(t) \left[\frac{E_b^2(\alpha_1 - \alpha_2)}{(2-\alpha_1)(2-\alpha_2)} + \frac{E_b^{\alpha_2} E_{max}^{2-\alpha_2}}{2-\alpha_2} - \frac{E_b^{\alpha_1} E_{min}^{2-\alpha_1}}{2-\alpha_1} \right]^{-1}. \tag{4.30}$$

In order to confine the accelerated particles within the PWN, the electrons Larmor radius r_L must be lower than the radius of the PWN, here we take $r_L < 0.5 r_s$ as pointed out by Venter & de Jager (2007) (r_s is the shock radius). Thus, the maximum energy is:

$$E_{max}(t) \approx \frac{e}{2} \sqrt{\frac{1}{4\pi\epsilon_0} \frac{\sigma}{\sigma+1} \frac{L(t)}{c}}. \tag{4.31}$$

The diffusion equation for the differential electron density $n_e(E_e, t)$ can be approximated as (see e.g., Zhang et al. 2008; Tanaka & Takahara 2010; Martín et al. 2012):

$$\frac{dn_e(E_e,t)}{dt} = Q(E_e,t) - \frac{n_e(E_e,t)}{\tau_{syn}(t)} - \frac{n_e(E_e,t)}{\tau_{esc}(t)}. \tag{4.32}$$

The particle spectrum obtained as a solution of the equation (4.32) over time from $t = 0$ to $t = T$ (age of the PWN) is (Zhang et al. 2008):

$$\frac{dN(E_e,T)}{dE_e} = \int_0^T Q(E_e,t) \exp\left(-\frac{T-t}{\tau_{eff}}\right) dt; \tag{4.33}$$

where $\tau_{eff}^{-1} = \tau_{syn}^{-1} + \tau_{esc}^{-1}$ corresponds to the lifetime of an electron with respect to both synchrotron energy loss and escape timescale (i.e., the time to diffuse 1 PWN radius), which are given by:

$$\tau_{syn}(t) \approx 1.25 \cdot 10^4 \left(\frac{B(t)}{10\,\mu\mathrm{G}}\right)^{-2} \left(\frac{E_e}{10\,\mathrm{TeV}}\right)^{-1} \mathrm{yr} \tag{4.34}$$

and

$$\tau_{esc}(t) \approx 3.4 \cdot 10^4 \left(\frac{B(t)}{10\,\mu\mathrm{G}}\right) \left(\frac{E_e}{10\,\mathrm{TeV}}\right)^{-1} \left(\frac{R_{PWN}}{1\,\mathrm{pc}}\right)^{2} \mathrm{yr}. \tag{4.35}$$

The PWN radius R_{PWN}, the magnetic field $B(t)$ and other parameters are evaluated from the fit of the gamma-ray spectrum of the PWN.

4.2.2 The Vela-X case

The pulsar J0534+2200, located inside the Crab Nebula, the remnant of a supernova explosion occurring in A.D. 1054, is extremely a well studied object. This young source can give us information about the first step of the life of a generic PSR/PWN. Note that the Crab distance is about 2 kpc and, due to the age, we can not see yet particles coming from that source at the Earth position. The TeVCat catalogue[3] contains less than 40 PWN observed in the TeV energy range. Only five of them are closer than 2 kpc and were observed by Cherenkov telescope experiments like HESS (Aharonian et al. 2006a,b), Veritas (Aliu et al. 2013; Humensky 2009) and Magic (Aleksi et al. 2012). Vela-X belongs to this sample. These observations regard a small fraction of known pulsars and they are much less complete and accurate in comparison with the Crab Spectral Energy Distribution (SED). Indeed it is widely believed that PWN's are not more observable after the early phase of expansion. Malyshev et al. (2009) suggested that all the pulsars have an initial stage as PWN and the lifetime of these objects is about 10^3-10^4 years. During this phase electrons and positrons are trapped inside the PWN, but later, after a time T from the SN explosion, they are free to propagate. Mature pulsars, like Geminga and Monogem, have no more gamma-ray emission from the nebula, but the electrons and positrons released are still coming to the Earth. For all the older pulsars we do not have information regarding the nebula photon spectrum, the braking index or the birth frequency. For what concerns the PSR age, we can roughly estimate the minimum characteristic age $\tau_c = P/2\dot{P}$ as reported in Abdo et al. (2013).

Model 1: using observed parameters for Vela-X

The observation of the timing property of the pulsar gives us the basic information to evaluate the braking index as in Eq. (4.14). Vela is one of the few sources (Yue et al. 2007) for which it is possible to measure the braking index: $n = 1.4 \pm 0.2$ (Lyne et al. 1996). Therefore, we built a model based on the observed parameters of Vela. Lyne et al. (1996) reports, in their work, the following parameters: frequency $\nu \sim 11.2$ Hz, first derivative $\dot{\nu} \sim -157 \times 10^{-3}$ Hz s^{-1} and second derivative $\ddot{\nu} = (31 \pm 4) \times 10^{-24}$ Hz s^{-2}. The electron-positron spectrum produces, via synchrotron and inverse Compton processes, a photon spectrum in agreement with the observations. We assume a value of n that is not time dependent. We do not have information on the birth time and assume the same initial rotation period of the Crab pulsar ($P_0 \sim 20$ ms, Manchester & Taylor 1977). In this way equation (4.15)

[3] `http://tevcat.uchicago.edu/` (2014)

gives an age, for Vela, of $\tau_{age} \sim 26$ kyrs (instead of the common characteristic age $\tau_c = 11$ kyrs). Vela-X was detected by HESS (Aharonian et al. 2006b) in the very high energy gamma ray band, the spectrum can be fitted by a power law with the photon index $\Gamma_\gamma = 1.45 \pm 0.09_{stat} \pm 0.2_{sys}$ in the energy range between 550 GeV and 65 TeV and an exponential cut-off at an energy of $13.8 \pm 2.3_{stat} \pm 4.1_{sys}$ TeV. The X-ray part was detected using ROSAT combined with ASCA data (Markwardt & Ögelman 1995, 1997). The spectrum observed in this region has a spectral index of $\Gamma_X \sim 2$. The results reported in figure 4.4 (Model 1) come from this analysis. We get a photon spectrum compatible with the HESS and ASCA data requiring a conversion efficiency of the spin down luminosity of about $\eta = 0.5\%$ for both electrons and positrons. Model 1 represents the diffused spectrum at the Earth evaluated with equation (3.13) using $t = \tau_{age} - T$. We set $T \sim 10$ kyrs, in comparison with the initial spin-down time scale which is evaluated to be $\tau_0 \sim 29$ kyrs. The band of the model reflects only the uncertainty on the Vela pulsar distance that is about 6% (Vela distance is 287^{+19}_{-17} pc, Abdo et al. 2013).

Model 2: using Crab-like parameters for Vela-X

Observation of the timing properties of the other pulsars, younger than Vela, for which the braking index n is known, this values is between 2 and 3 (Yue et al. 2007). All of them are more similar to the value of the Crab nebula with respect to Vela-X. Therefore, we can alternatively assume that all the pulsars are similar at their birth and we can take the properties (initial rotation period, braking index) of Crab. We need to assume that there is a variation of the braking index from 2.5, at the birth, down to 1.4, at later time. It could be associated to some changes in the structure of the neutron star, as suggested by the observation of glitches in the rotation period (Lyne et al. 1996). We do not have a model for this variation and, therefore, it is not currently possible to evaluate the photon spectra at the present day, but we can use the Crab photon spectra observed after ~ 1000 years from the birth. For the Crab-like source the initial spin-down time scale is $\tau_0 \sim 700$ years and the characteristic age is $\tau_c \sim 11$ kyr. Therefore, we take electron-positron spectra, normalized to the photon emission like in the Crab nebula, and propagate the source spectrum after $T \sim 1000$ years, as assumed in Malyshev et al. (2009) (Vela distance is always ∼287 pc). In figure 4.4 the positron or electron spectrum, obtained from equation (3.13) using all the Crab parameters, is shown for Vela-X (Model 2). The main parameters of the two models are summarized in table 4.2.

From an inspection of figure 4.4, one may remark that the measured electron and positron intensities can be accounted by the flux expected from Vela-X within

Parameter	Symbol	Model 1	Model 2
Q index 1	α_1	1.9	1.5
Q index 2	α_2	2.8	2.4
Q break energy (MeV)	E_b	$1.5 \cdot 10^5$	$1.5 \cdot 10^5$
Braking index	n	1.4	2.5
Conversion factor (%)	η	0.5	5
Birth period (ms)	P_0	20	20
Age (kyr)	τ_{age}	26	11
Spin-down time scale (kyr)	τ_0	29	0.7
Emission time	T (kyr)	10	1

Table 4.2: Parameters used in Model 1 and 2 for Vela-X nebula.

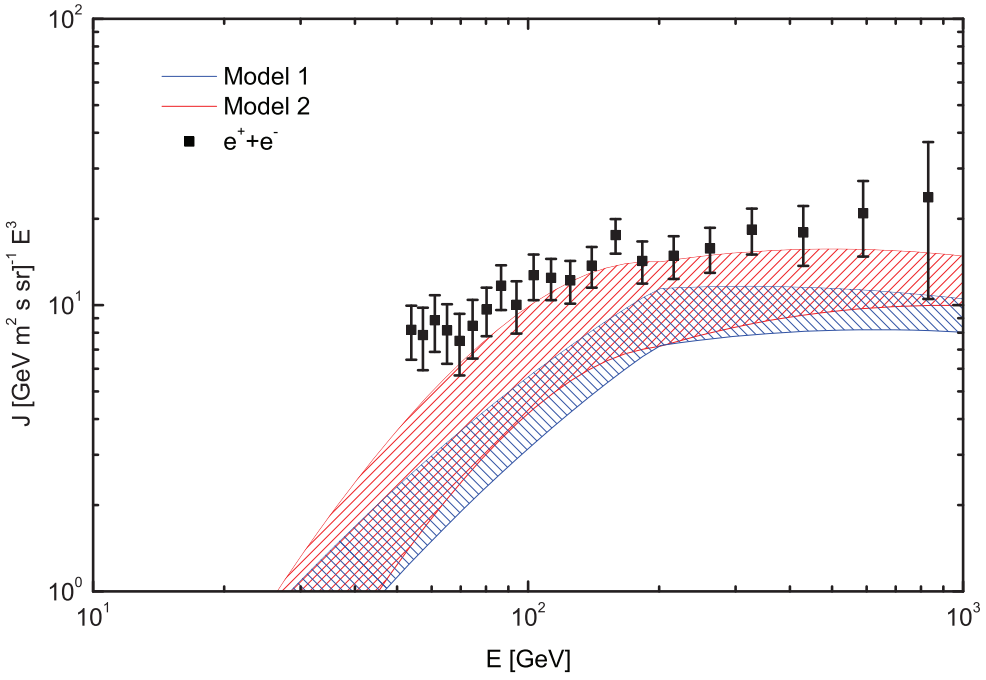

Figure 4.4: Two model of this analysis of the expected positron or electron omnidirectional intensities from Vela-X compared with the half electron plus positron signal as in figure 3.11.

model 2. However, it is noticeable that all points are systematically slightly above the expectations.

Comparison with data indicates the possibility of an extra source similar to Vela. There is only another known pulsar, B1737-30 (or J1740-3015), with parameters similar to Vela. It is 400 pc far and 20600 years old (Clifton & Lyne 1986; Yuan et al. 2010), but the photon emission of its nebula has not been observed yet. Moreover, statistically, we expect just one (or very few) more pulsar like Vela; in fact, considering a pulsar birth rate of 0.9-2 objects per century (Taani et al. 2012; Lorimer 2008) and a spatial distribution like in Taani et al. (2012) and Sartore et al. (2009), a couple of pulsars, with age from 10 to 50 kyrs in a volume of about 1 kpc^3 around the Earth, are expected.

At energy lower than 100 GeV, a contribution of aged pulsars (10^5 yrs) is expected. There are several of them close to the Earth, like Geminga or Monogem, which may contribute, but the emission of their PWN is no more observable.

4.3 CR Anisotropy

As pointed out in section 4.2.2, a single pulsar wind nebula, Vela-X, may be responsible for about half of the electron and positron excess in CRs. If our model is correct, an evident dipole signal in the CR arrival direction could be detected. In this section, we will evaluate the dipole signal from single source for electrons and positrons.

Observation of isotropy or anisotropy in the CR-sky could give us information about areas where these particles are produced. This study can be done detecting the arrival directions of CRs. As already mentioned in chapter 3, magnetic field and diffusion process influence the particle trajectories which are propagating in the Galaxy and, for this reason, it is impossible to accurately evaluate source positions without knowing the crossed fields. Nevertheless, having a specific source, it is possible to determine the anisotropy of CRs under the common assumption that the particle propagation in the Galaxy is usually described under the diffusion approximation (see e.g., Ginzburg & Ptuskin 1976; Linden & Profumo 2013; Ackermann et al. 2010). The degree of cosmic ray anisotropy from a single source is defined as:

$$\delta = \frac{I_{max} - I_{min}}{I_{max} + I_{min}}, \tag{4.36}$$

where $I\,[\#/(\mathrm{m}^2\,\mathrm{s}\,\mathrm{sr})]$ is the particle intensity depending on the direction. Considering a dataset consisting of the sum of a perfectly isotropic signal of constant intensity

I_0 and of a dipole anisotropy of maximum intensity I_1, the overall intensity at an angular distance ϑ from the maximum of the dipole anisotropy will be: $I(\vartheta) = I_0 + I_1 \cos\vartheta$. In this case, I_{max} becomes $I_0 + I_1$ (pointing in the source direction), while $I_{min} = I_0 - I_1$ (pointing in the opposite direction of the source) and the degree of the dipole anisotropy is:

$$\delta = \frac{I_1}{I_0}. \tag{4.37}$$

A more robust method involves a spherical harmonic analysis of the "fluctuations sky map" equal to the ratio of the actual and no-anisotropy sky maps minus one. This sky map is expanded in the basis of the spherical harmonics, producing a set of coefficients $a_{l,m}$; then, an angular power spectrum is constructed by calculating the variance of the $a_{l,m}$ coefficients at each multipole l as:

$$C_l = \frac{1}{2l+1} \sum_{m=-l}^{l} |a_{l,m}|^2. \tag{4.38}$$

The fluctuation map describing $I(\vartheta)$ is:

$$f(\vartheta) = \frac{I(\vartheta) - < I(\vartheta)}{I(\vartheta)} = \frac{I(\vartheta) - I_0}{I_0} = \frac{I_1}{I_0}\cos(\vartheta). \tag{4.39}$$

Among the spherical harmonic basis, we can find that:

$$Y_{1,0}(\vartheta, \varphi) = \sqrt{\frac{3}{4\pi}}\cos(\vartheta) \tag{4.40}$$

is the term of interest for the expansion of equation (4.39) on the new basis:

$$f(\vartheta) = \sum_l \sum_m a_{l,m} Y_{l,m}. \tag{4.41}$$

Thus, equation (4.39) becomes:

$$f(\vartheta) = \left(\frac{I_1}{I_0}\sqrt{\frac{4\pi}{3}}\right) \times Y_{1,0}, \tag{4.42}$$

and $a_{1,0}$ is:

$$a_{1,0} = \frac{I_1}{I_0}\sqrt{\frac{4\pi}{3}}. \tag{4.43}$$

The only non-zero term of the power spectrum is:

$$C_1 = \frac{1}{3}\sum_{m=-1}^{1}|a_{l,m}|^2 = \frac{1}{3}a_{1,0}^2 = \left(\frac{I_1}{I_0}\right)^2 \frac{4\pi}{9}. \tag{4.44}$$

Since C_l are a rotationally invariant quantity, equation (4.44) is valid in general for every dipole and reference frame. Merging equations (4.37) and (4.44), the relation between the degree of the dipole anisotropy and the value of the dipole power is:

$$\delta = 3\sqrt{\frac{C_1}{4\pi}}. \tag{4.45}$$

While the monopole $l = 0$ is a component expected to be equal to one, the dipole for $l = 1$ is described by three orthogonal functions defined on the celestial sphere. In Galactic coordinates they are aligned with: $Y_{1,0}$ along the North-South (NS) direction perpendicular to the galactic plane, $Y_{1,1}$ along the Forward-Backward (FB) direction with respect to the galactic center and $Y_{1,-1}$ along the East-West (EW) direction tangent to the orbit of the sun around the galactic center (see figure 4.5 and Casaus, J. & the AMS-02 Collaboration 2013). To study these three directions

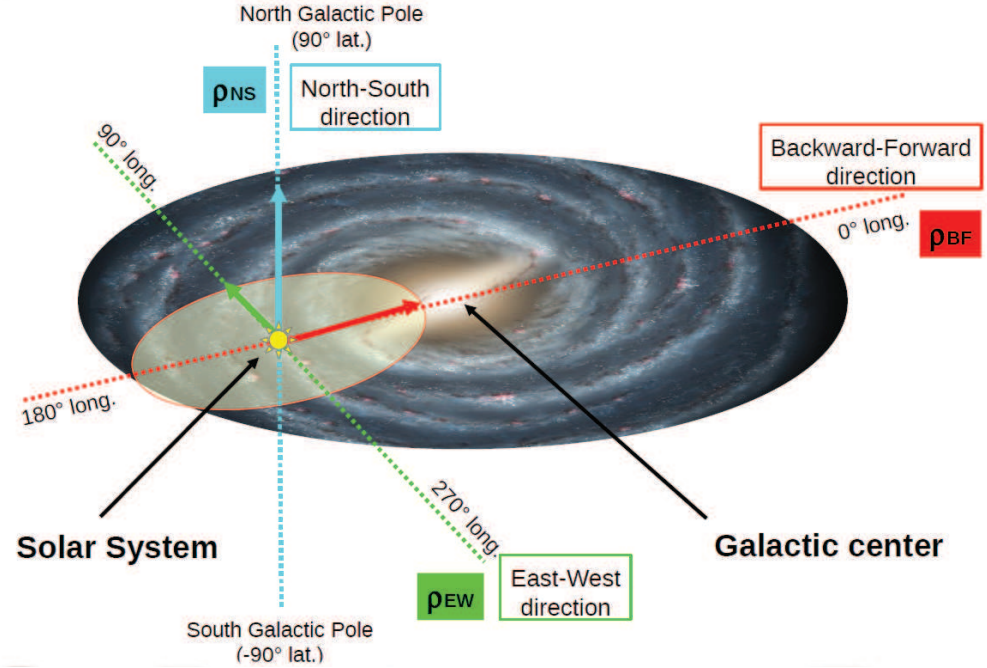

Figure 4.5: Dipole components (North-South, Forward-Backward and East-West) in galactic coordinates.

both separately and combined to determine the total dipole magnitude δ, the known

equation (4.45) allows to give a definition of the three dipole coefficients:

$$\rho_{NS} = \sqrt{\frac{3}{4\pi}} a_{1,0}, \qquad \rho_{FB} = \sqrt{\frac{3}{4\pi}} a_{1,1}, \qquad \rho_{EW} = \sqrt{\frac{3}{4\pi}} a_{1,-1}, \tag{4.46}$$

so that

$$\delta = \sqrt{\rho_{NS}^2 + \rho_{FB}^2 + \rho_{EW}^2}. \tag{4.47}$$

Returning to analyse the CR intensity (I), the particle flux is defined integrating it as following:

$$F \left[\frac{\#}{\mathrm{m}^2\,\mathrm{s}}\right] = \int I(\vartheta) \cos\vartheta d\Omega. \tag{4.48}$$

and in our case:

$$\begin{aligned} F &= 2\pi \int_0^{\pi} I(\vartheta) \cos(\vartheta) \sin(\vartheta) d\vartheta \\ &= 2\pi \left[- \int_1^{-1} I_0 \cos(\vartheta) d\cos\vartheta - \int_1^{-1} I_1 \cos^2(\vartheta) d\cos\vartheta \right] \\ &= \frac{4\pi}{3} I_1 \end{aligned} \tag{4.49}$$

Using the general transport equation:

$$\frac{\partial N_i}{\partial t} - \vec{\nabla} \cdot \left[D_i \vec{\nabla} N_i \right] + \frac{\partial}{\partial E} \left[b_i N_i \right] = Q_i - p_i N_i + P_i, \tag{4.50}$$

for a particle concentration:

$$N_i \left[\frac{\#}{m^3}\right] = \frac{1}{v_i} \int I d\Omega = \frac{4\pi}{v_i} I, \tag{4.51}$$

where v_i is the particle velocity (see e.g., Ginzburg & Ptuskin 1976), the diffusion approximation leads to consider only the first two terms of equation (4.50):

$$\frac{\partial N_i}{\partial t} - \vec{\nabla} \cdot \left[D_i \vec{\nabla} N_i \right] = 0, \tag{4.52}$$

where D_i is the diffusion coefficient. The general continuity equation:

$$\frac{\partial N_i}{\partial t} + \vec{\nabla} \cdot F = 0, \tag{4.53}$$

can be used to define the particle flux as:

$$F = D_i \left| \vec{\nabla} N_i \right|. \tag{4.54}$$

With these new information, we can evaluate the degree of anisotropy from equation (4.37):

$$\delta = \frac{I_1}{I_0} = \frac{3F}{4\pi I_0} = \frac{3D_i \left|\vec{\nabla} N_i\right|}{4\pi I_0}. \tag{4.55}$$

If the anisotropy is small ($I_0 = I - I_1 \cos\vartheta \sim I$), the dipole of anisotropy, using equation (4.51), is obtained as:

$$\delta = \frac{3D_i \left|\vec{\nabla} N_i\right|}{4\pi I} = \frac{3}{\beta c} \frac{D_i \left|\vec{\nabla} N_i\right|}{N_i}. \tag{4.56}$$

4.3.1 Electron and positron anisotropy from Vela-X

Contrary to hadronic CRs, high-energy (> GeV) CR electrons and positrons, propagating in the ISM, lose their energy quickly through synchrotron radiation and by inverse Compton collisions with low-energy photons of the interstellar radiation field. As discussed at the end of section 3.6, these particles, observed with energy of 100 GeV (1 TeV), are originated from relatively nearby sources, with a distance lower than ~ 2 kpc from the Solar System. As already discussed in section 3.5, the propagation of positrons and electrons in the interstellar medium may be described by the diffusion equation (3.6). Using the particle injection spectrum reported in equation (3.12), the solution of the diffusion equation is reported in Malyshev et al. (2009); Ackermann et al. (2010), where:

$$\frac{dN_{e^+,source}(\vec{x}, E, t)}{dE} = \frac{Q_0}{(4\pi\lambda_d^2)^{3/2}} E^{-\alpha} \left(1 - b_0 t E\right)^{\alpha-2} e^{-\frac{E}{E_{cut}(1-b_0 t E)}} e^{-\frac{|\vec{x}|^2}{4\lambda_d^2}}. \tag{4.57}$$

To evaluate the anisotropy from a single source for only positrons, we need to remember that the positron spectrum contains also the secondary component produced in the ISM; thus, the real evaluation is $N_{e^+,tot} = N_{e^+,source} + N_{e^+,cLIS}$. Assuming that particles produced in the ISM (like those that constitute the positron cLIS) are isotropic, equation (4.56) can be reduced to:

$$\delta = \frac{3}{\beta c} \frac{D(E)|\vec{\nabla} N_{e^+,tot}|}{N_{e^+,tot}} = \frac{3D(E)}{\beta c} \frac{2|\vec{x}|}{4\lambda_d^2} \frac{N_{e^+,source}}{N_{e^+,tot}}. \tag{4.58}$$

Using the electron (or positron) diffused spectrum from a single source, it is possible also to justify the approximation $I_0 \sim I$. In fact, if we keep the real I_0, we obtain

($\beta \approx 1$):

$$\begin{aligned}\delta &= \frac{3F}{4\pi(I - I_1\cos\vartheta)} = \frac{3D_i\left|\vec{\nabla}N_i\right|}{4\pi\left(\frac{cN_i}{4\pi} - D_i\left|\vec{\nabla}N_i\right|\cos\vartheta\right)} \\ &= \frac{3D_i\left|\vec{\nabla}N_i\right|}{cN_i - 4\pi D_i\left|\vec{\nabla}N_i\right|\cos\vartheta} = \frac{3D_i\left|\vec{\nabla}N_i\right|}{N_i\left(c - 4\pi D_i\frac{2|\vec{x}|}{4\lambda_d^2}\cos\vartheta\right)}.\end{aligned} \tag{4.59}$$

Since:

$$4\pi D_i\frac{2|\vec{x}|}{4\lambda_d^2}\cos\vartheta \propto \frac{D_i|\vec{x}|}{D_i t_{diff}} = \frac{|\vec{x}|}{t_{diff}}, \tag{4.60}$$

where t_{diff} is the diffusion time, the approximation $I_0 \sim I$ is valid if $t_{diff} \gg |\vec{x}|/c = t_{light}$ (diffusion approximation).

The most precise available data for electrons and positrons come from the FERMI experiment (Ackermann et al. 2010) which reports the upper limit at 95% of confidence level for the electron plus positron dipole signal, because FERMI-LAT can not distinguish the particle charge signs. In this case, equation (4.56) must be rewritten as in equation (4.61), where ($N_{e^-,source} = N_{e^+,source}$) because PWN produces these particles in pairs:

$$\delta = \frac{3D(E)}{\beta c}\frac{2|\vec{x}|}{4\lambda_d^2}\frac{2N_{e^+,source}}{2N_{e^+,source} + N_{e^+,cLIS} + N_{e^-,cLIS}}. \tag{4.61}$$

The results for both Models 1 and 2, shown in section 4.2.2, are reported in figure 4.6. The FERMI-LAT experiment is designed for detecting photons, but it can also work as a detector of high-energy CR electrons and positrons. The analysed dataset corresponds to the first year of LAT science operation and start on August 2008. To minimize the geomagnetic fields influence, the FERMI collaboration has selected $\sim$ 1.6 million events with an energy high enough ($E > 60$ GeV) to elude this effect. Figure 4.6 reports the upper limit of the dipole anisotropy, for electrons plus positrons, that can be even lower increasing the statistics (i.e., keep into account more data from the later years). At the moment, Vela-X, obtained with our models, is not yet visible in the CR-sky; moreover, to increase the excess components (see discussion at the end of section 4.2.2), we need a new source, if this object is located on the opposite galactic longitude side of Vela, the sum of the two signals of anisotropy can be lower than the two solid lines in figure 4.6.

Using the real spherical harmonics functions, the physical dipole components (ρ_{NS}, ρ_{FB} and ρ_{EW}) could give us more information about the arrival direction of the CRs. The AMS-02 experiment is able to detect, in the sub-TeV energy range,

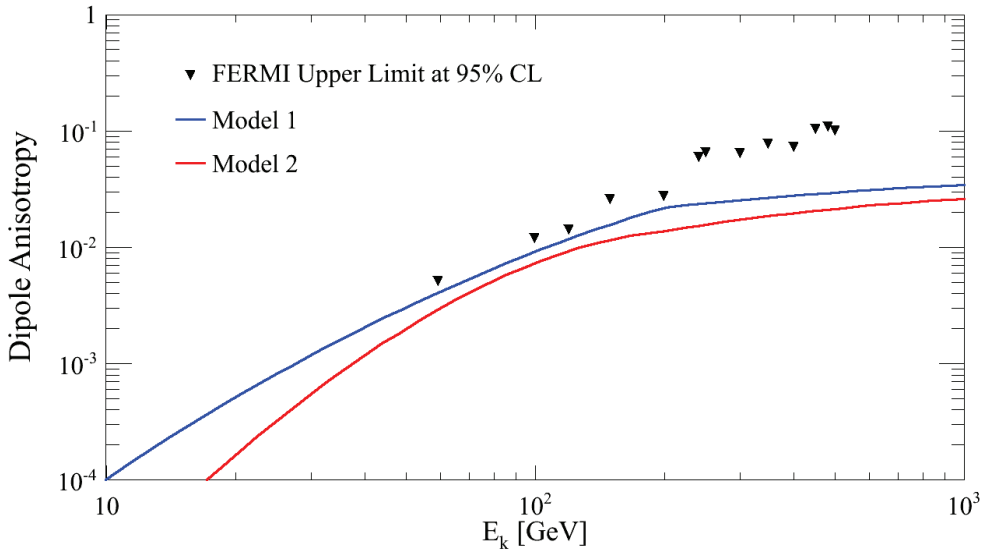

Figure 4.6: Dipole anisotropy for electron plus positron from Vela-X (Models 1 and 2, see section 4.2.2) compared with the FERMI-LAT upper limits on δ versus the minimum energy for 95% confidence level.

both direction and intensity of the dipolar CR anisotropy, if it exists. It can measure an unprecedented amount of particles arriving from a wide fraction of the sky. A preliminary analysis, using the initial 21 months of operation of AMS-02, was made on positrons detected in the energy range from 16 GeV to 350 GeV (Casaus, J. & the AMS-02 Collaboration 2013) and the first results on the anisotropy of the positron to proton ratio are reported. Protons, supposed to be more isotropic than other CR species, were taken as the reference for the measurement of the positron anisotropy. The analysis were done on the CR arrival directions inside AMS-02 and using the asymptotic directions obtained after the back-tracing in the magnetosphere. The trajectory were reconstructed using the internal IGRF-11 and external TS05 magnetic field models up to the magnetosphere border (see chapter 2 for a better explanation of the geomagnetic field representation). Since our predicted signal of anisotropy from PWN comes mainly from Vela-X, galactic longitude 263.6° and latitude −2.8°, we can focus our attention on the ρ_{EW} dipole component. In figure 4.7, the ρ_{EW} dipole component, evaluated from the AMS-02 positron data reconstructed at the magnetopause, is reported as a function of the minimum energy of the chosen bins. The three different exclusion regions (outside 1, 2 and 3σ) are represented in color scale. The data points are compatible with an isotropic signal, because the accepted region includes zero. Using this dipole component, equation (4.58), that reproduces the degree of anisotropy pointing in the direction of the single source, can be easily compared with the data (see solid line in figure 4.7). Since we are focusing the

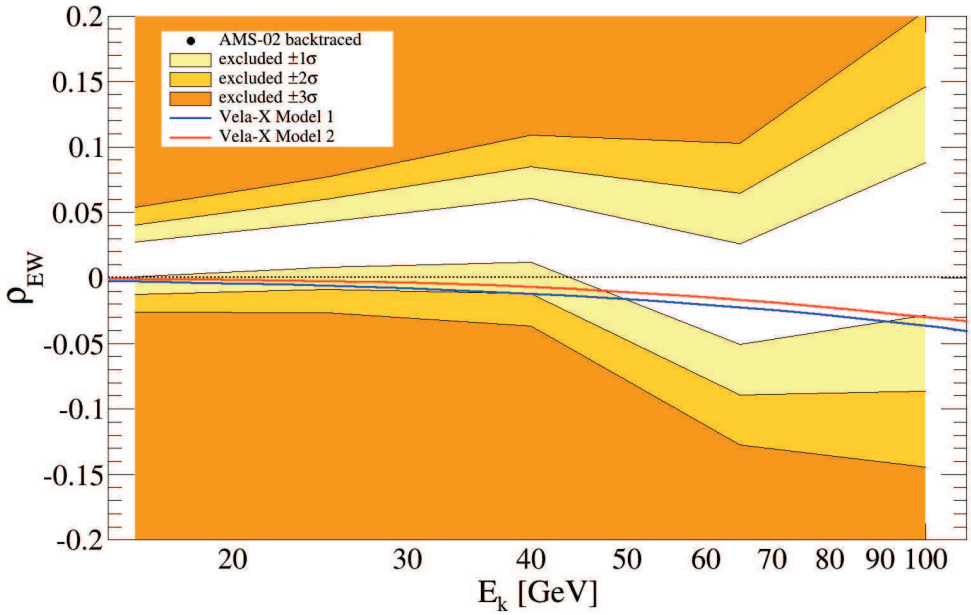

Figure 4.7: Exclusion plot at 68% (1σ), 95% (2σ) and 99% (3σ) CL, outside magnetosphere, of the ρ_{EW} dipole component compared with the positron signal from Vela-X (Models 1 and 2, see section 4.2.2).

attention on a single source, the denominator of equation (4.58) keeps into account not only the positron cLIS, but the difference between AMS-02 positron data and the Vela-X contribution. The ρ_{EW} dipole component is pointing from the galactic West (galactic longitude 270°) to the galactic East (galactic longitude 90°). To have the right contribution of Vela-X to the East-West direction, equation (4.58) must be multiplied by a factor: $\sin(90° + 2.8°) \times \sin(263.6°)$. The Vela-X contributions (Model 1 and 2) to the East-West dipole component are in agreement with the AMS-02 data inside 2σ. This analysis is just the first attempt, because, as we reported in section 4.2, Vela-X contributes to the electron and positron excess for energies above 100 GeV (while this data analysis is performed for energies up to 350 GeV); moreover, below 100 GeV we have already mentioned that contributions from mature pulsars (10^5 years old) are expected. With a better set of PWN photon data, it is possible to include in the analysis more sources to explain the full electron and positron excess flux and, also, to diminish an anisotropic signal coming from these different sources. Finally, up to now, it is not yet possible to discriminate an anisotropic signal in the CR sky, but the precise AMS-02 data and the separation of the dipole signal into the three different components could leads to observe the anisotropy, if it exists, of these astrophysical sources (pulsars as Vela-X can contribute to the EW component).

A preliminary test using a Monte Carlo approach, instead of the analytic diffu-

sion equation, has been done. The basic idea is to follow the particles injected by a source up to the Earth position, observing the arrival direction after the diffusion. The results available are in agreement with the analytic ones. The power of this model resides in the possibilities to change, for example, the diffusion parameters (e.g., the diffusion coefficient), introducing anisotropic diffusion in the galactic plane and in the halo.

Conclusions

Our information on cosmic ray electron and positron sources largely stems from the analysis of the high energy part of their spectra.

In the present work, we have analysed the AMS-02 electron, positron and electron-plus-positron spectra in the energy range above about 10 GeV. The excess spectra for electrons and positrons were obtained by subtracting the expected "classical" local interstellar spectra, computed with GALPROP, from the omnidirectional distributions observed by AMS-02. A comparison above $\sim$ 50 GeV indicates, for electrons and positrons, the same flux and the same slope with a spectral index of ~ -2.5. These excess spectra can be accounted by pulsar sources in which electron-positron pairs will be accelerated by the surrounding pulsar wind nebula. We then have evaluated electron and positron spectra generated in the Vela-X pulsar wind nebula and propagated them to the Earth. We have used two different models built using observed parameters of Vela and Crab nebulae and we have compared results with observations. Both models, taking into account uncertainties and assumptions, are not in disagreement with the AMS-02 excess components at energies higher than about 100 GeV. Vela-X Model 2, built on Crab, requires a particle conversion efficiency which is an order of magnitude higher than Model 1. The Vela-X contribute can be enhanced by another source with Vela-like distance (few hundreds of pc) and age (some tens of kyr). At energy lower than 100 GeV, a contribution of aged pulsars (10^5 years old) is expected. There are several of them close to the Earth, like Geminga or Monogem, which may contribute, because the electrons and positrons released are still coming to the Solar System, but the emission of their PWN is no more observable. If no other sources are missed, we expect a clear dipole anisotropy above 100 GeV centred in the direction of Vela. At 200 GeV, the dipole anisotropy for electrons plus positrons from Vela-X is expected of the order of $\sim$ 2% not yet excluded, or confirmed, by the FERMI experiment. Conversely, at lower energy, several sources can contribute to the electron and positron spectra, but the angular

distribution of all these sources should be more isotropic.

Our result is in agreement with models describing the origin of the pulsar wind nebula and, at the same time, it can be used to constrain the fraction of the spin-down luminosity, which is transferred to particle acceleration needed to fit the excess spectra observed by AMS-02. The satisfactory agreement between models and data leads to keep into account pulsar wind nebulae as sources of electrons and positrons. Therefore, a realistic LIS should include this type of electron and positron sources.

A single source, as Vela-X located in the galactic West, leaves a dipole signal in the electron and positron arrival directions. The AMS-02 experiment is located inside the magnetosphere; thus, an anisotropic signal in cosmic rays can be observed reconstructing the particle trajectories up to the magnetopause, using both an internal (IGRF) plus external (TS05) magnetic fields. With this technique, called back-tracing, we can separate particles produced outside the magnetosphere from the ones generated or trapped inside. Using the spherical harmonics approach in galactic coordinates, we compared the East-West component of the AMS-02 data with our models. Concerning the ρ_{EW} dipole component, the anisotropy from Vela-X is inside 2σ from the AMS-02 data; thus, it is not yet possible to discriminate this source. Higher statistics and wider energy range are needed.

In the near future, the precise AMS-02 measurements will be very important. The fluxes from different kind of particles, detected in the same data taking period, could constraint the parameters of the CR propagation and could be used to understand more heliospheric or magnetospheric effects. The higher statistics can help to increase the sensitivity to the CR anisotropy, if it exists, in the sub-TeV energy range, giving more information related to the sky regions where these particles are produced.

Appendix A

Integrals used in the inverse Compton effect

The integrals used in section 3.6 are:

$$\int_0^{+\infty} \frac{x^{\nu-1}}{e^{\mu x}-1} dx = \frac{1}{\mu^{\nu}} \Gamma(\nu)\zeta(\nu) \qquad \Re e\mu > 0 \quad \Re e\nu > 1$$

where $\Gamma(\nu)$ is the Euler Gamma function, while $\zeta(\nu)$ is the Riemann Zeta function. If $(\nu - 1 = \alpha)$ is an integer, the Gamma function becomes the factorial function $\Gamma(\alpha + 1) = \alpha!$ and we obtain:

$$\int_0^{+\infty} \frac{x^{\alpha}}{e^{x}-1} dx = \alpha!\zeta(\alpha + 1)$$

The following table reports some values:

α	0	1	2	3	4	5
ν	1	2	3	4	5	6
$\Gamma(\alpha+1)$	1	1	2	6	24	120
$\zeta(\alpha+1)$	/	$\frac{\pi^2}{6}$	$\zeta(3)$	$\frac{\pi^4}{90}$	$\zeta(5)$	$\frac{\pi^6}{945}$

Appendix B

Detector

FERMI

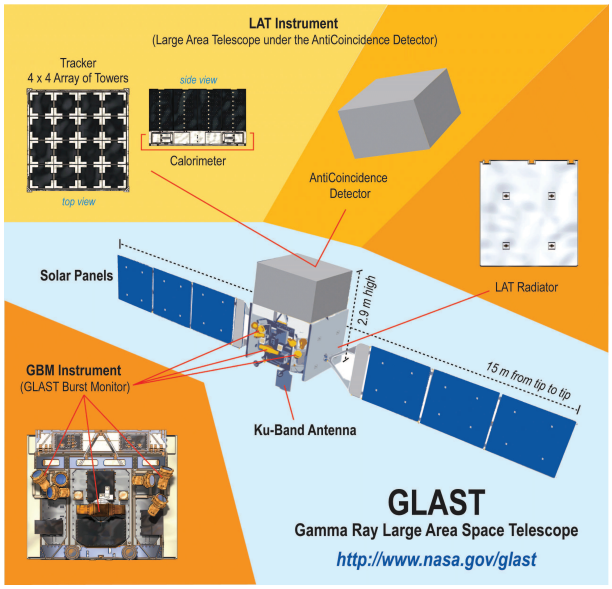

The Fermi Gamma-ray Space telescope was launched on June 11, 2008 on a Delta II heavy launch vehicle (Atwood et al. 2009). The primary since instrument on board Fermi is the LAT, a pair-conversion telescope which detects gamma-rays in the energy range from 20 MeV to $>$ 300 GeV. In addition, Fermi contains the Gammaray Burst Monitor (GBM), which is used to observe gamma-ray bursts (GRBs) in the energy range from 8 keV to 40 MeV. The LAT detector is composed of three major subsystems: the tracker, the calorimeter, and the Anti-Coincidence Detector (ACD). Fundamentally, the detector operates by inducing an incident gamma-ray to pair convert in the tracker into an electron and positron pair. The electron and position travel through the tracker and into the cesium iodide (CsI) calorimeter. The tracks and energy deposit can be used to infer the direction and energy of the incident gamma-ray. The LAT has an unprecedented effective area ($\sim$ 9500 cm^2), single-photon energy resolution ($\sim$ 10%), and single-photon angular resolution ($\sim 3.5^\circ$ at $E = 100$ MeV and decreasing to less than $\sim 0.15^\circ$ for $E > 10$ GeV) (Atwood et al. 2009). With its 2.4 sr field of view, Fermi can observe the entire sky almost uniformly every about 3 hours.

Bibliography

Abdo, A. A., Ajello, M., Allafort, A., et al. 2013, The Astrophysical Journal Supplement Series, 208, 17

Accardo, L., ..., Rozza, D., et al. 2014, Phys. Rev. Lett., 113, 121101

Ackermann, M., Ajello, M., Allafort, A., et al. 2012a, Astroparticle Physics, 35, 346

Ackermann, M., Ajello, M., Allafort, A., et al. 2012b, Physical Review Letters, 108, 011103

Ackermann, M., Ajello, M., Atwood, W. B., et al. 2010, Physical Review D, 82, 092003

Adriani, O., Barbarino, G. C., Bazilevskaya, G. A., et al. 2013, Phys. Rev. Lett., 111, 081102

Adriani, O., Barbarino, G. C., Bazilevskaya, G. A., et al. 2010, Astroparticle Physics, 34, 1

Adriani, O., Barbarino, G. C., Bazilevskaya, G. A., et al. 2009, Nature, 458, 607

Adriani, O., Barbarino, G. C., Bazilevskaya, G. A., et al. 2011, Physical Review Letters, 106, 201101

Aguilar, M., ..., Rozza, D., et al. 2013, Phys. Rev. Lett., 110, 141102

Aguilar, M., ..., Rozza, D., et al. 2014a, Phys. Rev. Lett., 113, 121102

Aguilar, M., ..., Rozza, D., et al. 2014b, Phys. Rev. Lett., 113, 221102

Aguilar, M., ..., Rozza, D., et al. 2015, Phys. Rev. Lett., 114, 171103

Aharonian, F., Akhperjanian, A. G., Bazer-Bachi, A. R., et al. 2006a, Astronomy & Astrophysics, 457, 899

Aharonian, F., Akhperjanian, A. G., Bazer-Bachi, A. R., et al. 2006b, Astronomy & Astrophysics, 448, L43

Aharonian, F. A., Atoyan, A. M., & Kifune, T. 1997, Monthly Notices of the RAS, 291, 162

Alcaraz, J., Alpat, B., Ambrosi, G., et al. 2000, Physics Letters B, 484, 10

Aleksi, J., Alvarez, E., Antonelli, L., et al. 2012, Astroparticle Physics, 35, 435

Aliu, E., Archambault, S., Arlen, T., et al. 2013, The Astrophysical Journal, 764, 38

Alvarez, L. & Compton, A. H. 1933, Phys. Rev., 43, 835

AMS-01 Collaboration, Aguilar, M., Alcaraz, J., et al. 2007, Physics Letters B, 646, 145

Anderson, C. D. 1932, Science, 76, 238

Atoyan, A. M. & Aharonian, F. A. 1996, Monthly Notices of the RAS, 278, 525

Atoyan, A. M., Aharonian, F. A., & Völk, H. J. 1995, Physical Review D, 52, 3265

Atwood, W. B., Abdo, A. A., Ackermann, M., et al. 2009, Astrophysical Journal, 697, 1071

Barwick, S. W., Beatty, J. J., Bower, C. R., et al. 1998, Astrophysical Journal, 498, 779

Beatty, J. J., Bhattacharyya, A., Bower, C., et al. 2004, Physical Review Letters, 93, 241102

Bednarek, W. & Bartosik, M. 2003, Astronomy and Astrophysics, 405, 689

Bednarek, W. & Protheroe, R. J. 1997, Physical Review Letters, 79, 2616

Berger, M. J. & Seltzer, S. M. 1964, in Studies in Penetration of Charged Particles in Matter, 205

Beringer, J., Arguin, J.-F., Barnett, R. M., et al. 2012, Physical Review D, 86, 010001

Bethe, H. & Heitler, W. 1934, Royal Society of London Proceedings Series A, 146, 83

Blackett, P. M. S. & Occhialini, G. 1932, Nature, 130, 363

Blasi, P. & Amato, E. 2011, in High-Energy Emission from Pulsars and their Systems, ed. D. F. Torres & N. Rea, 624

Blumenthal, G. R. & Gould, R. J. 1970, Reviews of Modern Physics, 42, 237

Bobik, P., ..., Rozza, D., et al. 2012, Advances in Space Research, 49, 1587 , advances in theory and observation of solar system dynamics - I

Bobik, P., ..., Rozza, D., et al. 2013a, in Proceedings of the 33^{rd} International Cosmic Ray Conference (ICRC2013), July 2-9 2013 (Rio de Janeiro, Brazil), arXiv: 1307.5199

Bobik, P., ..., Rozza, D., et al. 2013b, Proceedings of the 14^{th} ICATPP Conference, Villa Olmo 23-27 September 2013

Bobik, P., ..., Rozza, D., et al. 2013c, Proceedings of the 14^{th} ICATPP Conference, Villa Olmo 23-27 September 2013

Bobik, P., ..., Rozza, D., et al. 2013d, in Proceedings of the 33^{rd} International Cosmic Ray Conference (ICRC2013), July 2-9 2013 (Rio de Janeiro, Brazil), arXiv: 1307.5196

Bobik, P., ..., Rozza, D., et al. 2013, Advances in Astronomy, 2013

Bobik, P., ..., Rozza, D., et al. 2013a, Proceedings of the 14^{th} ICATPP Conference, Villa Olmo 23-27 September 2013

Bobik, P., ..., Rozza, D., et al. 2013b, in Proceedings of the 33^{rd} International Cosmic Ray Conference (ICRC2013), July 2-9 2013 (Rio de Janeiro, Brazil), arXiv: 1307.5195

Bobik, P., ..., Rozza, D., et al. 2013c, Proceedings of the 14^{th} ICATPP Conference, Villa Olmo 23-27 September 2013

Bobik, P., ..., Rozza, D., et al. 37 July, 2012, in Talk at 23^{rd} European Cosmic Ray Symposium (ECRS-2012), Moscow, Russia

Bobik, P., Boella, G., Boschini, M. J., et al. 2006a, Journal of Geophysical Research (Space Physics), 111, 5205

Bobik, P., Boella, G., Boschini, M. J., et al. 2006b, Journal of Geophysical Research (Space Physics), 111, 5205

Bobik, P., Boschini, M., Grandi, D., et al. 2005, in Washington DC American Geophysical Union Geophysical Monograph Series, Vol. 155, The Inner Magnetosphere: Physics and Modeling, ed. T. I. Pulkkinen, N. A. Tsyganenko, & R. H. W. Friedel, 301

Boezio, M., Barbiellini, G., Bonvicini, V., et al. 2001, Advances in Space Research, 27, 669

Boezio, M., Carlson, P., Francke, T., et al. 2000, Astrophysical Journal, 532, 653

Boschini, M., ..., Rozza, D., et al. 2013, in Proceedings of the 33^{rd} International Cosmic Ray Conference (ICRC2013), July 2-9 2013 (Rio de Janeiro, Brazil), arXiv: 1307.5192

Casaus, J. & the AMS-02 Collaboration. 2013, in Talk at the 33rd ICRC Conference, CR-EX - Experimental results, 1261

Cheng, K. S., Cheung, T., Lau, M. M., Yu, K. N., & Kwok, P. W. 1990, Journal of Physics G Nuclear Physics, 16, 1115

Cheng, K. S., Ho, C., & Ruderman, M. 1986, Astrophysical Journal, 300, 500

Clem, J. & Evenson, P. 2004, Journal of Geophysical Research (Space Physics), 109, 7107

Clem, J. & Evenson, P. 2009, Journal of Geophysical Research (Space Physics), 114, 10108

Clem, J. M., Clements, D. P., Esposito, J., et al. 1996, Astrophysical Journal, 464, 507

Clem, J. M., Evenson, P., Huber, D., et al. 2000, Journal of Geophysics Research, 105, 23099

Clem, J. M. & Evenson, P. A. 2002, Astrophysical Journal, 568, 216

Clifton, T. R. & Lyne, A. G. 1986, Nature, 320, 43

Cordes, J. M. & Lazio, T. J. W. 2002, ArXiv Astrophysics e-prints

Daugherty, J. K. & Harding, A. K. 1996, Astrophysical Journal, 458, 278

De Angelis, A. 2012, ArXiv:1208.6527

de Jager, O. C. & Harding, A. K. 1992, The Astrophysical Journal, 396, 161

de Jager, O. C., Harding, A. K., Sreekumar, P., & Strickman, M. 1996, Astronomy and Astrophysics, Supplement, 120, C441

Delahaye, T., Lineros, R., Donato, F., et al. 2009, A&A, 501, 821

Delahaye, T., Lavalle, J., Lineros, R., Donato, F., & Fornengo, N. 2010, A&A, 524, A51

Della Torre, S., Gervasi, M., Rancoita, P., Rozza, D., & Treves, A. 2013a, in Proceedings of the 33^{rd} International Cosmic Ray Conference (ICRC2013), July 2-9 2013 (Rio de Janeiro, Brazil), arXiv: 1307.5197

Della Torre, S., Gervasi, M., Rancoita, P., Rozza, D., & Treves, A. 2013b, Proceedings of the 14^{th} ICATPP Conference (Villa Olmo, Como), 23-27 September 2013, ArXiv e-prints: 1312.3483

Della Torre, S., Grandi, D., La Vacca, G., Rozza, D., & Tacconi, M. 2013c, Internal report for the AMS-02 Collaboration

Du Plessis, I., de Jager, O. C., Buchner, S., et al. 1995, The Astrophysical Journal, 453, 746

DuVernois, M. A., Barwick, S. W., Beatty, J. J., et al. 2001, Astrophysical Journal, 559, 296

Erber, T. 1966, Reviews of Modern Physics, 38, 626

Feng, L., Yang, R.-Z., He, H.-N., et al. 2014, Physics Letters B, 728, 250

Fermi, E. 1949, Phys. Rev., 75, 1169

Ginzburg, V. L. & Ptuskin, V. S. 1976, Rev. Mod. Phys., 48, 161

Ginzburg, V. L. & Syrovatskii, S. I. 1964, The Origin of Cosmic Rays (New York: Macmillan)

Golden, R. L., Stochaj, S. J., Stephens, S. A., et al. 1996, Astrophysical Journal, Letters, 457, L103

Goldreich, P. & Julian, W. H. 1969, Astrophysical Journal, 157, 869

Gould, R. J. 1975, Astrophysical Journal, 196, 689

Grandi, D. & Rozza, D. April 2014, Presentation for the AMS-02 Analysis Meeting

Grandi, D. & Rozza, D. March 2014, Presentation for the AMS-02 Analysis Meeting

Grandi, D. & Rozza, D. March 2015, Presentation for the AMS-02 Analysis Meeting

Grandi, D. & Rozza, D. November 2013, Presentation for the AMS-02 Analysis Meeting

Grandi, D. & Rozza, D. September 2014, Presentation for the AMS-02 Analysis Meeting

Grandi, D., Rozza, D., & Della Torre, S. October 2014, Presentation for the AMS-02 Analysis Meeting

Grimani, C., Stephens, S. A., Cafagna, F. S., et al. 2002, Astronomy and Astrophysics, 392, 287

Haino, S. & the AMS-02 Collaboration. 2013, in Talk at the 33rd ICRC Conference, CR-EX - Experimental results, 1265

Harding, A. K., Stern, J. V., Dyks, J., & Frackowiak, M. 2008, Astrophysical Journal, 680, 1378

Hartman, R. C., Bertsch, D. L., Bloom, S. D., et al. 1999, Astrophysical Journal, Supplement, 123, 79

Haslam, C. G. T., Salter, C. J., Stoffel, H., & Wilson, W. E. 1982, Astronomy and Astrophysics, Supplement, 47, 1

Hess, V. 1912, Phys. Zeits, 13, 10841091

Hillas, A. M., Akerlof, C. W., Biller, S. D., et al. 1998, The Astrophysical Journal, 503, 744

Horns, D., Aharonian, F., Santangelo, A., Hoffmann, A. I. D., & Masterson, C. 2006, Astronomy and Astrophysics, 451, L51

Huang, C.-L., Spence, H. E., Singer, H. J., & Tsyganenko, N. A. 2008, Journal of Geophysical Research (Space Physics), 113, 4208

Humensky, T. B. 2009, Fermi Symposium eConf Proceedings C091122, ArXiv e-prints: 0912.4304

Ibe, M., Matsumoto, S., Shirai, S., & Yanagida, T. T. 2013, JHEP, 1307, 063

Johnson, T. H. 1933, Phys. Rev., 43, 834

Johnson, T. H. 1935, Physical Review, 48, 287

Kamae, T., Karlsson, N., Mizuno, T., Abe, T., & Koi, T. 2006, Astrophysical Journal, 647, 692

Kaspi, V. M., Roberts, M. S. E., & Harding, A. K. 2006, Isolated neutron stars, ed. W. H. G. Lewin & M. van der Klis, 279–339

Kennel, C. F. & Coroniti, F. V. 1984a, The Astrophysical Journal, 283, 694

Kennel, C. F. & Coroniti, F. V. 1984b, The Astrophysical Journal, 283, 710

Kobayashi, T., Komori, Y., Yoshida, K., & Nishimura, J. 2004, Astrophysical Journal, 601, 340

Leroy, C. & Rancoita, P.-G. 2009, Principles of Radiation Interaction in Matter and Detection, 2nd Edition (World Scientific Publishing Co)

Lin, T., Finkbeiner, D. P., & Dobler, G. 2010, Physical Review D, 82, 023518

Linden, T. & Profumo, S. 2013, The Astrophysical Journal, 772, 18

Lorimer, D. R. 2008, Living Reviews in Relativity, 11

Lyne, A. G., Pritchard, R. S., Graham-Smith, F., & Camilo, F. 1996, Nature, 381, 497

Malyshev, D., Cholis, I., & Gelfand, J. 2009, Phys. Rev. D, 80, 063005

Manchester, R. N., Hobbs, G. B., Teoh, A., & Hobbs, M. 2005, VizieR Online Data Catalog, 7245, 0

Manchester, R. N. & Taylor, J. H. 1977, Pulsars

Mandl, F. & Shaw, G. 2010, Quantum Field Theory 2nd Edition (John Wiley and Sons)

Markwardt, C. B. & Ögelman, H. 1995, Nature, 375, 40

Markwardt, C. B. & Ögelman, H. B. 1997, Astrophysical Journal, Letters, 480, L13

Martín, J., Torres, D. F., & Rea, N. 2012, Monthly Notices of the RAS, 427, 415

Maurin, D., Donato, F., Taillet, R., & Salati, P. 2001, Astrophysical Journal, 555, 585

Maurin, D., Melot, F., & Taillet, R. 2013, ArXiv e-prints: 1302.5525

McCollough, J. P., Gannon, J. L., Baker, D. N., & Gehmeyr, M. 2008, Space Weather, 6, 10001

Moskalenko, I. V. & Strong, A. W. 1998, The Astrophysical Journal, 493, 694

Munakata, K., Kiuchi, T., Yasue, S., et al. 1997, Phys. Rev. D, 56, 23

Nagashima, K., Fujimoto, K., & Jacklyn, R. M. 1998, J. Geophys. Res., 103, 17429

Norbury, J. W. & Townsend, L. W. 2007, Nuclear Instruments and Methods in Physics Research B, 254, 187

P. Bobik, e. a. 2012, Astroph.J., 745, 132

Pacini, D. 1912, Nuovo Cim. VI/3 93 (translated and commented by A. De Angelis in ArXiv:1002.1810)

Pacini, F. & Salvati, M. 1973, Astrophysical Journal, 186, 249

Parker, E. N. 1957, Phis. R., 107

Parker, E. N. 1965, Planet. Space. Sci., 13, 9

Platania, P., Bensadoun, M., Bersanelli, M., et al. 1998, Astrophysical Journal, 505, 473

Ptuskin, V. S., Moskalenko, I. V., Jones, F. C., Strong, A. W., & Zirakashvili, V. N. 2006, The Astrophysical Journal, 642, 902

Rees, M. J. & Gunn, J. E. 1974, Monthly Notices of the RAS, 167, 1

Romani, R. W. 1996, Astrophysical Journal, 470, 469

Rossi, B. 1930, Physical Review, 36, 606

Rossi, B. 1934, Phys. Rev., 45, 212

Rossi, B. 1964, Cosmic rays, McGraw-Hill paperbacks in physics (McGraw-Hill)

Ruderman, M. A. & Sutherland, P. G. 1975, Astrophysical Journal, 196, 51

Sartore, N., Ripamonti, E., Treves, A., & Turolla, R. 2009

Schlickeiser, R. 2002, Cosmic Rays Astrophysics (Berlin: Springer)

Sefako, R. R. & de Jager, O. C. 2003, The Astrophysical Journal, 593, 1013

Seltzer, S. M. & Berger, M. J. 1984, The International Journal of Applied Radiation and Isotopes, 35, 665

Shue, J.-H., Chao, J. K., Fu, H. C., et al. 1997, Journal of Geophysical Research, 102, 9497

Sibeck, D. G., Lopez, R. E., & Roelof, E. C. 1991, Journal of Geophysics Research, 96, 5489

Störmer, C. 1956, The polar aurora (Oxford University Press)

Strauss, R. & Potgieter, M. 2014, Advances in Space Research, 53, 1015

Strong, A. W., Moskalenko, I. V., & Ptuskin, V. S. 2007, Annual Review of Nuclear and Particle Science, 57, 285

Sturrock, P. A. 1971, Astrophysical Journal, 164, 529

Taani, A., Naso, L., Wei, Y., Zhang, C., & Zhao, Y. 2012, Astrophys.Space Sci., 341, 601

Tanaka, S. J. & Takahara, F. 2010, The Astrophysical Journal, 715, 1248

Tsyganenko, N. A. 1995, Journal of Geophysics Research, 100, 5599

Tsyganenko, N. A. 1996, in ESA Special Publication, Vol. 389, International Conference on Substorms, ed. E. J. Rolfe & B. Kaldeich, 181

Tsyganenko, N. A. & Sitnov, M. I. 2005, Journal of Geophysical Research (Space Physics), 110, 3208

Venter, C. & de Jager, O. C. 2007, in WE-Heraeus Seminar on Neutron Stars and Pulsars 40 years after the Discovery, ed. W. Becker & H. H. Huang, 40

Vladimirov, A., Digel, S., Jhannesson, G., et al. 2011, Computer Physics Communications, 182, 1156

Welsh, B. Y. & Shelton, R. L. 2009, Astrophysics and Space Science, 323, 1

Yuan, J. P., Wang, N., Manchester, R. N., & Liu, Z. Y. 2010, Monthly Notices of the RAS, 404, 289

Yuan, Q., Bi, X.-J., Chen, G.-M., et al. 2013, ArXiv e-prints: 1304.1482

Yue, Y. L., Xu, R. X., & Zhu, W. W. 2007, Advances in Space Research, 40, 1491

Zhang, L., Chen, S. B., & Fang, J. 2008, The Astrophysical Journal, 676, 1210

Zhang, Q.-H., Dunlop, M. W., Holme, R., & Woodfield, E. E. 2010, Annales Geophysicae, 28, 309

Zhang L., . C. K. S. 2001, Astronomy and Astrophysics, 368, 1063

Zuccon, P. et al. 2013, in Poster at the 33rd ICRC Conference, CR-IN - Methods, techniques and instrumentation, 1064